UNIVERSITÀ
DI PARMA

Università degli Studi di Parma

Dottorato di Ricerca in Scienza e Tecnologia dei Materiali

XXXVII Ciclo

Linear and nonlinear optical microscopy for advanced applications: the role of a spectroscopist in bioimaging

Coordinatore
Prof. Enrico Dalcanale

Relatrice
Prof.ssa Cristina Sissa

Dottoranda
Ilaria Ferraboschi

Anni accademici 2021/2022 - 2024/2025

Contents

List of Publications

1. M. Ghezzi, S. Pescina, A. Delledonne, I. Ferraboschi, C. Sissa, F. Terenziani, P. De Freitas Rosa Remiro, P. Santi, S. Nicoli, Improvement of imiquimod solubilization and skin retention via TPGS micelles: exploiting the co-solubilizing effect of oleic acid. Pharmaceutics, 2021, 13, 1476

2. M. Ghezzi, I. Ferraboschi, A. Delledonne, S. Pescina, C. Padula, P. Santi, C. Sissa, F. Terenziani, S. Nicoli, Cyclosporine-loaded micelles for ocular delivery: Investigating the penetration mechanisms. Journal of Controlled Release, 2022, 349, 744–755

3. S. D'Auria, A. Pedrini, I. Ferraboschi, J. Vachon, C. Sissa, R. Pinalli, E. Dalcanale, Two-photon microscopy as a visual tool for polymer compatibilization monitoring: the PE-EVOH case. Soft Matter, 2023, 19(10), 1900-1906

4. M. Ghezzi, I. Ferraboschi, A. Fantini, S. Pescina, C. Padula, P. Santi, C. Sissa, S. Nicoli, Hyaluronic acid–PVA films for the simultaneous delivery of dexamethasone and levofloxacin to ocular tissues. International Journal of Pharmaceutics, 2023, 638, 122911

5. I. Ferraboschi, J. Ovčar, K. V. Vygranenko, S. Yu, A. Min-

ervino, A. Wrzosek, A. Szewczyk, R. Rozza, A. Magistrato, K.D. Belfield, D. T. Gryko, L. Grisanti, C. Sissa, Neutral rhodol-based dyes expressing localization in mitochondria. Organic & Biomolecular Chemistry, 2024

6. M. Alcaina-Hernando, I. Malvacio, I. Ferraboschi, C. Huck-Iriart, A. Bianchera, S. Sala, J. S. Pedersen, L. Ferrer-Tasies, S. Pescina, C. Sissa, N. Ventosa, A. Córdoba, A new plant-based drug delivery platform based on alkyl polyglucosides and β-sitosterol nanovesicles for topical delivery. Applied Materials Today, 2024, 41, 102467

7. M. Brugnera, M. Vicario-de-la-Torre, M. A. González-Cela-Casamayor, F. M. González-Fernández, I. Ferraboschi, V. Andrés-Guerrero, S. Nicoli, C. Sissa, S. Pescina, R. Herrero-Vanrell, I. Bravo-Osuna, Disclosing Long-term Tolerance, Efficacy and Penetration Properties of Hyaluronic Acid-coated Latanoprost-loaded Liposomes as Chronic Glaucoma Therapy. Submitted to Journal of Controlled Release, in peer review

8. I. Ferraboschi, F. Canzolino, E. Ferrari, C. Sissa, M. Masino, M. Rizzi, S. Bussolati, G. Basini, S. Bertini, S. Grolli, R. Ramoni, F. Di Ianni, A. Vetere, E. Bigliardi, Detection of microplastics in the feline placenta and fetus. Submitted to Plos One, in peer review

9. L. V. Sanchez-Castillo, F. Guareschi, E. Tsekoura, V. Patterlini, A. Delledonne, I. Ferraboschi, C. Sissa, F. Sonvico, R. Naraina, Formulation of siRNA Nanoparticles, Transfection and Enhanced Adhesion -Penetration in Nasal Mucosal Tissue. Submitted to Journal of Controlled Release, in peer review

Introduction

Since its invention in 17th century, microscopy has dramatically changed biology by allowing the visualization of biological targets in their physiological environments. [1] Nowadays, several optical microscopy techniques suitable for biological investigations are available, differing in the types of radiation employed or the contrast mechanisms used to visualize samples. For instance, microscopes can utilize electromagnetic radiation (*e.g.* UV-Vis, infrared), acoustic radiation, or matter waves (such as electrons or protons). They can also exploit various contrast mechanisms, such as phase contrast, polarization, or fluorescence to generate images.

Nevertheless, among the various microscopy techniques, fluorescence microscopy drawn major attention since 1871, *i.e.* when the first fluorescent stainer was developed. [2]

This work mainly describes the application to various biological investigations of two fluorescence microscopy techniques: confocal fluorescence microscopy (CFM) and two-photon microscopy (2PM). Moreover, a work employing micro-Raman spectroscopy (mRS) is also presented.

These techniques differ mainly in the phenomena involved in the generation of the detected signal. Indeed, CFM exploits linear interactions between radiation and matter, while 2PM and mRS

exploit nonlinear ones.

The term "linear interaction" refers to a phenomenon in which a single photon of the incident radiation interacts with one molecule of the sample at a time. Conversely, the term "nonlinear interaction" describes a phenomenon in which multiple photons interact simultaneously with the same molecule of the sample. As a consequence, linear interaction refers to phenomena in which the response of the system is directly proportional to the intensity of the incident light, while nonlinear interaction refers to phenomena where the response of the system depends nonlinearly on the intensity of the incident light.

In CFM, the only signals detected are fluorescence or phosphorescence, both of which are generated by one-photon absorption. Usually, it exploits a focused laser beam falling in the UV-vis spectral region that illuminates a small region of the sample. The focus of the laser is then moved in the x and y directions to scan the whole sample. The out-coming emission collected in each illuminated region generates the final image. [3]. Moreover, the term "confocal" indicates the presence of a pinhole that selects the plane from which the fluorescence signal arise, giving to the technique a 3D resolution. Unfortunately, the 3D resolution achieved is limited. Indeed, the closer the pinhole, the better the resolution but the lower the intensity of the signal collected. Thus, CFM is better applied to thin samples than to deep imaging. [4]

On the other hand, 2PM exploits nonlinear phenomena. Notably, two nonlinear phenomena are exploited in the studies presented in this thesis: two-photon excited fluorescence (TPFE) and second harmonic generation (SHG) (see Sec. A.1 for further details). Considering the same type of fluorescent probe used in the CFM, the photons involved in TPFE and SHG have half the energy of the photon involved in linear phenomena. Thus, 2PM usually exploits focused laser beam falling in the near infrared (NIR) spectral region. NIR radiation is less absorbed and less scattered by biological sam-

ples compared to UV-vis light, giving to 2PM several advantages compared to CFM:

- Better penetration in biological tissues
- Lower photobleaching
- Lower scattering

Moreover, the exploitation of nonlinear phenomena gives to 2PM an intrinsic 3D resolution. Indeed, a high photon density is needed for the simultaneous interaction of two or more photons with one molecule. Only in a small volume around the laser focal point, *i.e.* the *voxel*, the proper photon density is reached and by moving the voxel in the three dimensions, 3D images can be acquired. Thus, 2PM is a widespread technique for imaging thick biological samples. [5]

Unlike CFM and 2PM, mRS does not detect a fluorescence signal. Indeed, this technique relies on the light scattering produced by the sample. The term "Raman scattering" indicates an inelastic scattering of light that entails an energy exchange between the incident radiation and the molecule. The amount energy exchanged between the sample and the radiation matches the vibrational energy of the molecule itself. Thus, by recording the scattered light and knowing the incident radiation, information regarding the molecule vibrations are gained. This technique allows to obtain a spectrum that is unique for the molecule that produced the scattering, leading to its identification. [6, 7, 8]

In this doctoral work, I focused on utilizing the microscopy techniques introduced earlier, particularly 2PM, to study complex biological systems. The 2PM microscope was acquired by the Chemistry, Life Sciences and Environmental Sustainability Department of the University of Parma just before the start of my doctoral research, and part of my work was therefore dedicated to studying

the operation and potential of the instrument, including the measurement of correction curves for the acquisition of excitation and emission spectra. Additionally, leveraging the expertise of the research group that hosted me, I integrated the information derived from the images with spectroscopy data by collecting emission and excitation spectra and/or performing hyperspectral image analysis, which allows for capturing spectral information for each pixel in an image. In this case, each pixel not only represents a single color value but a series of spectral values at different wavelengths. This type of analysis therefore provides a vast amount of information about the materials under investigation, as well as the physical and chemical properties of the observed samples.

This thesis is organized in 4 chapters, one dedicated to the exploitation of each technique in biological investigations and one describing two different collaborations with non-academic institutions. Chapter 1 describes the characterization of two novel dyes for mitochondria tracking using CFM. Chapter 2 presents four studies in which 2PM was exploited for the characterization of topical formulations. Notably, Sec. 2.2 focuses on the information that can be gained thanks to the advantage of acquiring 3D and hyperspectral images through 2PM. While, Sec. 2.3 focuses on how 2PM deep penetration in biological tissues can be exploited for the study of formulation permeation. Chapter 3 describes the exploitation of micro-Raman spectroscopy to detect and identify microplastics present in feline placentas and fetuses. Chapter 4 describes two case studies stemming from the collaboration with non-academic institutions, where I learned how microfluidics can be applied to cells culture with the aim of exploiting this technology in future permeation studies and I explored the potentialities of 2PM for the investigation of a novel formulation for respiratoy diseases.

A technical section (see Appendix. A) describing the nonlinear phenomena exploited in 2PM and the physiological structure of non-treated eye and skin tissues is present at the end of this work

of thesis.

All the studies were carried out thanks to the collaboration with different research groups:

- Prof. Daniel T. Gryko and Kateryna V. Vygranenko from the the Institute of Organic Chemistry – Polish Academy of Sciences. They synthesized the fluorescent mitochondria trackers investigated in Chapter 1

- Prof. Luca Grisanti and Juraj Ovčar from Ruđer Bošković Institute that collaborated in the development of the model for neutral mitochondria trackers presented in Chapter 1

- Prof. Kevin D. Belfield and Shupei Yu from the New Jersey Institute of Technology that provided the necessary expertise for cell cultures and CFM presented in Chapter 1

- The group of Prof. Silvia Pescina and Prof. Sara Nicoli from the Food and Drug Department of the University of Parma, which provided the *ex vivo* animal tissues, contributed to the development of the experimental set-up for the 2PM analysis and provided the expertise and facilities necessary for the permeation experiments (Chapter 2). Moreover, they prepared the formulation designed for drug delivery discussed in Sec. 2.2.1

- the Nanomol-Bio group of Prof. Nora Ventosa (ICMAB-CSIC) and Marta Alacaina Hernando of Nanomol Technologies S.L., Spain, that synthesized and characterized the formulation investigated in Sec. 2.2.2

- The group of Prof. Fabio Sonvico from the Food and Drug Department of the University of Parma, that prepared the formulation and the biological tissues presented in Sec. 2.3.1

- Prof. Rocío Herrero-Vanrell, Prof. Irene Bravo-Osuna and Marco Brugnera from the Complutense University (UCM), Madrid, Spain that synthesized and characterize the formulation presented in Sec. 2.3.2
- The group of Prof. Giuseppina Basini, Prof. Alessandro Vetere and Prof. Enrico Bigliardi from the Department of Veterinary Science of the University of Parma, that prepared the samples presented in Chapter 3
- Elvesys, in particular Dr. Lisa Muiznieks from the Microfluidic Innovation Center (MIC) that supervised the activities described in Sec. 4.2.
- An international pharmaceutical company was involved in the project presented in Sec. 4.3.

The activities presented in Chapter 1 and in Sec. 4.3 were carried out at New Jersey Institute of Technology (New Jersey, USA) and at Elvesys (now the Microfluidic Innovation Center) (Paris, France) during two separate secondments undertaken as part of a Research and Innovation Staff Exchange (RISE) funded by the European Commission, the project Micro4Nano (Grant agreement No: 101007804).

Chapter 1

In vitro experiments: tracking mitochondria with a new family of neutral dyes

1.1 Introduction

The term "*in vitro*", literally meaning "in glass", usually refers to studies conducted in a Petri dish on microorganisms, cell lines or biological molecules outside of their biological environments. [9] The isolation of these samples from their native environment is one of the major limitations of *in vitro* assays. However, *in vitro* experiments allows scientists to have greater control over the experiments and facilitates the study of fundamental biological functions impossible to assess in the complexity of a whole tissue or organism. Thus, *in vitro* tests are a necessary step in the preclinical drug development, especially considering the high-throughput screening that can be achieved and the low cost associated with conducting these tests. [10] Several studies can be conducted through *in vitro* models such as the determination of drug toxicology and activity towards a

selected target as well as preliminary binding studies, prediction of pharmacokinetic parameters or drug resistance. [11] Indeed, cells cultured in a plate are easily marked, stained, visualized through optical microscopes or confocal ones, enabling the exploitation of several techniques to analyze them. [12]

In the study presented in this chapter, *in vitro* assays were exploited to test the cytotoxicity and the biological activity of two novel dyes designed for mitochondria tracking by our collaborator at the Institute of Organic Chemistry – Polish Academy of Sciences. [13] In particular, the cytotoxicity of the target molecules was evaluated on HeLa cells line through cell viability assay, the stained cells were imaged through confocal microscopy and colocalization assays were carried out to assess the capacity of the dyes to track mitochondria. The work was developed in the framework of the Research and Innovation Staff Exchange (RISE) project Micro4Nano, funded by the European Commission. The work has been carried out at the New Jersey Institute of Technology (USA), under the supervision of prof. Kevin D. Belfield, and in collaboration with the Institute of Organic Chemistry – Polish Academy of Sciences and the Ruđer Bošković Institute, all Partners of Micro4Nano.

1.2 Characterization of a novel dye for staining mitochondria

Mitochondria are organelles present in the cytoplasm of most eukaryotic cells. They generate ATP molecules, the "fuel" of metabolic energy, and they participate in other crucial activities such as: reactive oxygen species production, ionic homeostasis, biosynthesis of several substances and thermo-regulation. [14]

Thus, mitochondria dysfunctions severely impact the cells well-functioning and therefore the health of living beings. Indeed, several diseases have been associated with mitochondria dysfunctions, [15] highlighting the critical importance of monitoring and studying these organelles.

Mitochondria are motile organelles that control their morphology to carry out the vital processes they are involved into. The four main actions that regulate the mitochondria functioning (fission, fusion, degradation and transport) are commonly referred to as "mitochondrial dynamics". [16] Therefore, the study of mitochondrial dynamics can reveal crucial information for the development of disease treatment strategies.

The use of fluorescent probes, *i.e.* trackers, is a valuable method for following mitochondrial dynamics in their native environment, the cell. [17] The vast majority of commercially available mitochondria trackers are positively charged. [18, 19, 20] They exploit the electrochemical potential difference generated across the mitochondrial inner membrane due to the proton gradient established by the respiratory chain to enter into the organelle. [21] Unfortunately, cationic trackers exhibit several drawbacks, *e.g.* chemical instability and high cytotoxicity due to mitochondrial membrane depolarization. [22] A possible alternative route to track mitochondria is by exploiting neutral trackers that do not present the same limitations as cationic ones.

Namely, their accumulation in mitochondria does not lead to membrane depolarization, [23, 24] allowing for the investigation of mitochondrial morphology in a minimally perturbed environment. Despite the advantages, there have been far fewer reports of neutral tracking probes compared to charged ones. [19, 22, 23, 24, 25, 26, 27, 28, 29, 30, 31] In fact, the physical mechanisms of the localization of neutral molecules in mitochondria are not fully understood. The lack of understanding of the physical processes underpinning mitochondrial localization of neutral trackers from a fundamental point of view is detrimental to the formulation of improved strategies for rational design of novel trackers, as well as to the integrity of the interpretations of mitochondrial tracking experiments.

In this section, the photophysical and biological characterization of two potential neutral mitochondria trackers, as well as a theoretical model providing a plausible explanation of their interaction with the mitochondrial membrane, is presented.

FM and **MOFM** are two red-fluorescent sulphone rhodol-based dyes which structures differ only for the substitution of their upper ring moiety (Fig. 1.1).

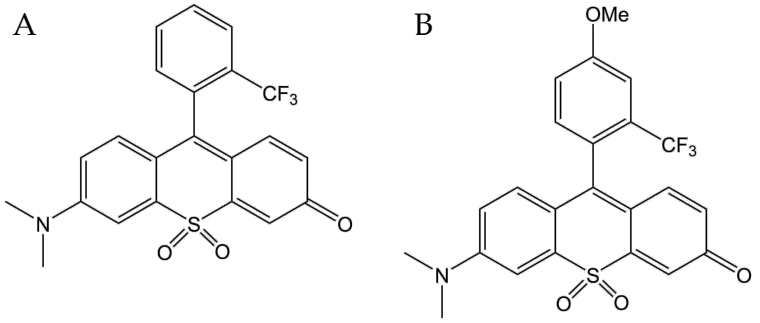

Figure 1.1: Chemical structures of (A) **FM** and (B) **MOFM**.

Their photophysical properties were studied in commonly used organic solvents as well as in biological relevant environments like PBS and cell culture medium. The results are reported in Tab. 1.1.

Table 1.1: Quantum yields (QY) and maxima of absorption (λ_{abs}^{max}) and emission (λ_{em}^{max}) spectra of **FM** and **MOFM** measured in various solvents

Compound	Solvent	QY	λ_{abs}^{max} (nm)	λ_{em}^{max} (nm)
FM	Toluene	0.05	548	642
	DCM	0.46	576	680
	DMSO	0.28	605	699
	PBS	0.04	669	717
	Cell medium	0.01	669	717
MOFM	Toluene	0.06	548	647
	DCM	0.45	574	680
	DMSO	0.30	601	698
	PBS	0.02	668	717
	Cell medium	0.01	669	717

Both molecules share a common backbone that determines their photophysical properties. Indeed, both **MOFM** and **FM** present quantum yields that vary from $\sim$0.45 in DCM to less than 0.05 in water, PBS and cell culture medium, and similar solubility. Moreover, their emission and absorption maxima shift towards higher wavelengths when going from non- to more polar solvents.

The shift of absorption and/or emission spectra in polar solvents is a phenomenon called "solvatochromism" and indicates that the ground and/or the excited state have non-negligible dipole moments that are stabilized by polar solvents. When the shift is toward the red edge of the UV-vis spectrum, the solvatochromism is referred to as "positive solvatochromism". Solvatochromism is usually associated with the presence of charge-transfer transitions, which involve a partial transfer of charge among different molecular moieties.

To further study the **MOFM** and **FM** excited states, anisotropy

studies were performed on both molecules in glycerol (Fig. 1.2). Anisotropy measures can unveil important information regarding the number and relative orientation of states involved in the absorption and emission processes (see Sec. 1.6.1 for technical description of the measurements performed). [32]

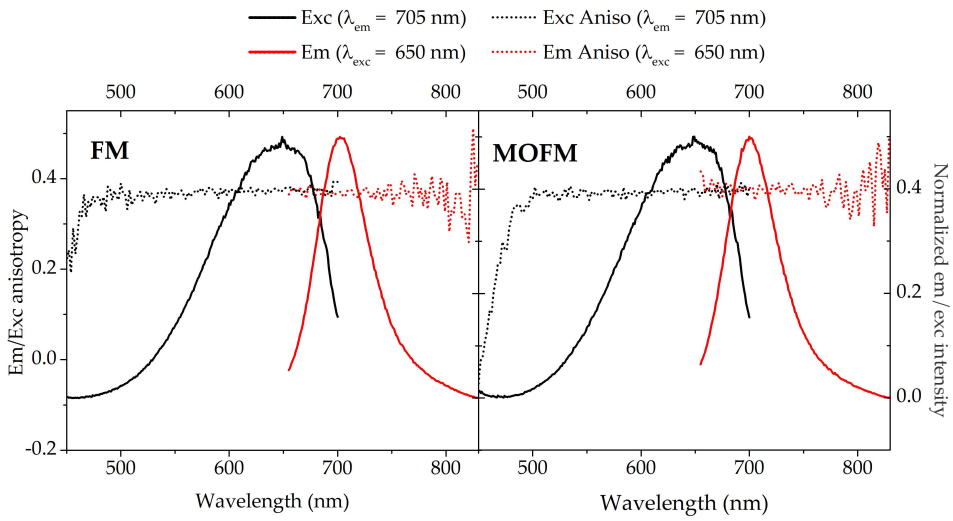

Figure 1.2: Emission and excitation spectra; emission and excitation anisotropy acquired in glycerol of **FM** and **MOFM**.

The spectra reported in Fig. 1.2 show that the emission and excitation anisotropy of both molecules are constant within the whole respective band. A constant value of excitation anisotropy indicates that only one excited state is involved in the absorption transition. Moreover, an equal value of the emission and excitation anisotropy reveals that the same excited state is involved in both transitions. Finally, the value of anisotropy close to 0.4, which is the limiting value for anisotropy, points out that the ground and excited states transition dipole moment are almost parallel. [32]

Additionally, to fully characterize the excited states of **FM** and **MOFM**, the two-photon absorption (2PA) cross sections were mea-

sured (see Sec. 1.6.1). The bandshapes of one-photon absorption and 2PA spectra overlaps, confirming that the same excited state is involved in the two processes, as expected for non centrosymmetric dyes. [33]

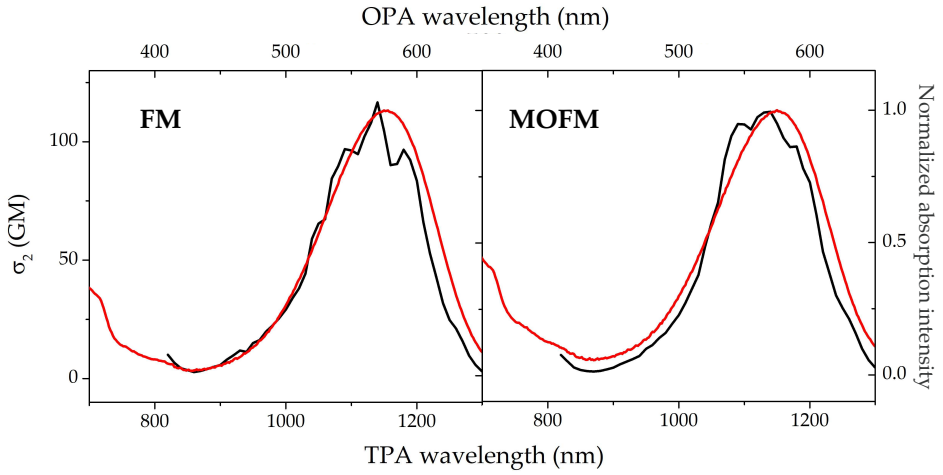

Figure 1.3: Two-photon absorption cross-section (black lines) and normalized one-photon absorption (red lines) of **FM** and **MOFM** in DCM.

Both molecules exhibit appreciable values of the 2PA cross section σ ($\sigma_{\mathbf{FM}}^{\lambda_{max}} = 120$ GM and $\sigma_{\mathbf{MOFM}}^{\lambda_{max}} = 110$ GM), enabling a potential exploitation also for two-photon microscopy experiments.

Once the photophysical properties of the target molecules were determined, we evaluated the biological features of **FM** and **MOFM** in term of cytotoxicity and ability to track mitochondria.

1.3 *In vitro* experiments: cell viability studies and mitochondria tracking

Cytotoxicity refers to the potential of a compound to induce cell death and is, therefore, the primary characteristic that must be evaluated for compounds interacting with biological samples. Cytotoxicity tests are pivotal to determine the amount of compound that can come in contact with cells without damaging them. [34] In cytotoxicity tests, cell viability is the parameter commonly determined. [35] Cell viability assays aim to define the number of healthy cells present in a sample. [36]

The cell viability of **FM** and **MOFM** was assessed after 24 hours of incubation in HeLa cells at different concentrations as reported in Fig. 1.4 (see Sec. 1.6.2 for technical description of the procedure).

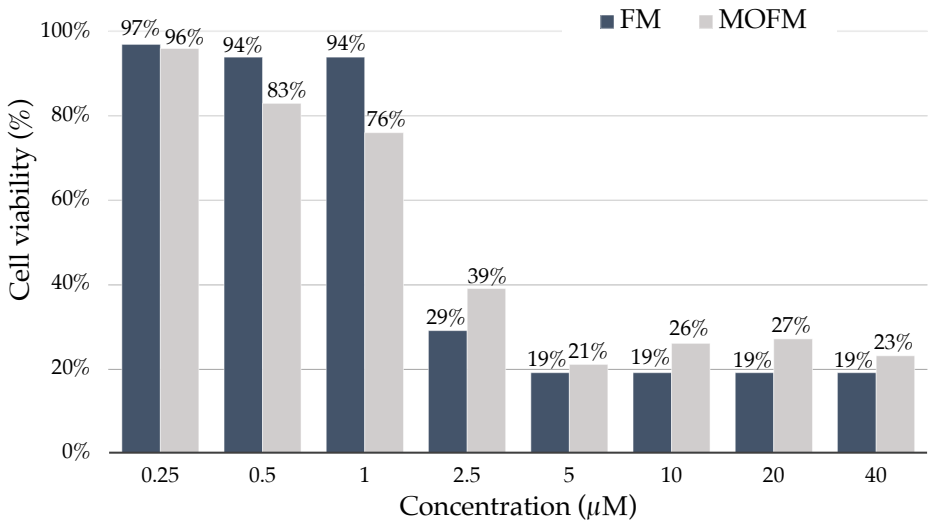

Figure 1.4: Cell viability after 24 hours incubation with **FM** (blue) and **MOFM** (grey).

Fig. 1.4 shows that cell viability severely decreases at concentra-

tion above 1 µM, indicating an increase in the toxicity of the compounds.

In order to maximize the signal of the dyes without incurring in undesired effects, for imaging experiments the dyes were used at a concentration of 1.5 µM but the incubation time was reduced to 30 minutes.

To evaluate weather **FM** and **MOFM** were internalized by the cells, the cells incubated with the dyes were imaged with a confocal microscope. The images obtained, reported in Fig. 1.5, confirmed the uptake of both **FM** and **MOFM**.

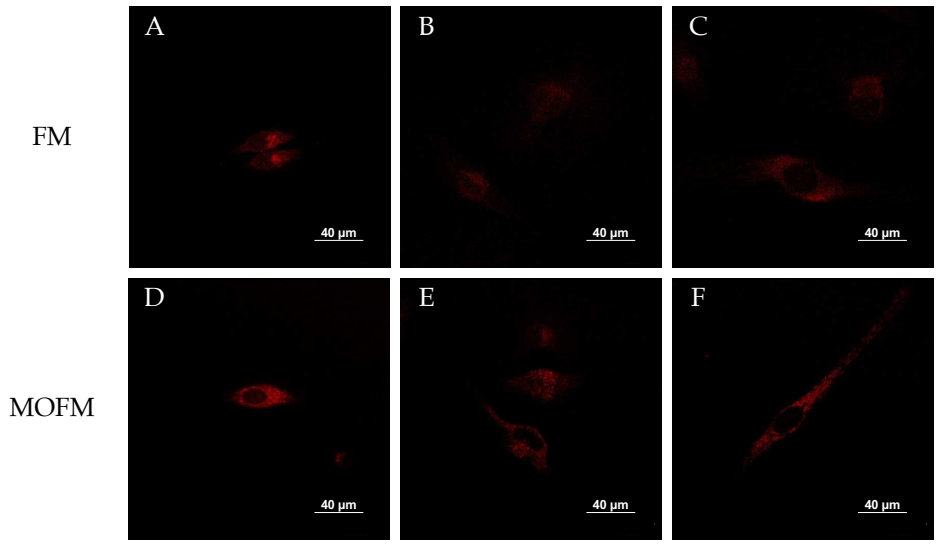

Figure 1.5: Images of cells after 30 minutes of incubation with **FM** and **MOFM**, using a concentration of 1.5 µM, an excitation wavelength of λ=561 nm and a detectable range of 600 nm-750 nm.

The emission spectrum of **MOFM** in cells was collected exploiting a dedicated detector of the confocal microscope (Fig. 1.6). Although the emission spectrum in cells could not be entirely acquired due to a limitation of the detector spectral range, the over-

lap with the spectrum acquired with the fluorometer on **MOFM** in a PBS solution indicates that the uptake did not damaged the dye which experienced a similar polarity in both PBS solution and cells.

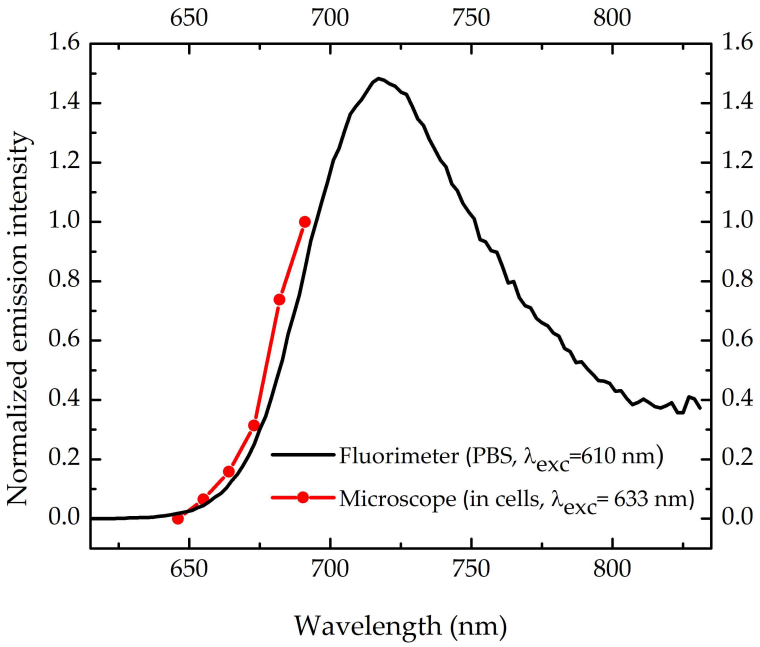

Figure 1.6: Emission spectra of **MOFM** in cells (red line) acquired with a confocal microscope and in PBS solution (black line) acquired with a fluorometer.

From Fig. 1.5 it is clear that the dyes do not localized ubiquitously in the cells, *e.g.* no signal is detected in the nucleus. To determine weather **FM** and **MOFM** were able to localize in specific organelles, colocalization experiments were carried-out.

Colocalization experiments are frequently used in cell biology studies to analyze the distribution of different dyes in the same cell. [37] Therefore, we investigated the colocalization of **FM** and **MOFM** with MitoTracker^{TM} Green (MTG), a commercial mitochondria tracker. The spatial overlap between the fluorescence signals of

the commercial dye and of our compounds provided information about the ability of **FM** and **MOFM** to track mitochondria.

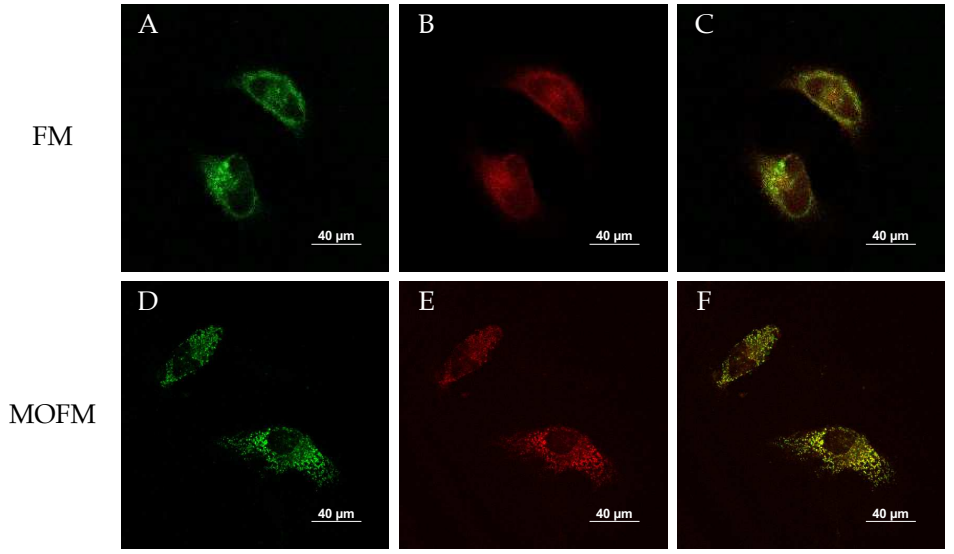

Figure 1.7: colocalization of **FM** and **MOFM** with MTG in HeLa cells. Panels A and D: MTG images. Panels B and E: **FM** and **MOFM** images. Panels C and F: merged images.

The images obtained from the colocalization assay are reported in Fig. 1.7. Panels C and F show the merging of MTG and **FM** or **MOFM** signals, respectively. Since MTG emission falls in the green spectral region and the emissions of **FM** and **MOFM** fall in the red spectral region, we obtain a yellow signal when the two dyes are located in the same region, *i.e.* are co-localized. Qualitatively, it is evident that both dyes are localized in the same spatial region as MTG, suggesting that they work as mitochondria tracker. However, from Fig. 1.7.C and F, it can be observed how the overlap between MTG and **FM** signals is worse that the one between MTG and **MOFM** ones. Indeed, the yellow signal in panel F is homogeneous while in panel C we can distinguish more reddish regions (higher con-

centration of **FM**) and more greenish ones (higher concentration of MTG).

The Pearson correlation coefficient (PCC) is often used to evaluate the degree of colocalization between two fluorophores. [38] The PCC values (r_P) range from -1 (worst colocalization) to 1 (best colocalization) and it is calculated automatically by images analysis softwares, *e.g.* ImageJ, following Eq. 1.1:

$$r_P = \frac{\sum_i (R_i - R_{av}) \cdot (G_i - G_{av})}{\sqrt{\sum_i (R_i - R_{av})^2 \cdot \sum_i (G_i - G_{av})^2}} \tag{1.1}$$

where R_i is the intensity of the first fluorophore in individual pixels and R_{av} the arithmetic mean, while G_i and G_{av} are the corresponding intensities for the second fluorophore in the same pixels.

The r_P calculated from the acquired images are $r_P = 0.79$ for **FM** and $r_P = 0.89$ for **MOFM**. Since both values are close to 1, it shows that both compounds selectively localize inside mitochondria, with **MOFM** having a stronger localization tendency compared to **FM**. For **FM**, having a lower Pearson coefficient, another colocalization experiment was performed using LysoTracker Green (LTG), a commercial lysosomes tracker.

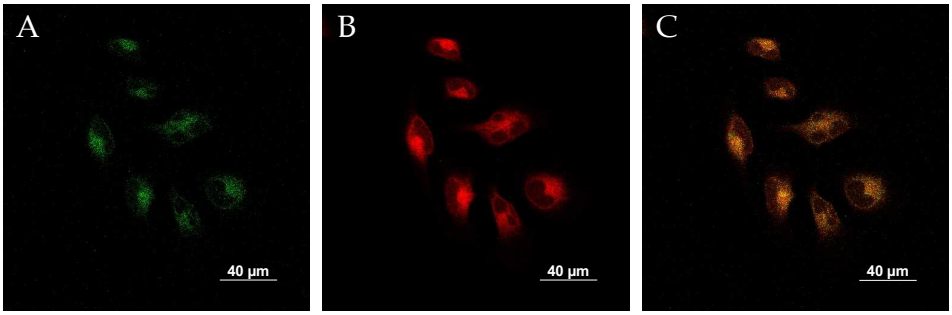

Figure 1.8: colocalization of **FM** with Lysotracker Green in HeLa cells. Panel A: Lysotracker Green image. Panel B: **FM** image. Panel C: merged image.

The images reported in Fig. 1.8 show the results obtained by the colocalization between **FM** and LTG: Fig. 1.8.C appears more orangeish compared to Fig. 1.7.C indicating a worse colocalization. Indeed, the r_P calculated for **FM** and LTG is 0.6, lower than the one calculated for **FM** and MTG.

1.4 A model for localization of neutral polar dyes in mitochondria

While for cationic trackers the physical localization mechanism is well understood, reports of neutral mitochondrial trackers often remain unclear or silent on their localization mechanism. In collaboration with Juraj Ovčar and Luca Grisanti, we developed a model for unveiling the mechanism of localization of polar neutral molecules in mitochondria.

The interior of the inner mitochondrial membrane was modeled as a phospholipid bilayer of palmitoyl-oleyl-phosphatidylcholine (POPC), while the intermembrane space and the mitochondrial matrix were considered aqueous solutions. [39, 40, 41] The total electrostatic potential of a one-dimensional inner mitochondrial membrane is then given by:

$$\Phi(x, \Delta\Psi_{\mathrm{NP}}) = \Phi_{\mathrm{P}}(x, \Delta\Psi_{\mathrm{NP}}) + \Phi_{\mathrm{W}}(x, \Delta\Psi_{\mathrm{NP}}), \tag{1.2}$$

where Φ_{P} is the electrostatic potential generated by the POPC bilayer, Φ_{W} is generated by water and $\Delta\Psi_{\mathrm{NP}}$ is the voltage drop across the membrane induced by a homogeneous electric field, stemming from the proton gradient established during the Krebs cycle. To fit a functional form of Φ, we utilized results from molecular dynamics (MD) simulations of the water-POPC bilayer system. [42] We set the origin $(x = 0)$ to be at the center of the POPC bilayer, with the intermembrane space being located in the $-\hat{x}$ direction from the phospholipid bilayer (i.e. $x \to -\infty$) and the mitochondrial matrix being located in the $+\hat{x}$ direction ($x \to +\infty$). The fitted curves obtained are shown in Fig. 1.9.

As can be seen from Fig. 1.10, the calculated electric field across the membrane indeed exhibits significant variation on the length scale of **FM** and **MOFM** ($\approx 10\,\text{Å}$), allowing for a net electrostatic force on the polar molecules. We considered a model in which we

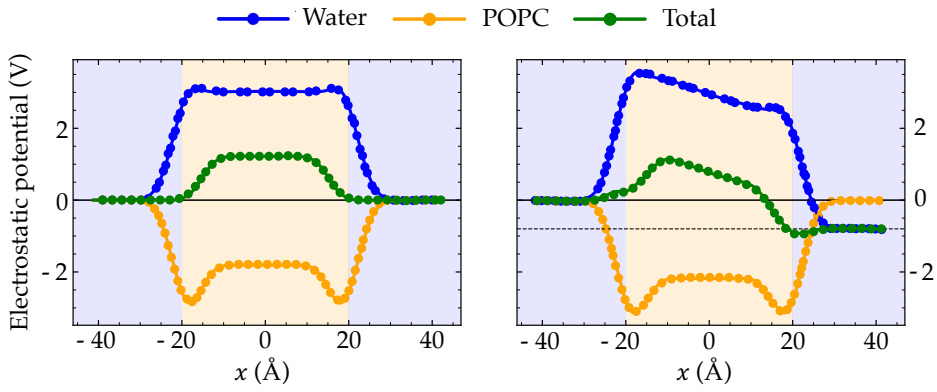

Figure 1.9: Functional forms of the inner mitochondrial membrane (full lines) and the data (scatter points) used to obtain them, shown for $\Delta\Psi_{\mathrm{NP}} = 0.0\,\mathrm{V}$ (left panel) and $\Delta\Psi_{\mathrm{NP}} = -0.8\,\mathrm{V}$ (right panel). The "Total" fitted curve is calculated as a sum of "Water" and "POPC" ones. The region containing predominantly water (POPC) is highlighted by the light blue (orange) background.

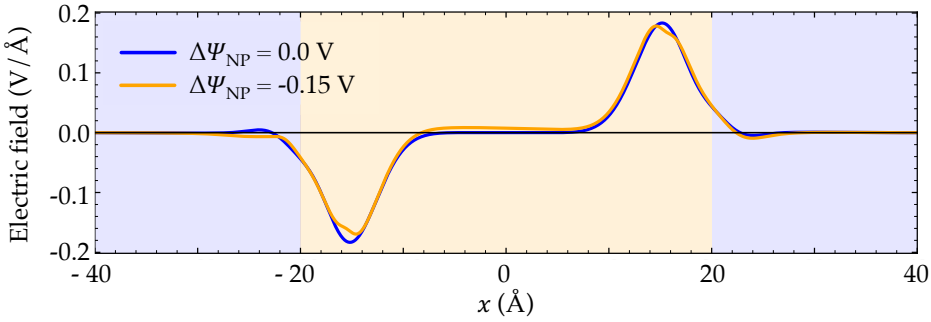

Figure 1.10: Electric field across the inner mitochondrial membrane for $\Delta\Psi_{\mathrm{NP}} = 0.0\,\mathrm{V}$ and $\Delta\Psi_{\mathrm{NP}} = -0.15\,\mathrm{V}$. The region containing predominantly water (POPC) is highlighted by the light blue (orange) background.

represent a molecule as a collection of N rigidly connected particles with respective masses m_i and partial charges q_i. The equations of motion for these particles in a spatially varying one-dimensional electric field $\vec{E}(x) = E(x)\hat{x}$ are:

$$m_i \ddot{x}_i = q_i E(x_i), \tag{1.3}$$

where x_i is the x-component of the position of particle i. Introducing a coordinate for the center of mass of the molecule as X, we can sum the equations of motion (1.3) to obtain:

$$M\ddot{X} = \sum_i^N q_i E(X + l_i), \tag{1.4}$$

where M is the mass of the molecule and $l_i = x_i - X$. Therefore, the net force experienced by the polar molecule is $F(X) = \sum_i^N q_i E(X + l_i)$.

In a stationary state, the molecule will be oriented in such a way that the dipole moment $\vec{\mu}$ is aligned with $\vec{E}(x)$. Let us fix $\{l_1, \ldots, l_N\}$, so that the dipole moment is parallel to the x-axis, i.e. $\vec{\mu} = \mu\hat{x}$. Then, the respective electrostatic potential energies $E_{\mathrm{p}}^{\pm}(x)$ for the two configurations with the dipole moment being (anti)parallel to the x-axis are simply:

$$E_{\mathrm{p}}^{\pm}(x) = -\int_{-\infty}^{x} F(x' \pm l_i)dx' = \sum_i^N q_i \Phi(x \pm l_i). \tag{1.5}$$

Note that x in eqn. (1.5) denotes the position of the molecular center of mass. To obtain the ionic point charges q_i, we calculate Mulliken charges from the ground state electronic density obtained by DFT optimizations of **FM** and **MOFM** in vacuum and water. We test different environments as it is not trivial to determine which is the most representative environment of the relevant realistic physical system. [43] It is known that the center of the inner mitochondrial membrane is non-polar, with the value of the

relative permittivity being $\epsilon \approx 2$, while the relative permittivity of the aqueous solutions representing the intermembrane space and the mitochondrial matrix is $\epsilon \approx 80$. [44, 43, 41]

Table 1.2: Ground state dipole moments (in Debye) of **FM** and **MOFM** in different solvents, calculated using the electronic density obtained with DFT (μ_ρ) and Mulliken charges (μ_M); electrostatic binding energies (in meV), calculated using Mulliken charges obtained in different solvents for dipole moments parallel (E_b^+) and antiparallel (E_b^-) to the x-axis

Molecule	Solvent	μ_ρ	μ_M	E_b^+	E_b^-
FM	Vacuum	12.346	13.253	-347	-326
	Water	22.918	23.084	-598	-561
MOFM	Vacuum	12.638	13.716	-353	-332
	Water	23.211	23.492	-606	-570

From Table 1.2, we can see that the dipole moments calculated using Mulliken charges agree well with the dipole moments calculated directly from the electronic density obtained using DFT. Furthermore, we note that both molecules have large dipole moments and are highly polarizable. The large dipole moment is a result of donor and acceptor groups connected at the two ends of the conjugated molecular unit, similarly to push-pull molecules.

The electrostatic potential energies calculated as per eqn (1.5), using Mulliken charges obtained in different solvents and using $\Delta\Psi_\mathrm{NP} = 0.15\,\mathrm{V}$, are shown on Fig. 1.11, with the binding energies $E_\mathrm{b}^\pm$ (minimal values of $E_\mathrm{p}^\pm(x)$) being listed in Table 1.2. We find that two binding sites at $x \approx \pm\, 16\,\text{Å}$ exist for both **FM** and **MOFM**. These positions are found within the phospholipid bilayer, as the lipid heads are located at $x \approx \pm\, 20\,\text{Å}$. [42] From Table 1.2, we observe that the binding energy of the site near the mitochondrial matrix (E_b^+) is consistently lower than the one of the site near the

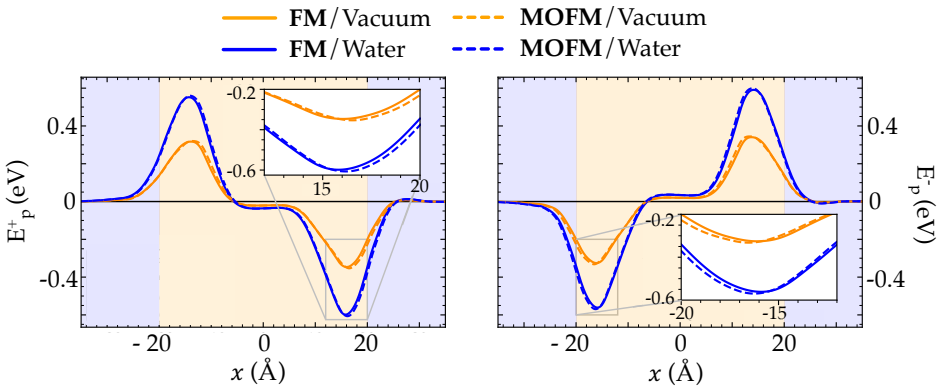

Figure 1.11: Electrostatic potential energy across the inner mitochondrial membrane as a function of the position of the molecular center of mass, calculated using Mulliken charges in vacuum and water for dipole moments parallel (left panel) and antiparallel (right panel) to the x-axis. The binding sites are shown magnified in the insets. The region containing predominantly water (POPC) is highlighted by the light blue (orange) background. The voltage drop across the membrane was set to $\Delta\Psi_{\mathrm{NP}} = -0.15\,\mathrm{V}$.

intermembrane space (E_{b}^{-}). This asymmetry in the binding energies between the two sites stems from the polarization of the POPC and water subsystems due to $\Delta\Psi_{\mathrm{NP}}$. Notably, we find that all calculated binding energies for **MOFM** are lower than the corresponding ones for **FM**, consistent with the experimental observation that **MOFM** has a larger tendency to localize in mitochondria compared to **FM**. Because of the difficulty in determining the most appropriate ionic charges (see discussion above), we consider the binding energies calculated using Mulliken charges obtained in vacuum (water) to represent the upper (lower) bound of the real electrostatic binding energy; however, we note that, due to the large solvatochromism of the considered molecules, the similarity in the measured emission spectra of **MOFM** in PBS ($\epsilon \approx 79$) and cells (Fig. 1.6) indicates that

the relevant physical environment could be best approximated by water.

To calculate the total binding energy, it is necessary to account for all molecule-membrane interactions other than the electrostatic one (e.g. hydrophobic, Van der Waals, steric and specific chemical interactions). This is difficult to achieve without the use of more complex methods, *i.e.* a detailed study of molecular permeation through the inner mitochondrial membrane. Thus, we decided to focus on a qualitative assessment of the aforementioned factors. Using a simple lipophilicity model, [45] we obtain $\log P = 3$ for both **FM** and **MOFM**, meaning that both molecules are significantly hydrophobic. This further enhances localization to the POPC bilayer. [40, 41] Steric and other factors have been shown to be of secondary importance in modeling hydrophobic ion interactions with membranes [43] and are unlikely to hinder localization within the POPC bilayer, especially considering the large electrostatic binding energy, high lipophilicity and the comparatively small size of **FM** and **MOFM** with respect to some of the larger lipophilic mitochondria trackers. [18, 19, 20]

Finally, we estimated the ratio of the concentrations of **FM** and **MOFM** localized in mitochondria. Due to the structural similarity of the considered molecules, we assume that the total binding energies of the two molecules significantly differ only in the electrostatic contribution. We can then use the following expression to approximate the ratio of concentrations of localized molecules:

$$\gamma = \frac{e^{-\beta E^{+}_{\mathrm{b,\,FM}}} + e^{-\beta E^{-}_{\mathrm{b,\,FM}}}}{e^{-\beta E^{+}_{\mathrm{b,\,MOFM}}} + e^{-\beta E^{-}_{\mathrm{b,\,MOFM}}}}, \tag{1.6}$$

where we calculated the thermodynamic β parameter using a temperature of 36 °C. The values of γ, calculated using the Mulliken charges obtained in vacuum and water are respectively 0.78 and 0.73, comparable to the ratio of the measured Pearson correlation

coefficients $(\mathrm{PCC}_{\mathbf{FM}}/\mathrm{PCC}_{\mathbf{MOFM}} \approx 0.89)$, which can also be interpreted as an approximation to the ratio of concentrations of localized molecules, showing that our model is quantitatively sound.

1.5 Conclusions and future perspectives

In this chapter was presented the full characterization of two novel neutral dyes synthesized by Kateryna V. Vygranenko and Daniel T. Gryko. The photophysical characterization was successfully performed both experimentally and theoretically thanks to the collaboration with Luca Grisanti and Juraj Ovčar. The cytotoxicity was determined thanks to *in vitro* assays performed by Shupei Yu, and the colocalization experiments allowed us to assess the ability of **FM** and **MOFM** to track mitochondria. Our study was pubblished on Organic & Biomolecular Chemistry on May 2024. [46]

In vitro assays are of paramount importance for assessing the features of new molecules of biological interest. Nevertheless, *in vitro* characterization presents several limitations for the full characterization of complex formulations. The main one is that cultivated cell lines oversimplify organ structures and sometimes are unable to reproduce the features even of the same cell type in an organism. [47] Not to mention the limitation in reproducing interactions between different cell types, extrapolating *in vivo* doses or determining the consequences of long term exposure. [48]

These limitations are partially overcome by 3D *in vitro* cultures: in 3D *in vitro* models the cells can grow in the three dimensions, respecting their native morphology; 3D models offer the possibility to cultivate different cell types and, thus, reproduce their relative interactions; lastly, in 3D models condition resembling the biological environment, like mechanical stimuli, nutritional and oxygen conditions etc. can be mimicked. [49]

One of the strategies to fabricate 3D *in vitro* models exploits microfluidic technology. To further explore the use of 3D models in our studies, I spent three months at Elvesys (now the Microfluidic Innovation Center) in Paris, to acquire the knowledge necessary to perform elemental tests on microfluidic chips (see Sec. 4.2).

Another approach to overcome limitations of *in vitro* experi-

ments involves the use of *ex vivo* animal models, that allow to test new formulations on almost intact tissue before moving to the *in vivo* phase. This is particularly interesting for drug delivery studies regarding topical applications, and requires specific microscopic techniques that allow the collection of 3D images, as multiphoton microscopy. In chapter 2 this strategy is applied to various drug formulations and tissues.

1.6 Materials and Methods

1.6.1 Spectroscopic measurements

UV-vis absorption spectra were recorded with a Tecan Infinite M200 PRO plate reader (at NJIT) or with a PerkinElmer Lambda650 spectrophotometers, in 1 cm path length cuvettes.

Fluorescence emission spectra were measured using an Edinburgh FLS980 (at NJIT) or an Edinburgh FLS1000 fluorometers on solutions with absorbance < 0.1 in 1 cm path length cuvettes.

Fluorescence quantum yields of **FM** and **MOFM** were measured using Cresyl Violet in ethanol ($\phi = 0.578$, from Ref. [50]) or Fluorescein in $NaOH_{aq}$ 0.1 M ($\phi = 0.90$) as standard.

Fluorescence anisotropy measurements were carried out using the Edinburgh FLS1000 fluorometers with two automatic polarizers (one in the excitation light path and the other in the emission light path). The anisotropy was measured for two glycerol solutions of **FM** and **MOFM** by exciting the sample with linearly polarized light and collecting the emission signal with parallel (I_{VV}) and orthogonal (I_{VH}) polarization with respect to polarization of the exciting light. Fluorescence anisotropy (r) is defined as follows:

$$r = \frac{I_{VV} - G \cdot I_{VH}}{I_{VV} + 2 \cdot G \cdot I_{VH}} \tag{1.7}$$

where I_{VV} indicates the intensity of the light emitted parallel to the excitation light polarization, and I_{VH} indicates the intensity of the light emitted orthogonal to the excitation light polarization. The G factor correction accounts for the different sensitivities of the detector to the vertical and horizontal polarization of the emitted light and it is defined as:

$$G = \frac{I_{HV}}{I_{HH}} \tag{1.8}$$

Anisotropy values can range from -0.2 and 0.4 depending on the fluorescence depolarization. When the anisotropy is measured on a rigid system, *e.g.* a molecule in a viscous or glassified solvent, the value is defined as "fundamental anisotropy", and depends on the relative orientation of the ground state and excited state transition dipole moments. If the two transition dipole moments are parallel, the anisotropy assumes its maximum value. [32]

Two-photon absorption bandshapes and cross section

The two-photon absorption (TPA) cross sections of two solutions of **FM** and **MOFM** in dichloromethane (DCM) were measured with the two-photon microscope available at University of Parma. A technical description of the two-photon microscope is reported in Sec. A.1.

The TPA bandshape was obtained by collecting the intensity of the emission falling in the detector dedicated to the red spectral region as a function of the excitation wavelength adopted to generate the signal. The correction curve for the wavelength dependent sensitivity of the excitation optics was applied to obtain the correct bandshape.

The absolute value of the cross sections was obtained by comparing **FM** and **MOFM** two-photon excited fluorescence (TPEF) intensity to that of a reference, a 12.4 µM (for **FM**) and a 10.9 µM (for **MOFM**) solution of Nile Red in DMSO, following a procedure described in the literature. [51, 52] The TPEF signal was acquired using the spectral detector (see Sec. A.1) and the correction for the wavelength dependent sensitivity of the detector was applied. The measurements were carried out using 1 cm quartz cells placed horizontally under the microscope objective. Distilled water was employed to dip the objective and the focal point was moved as close as possible to the upper cuvette wall, maximizing the signal intensity for each sample. The concentrations of the sample solutions

were 12 µM and 11.6 µM for **FM** and **MOFM**, respectively.

Due to the limited spectral range of the microscope detector, the emission spectra of **FM**, **MOFM** and the reference were only partially acquired. Nevertheless, in the acquired range the spectra were superimposable with the ones acquired with the fluorometer, confirming that the emitting state is the same for one- and two-photon excited fluorescence. Moreover, the TPEF integrated signal was multiplied for a correction factor accounting for the ratio between the integrated areas measured with the microscope and the fluorometer, respectively. Therefore, for each sample and for the reference, we assumed the same fluorescence quantum yield for one- and two-photon excited fluorescence. Following the procedure reported in the literature, [53] the TPA cross section of the sample ($\sigma_{2,\mathrm{new}}$) as a function of the excitation wavelength λ can be obtained as reported:

$$\sigma_{2,\mathrm{new}}(\lambda) = \frac{\phi_{\mathrm{ref}}}{\phi_{\mathrm{new}}} \frac{C_{\mathrm{ref}}}{C_{\mathrm{new}}} \frac{P(\lambda)^2_{\mathrm{ref}}}{P(\lambda)^2_{\mathrm{new}}} \frac{F(\lambda)_{\mathrm{new}}}{F(\lambda)_{\mathrm{ref}}} \frac{n_{\mathrm{ref}}}{n_{\mathrm{new}}} \sigma_{2,\mathrm{ref}}(\lambda). \tag{1.9}$$

where σ_2 is the TPA cross section, ϕ is the fluorophore quantum yield, C is the solution concentration, n is the refractive index, $P(\lambda)$ is the laser power at wavelength λ, and $F(\lambda)$ is the integral of the TPEF spectrum, evaluated after correcting the emission spectrum for the detector sensitivity. The subscripts "new" and "ref" refer to the sample and to the reference, respectively. The absolute values of $\sigma_{2,\mathrm{ref}}(\lambda)$ of Nile Red in DMSO were calculated using the same procedure using rhodamineB in methanol as reference ($\sigma_{2,\mathrm{rhodamineB}}(\lambda)$ taken from the literature [54]). TPA cross sections are expressed in Goeppert-Mayer units: 1 GM=1050 $\mathrm{cm}^4 \cdot \mathrm{s} \cdot \mathrm{photon}^{-1}$.

1.6.2 Cell viability

To perform the cytotoxicity assay, HeLa cells were cultured in the Dulbecco's Modified Eagle Medium (DMEM) supplemented with

10% fetal bovine serum, 1% penicillin/streptomycin at 37 °C in a humidified 5% CO_2. Cells were placed in 96 well plates and incubated until there are no fewer than $5 \cdot 10^3$ cells per well for the experiments. Stock solutions of **FM** and **MOFM** dissolved in DMSO were prepared at a nominal concentration of 1 mM respectively. Then, the stock solutions were diluted to the desired concentrations with DMEM (DMSO final concentration $\leq 1\%$ to avoid its cytotoxicity). [55] Next, cells were incubated with different concentrations of **FM** and **MOFM** (0.25 µM, 0.5 µM, 1 µM, 2.5 µM, 5 µM, 10 µM, 20 µM and 40 µM). After 22 h of incubation, the cell culture medium was replaced with a fresh one into each well and then 20 µL of the Cell Titer 96 Aqueous One solution reagent (for MTS assay) was added into each well, followed by further incubation for 2 h at 37 °C. The respective absorbance values were read on a Tecan Infinite M200 PRO plate reader spectrometer at 490 nm. Cell viabilities were calculated based on the following equation:

$$\text{Cell viability}(\%) = \frac{\text{Abs}^{S}_{490\ \text{nm}} - \text{Abs}^{D}_{490\ \text{nm}}}{\text{Abs}^{C}_{490\ \text{nm}} - \text{Abs}^{D2}_{490\ \text{nm}}} \cdot 100\%, \tag{1.10}$$

where $\text{Abs}^{S}_{490\ \text{nm}}$ is the absorbance of the cells incubated with different concentrations of experimental probe solutions, $\text{Abs}^{D}_{490\ \text{nm}}$ is the absorbance of cell-free well containing only **FM** and **MOFM** at the concentration that was studied, $\text{Abs}^{C}_{490\ \text{nm}}$ is the absorbance of cells alone incubated in the medium and $\text{Abs}^{D2}_{490\ \text{nm}}$ is the absorbance of the cell-free well.

1.6.3 Live cell imaging

All cells were seeded on confocal dish (MatTek) at the density of $4 \cdot 10^4$ cells per dish and incubated for 24 h at 37 °C and 5% CO_2. Stock solutions of **FM** and **MOFM** dissolved in DMSO were prepared at a nominal concentration of 1 mM respectively. The stock solutions were diluted to 1.5 µM with DMEM cell medium (DMSO

final concentration $\leq$ 1% to avoid its cytotoxicity) [55] and freshly placed over cells for a 30 min incubation period. Cells were washed three times with PBS, then the live cell imaging solution (Molecular Probes) was added to confocal dishes and the cells were imaged.

For colocalization assays after the three washes with PBS, the cells were further incubated with MitoTracker^{TM} Green (working concentration: 100 nM) or LysoTracker Green (working concentration: 75 nM), washed with PBS three times, and the live cell imaging solution (Molecular Probes) was added before the cells imaging.

1.6.4 Confocal imaging

Cells images were recorded with a Zeiss LSM 780 confocal microscope equipped with a C-Apochromat 40x/1.20 W Korr FCS M27 objective (pinhole 42.5 µm, airy 1 with respect to the blue channel; numerical aperture 1.20), available in the laboratory of Prof. K. Belfield at New Jersey Institute of Technology.

The confocal images were obtained detecting **FM** and **MOFM** by exciting the sample at 633 nm and acquiring the emission in the range between 645 nm and 750 nm (unless otherwise specified); MitoTracker^{TM} Green and LysoTracker Green by exciting the sample at 488 nm and acquiring the emission in the range between 495 nm and 550 nm.

Captures were taken at 40X magnifications (without zoom, pixel dwell 1.58 µs) to obtain detailed pictures of few cells with a field of view of 212.5 µm x 212.5 µm (512 x 512 pixels resolution, with a pixel size of 0.41 µm x 0.41 µm). The software ImageJ was used to process the images acquired and to determine the Pearson's correlation coefficients.

Chapter 2

Ex vivo experiments: characterization of drug delivery formulations in thick tissues

2.1 Introduction

Experiments conducted *ex vivo*, literally meaning "out of the living", are studies that involve the use of tissues or fluids extracted from their native environment. [56] *Ex vivo* analysis represents a bridge between *in vitro* and *in vivo* testing. [57] Indeed, while the first is useful but limited because of the simplicity of the model, the latter provides the most complete information but is complex, expensive, and could present ethical limitations. [58] On the other hand, *ex vivo* models have the advantage of preserving the structure of the native tissue under controlled conditions without the actual use of a living being. [59] *Ex vivo* animal models can be particularly useful for gaining insight on the mechanism of action of the drug in contact

with a target organ. [60] In particular, these models are valuable for the permeation study of drug delivery systems, especially for topical applications. [61]

One of the most used diffusion model to study drug permeation across tissues is the Franz diffusion cell, where the tissue is located between a donor chamber (where the formulation is placed) and a receiving one (where the permeated formulation accumulates and samples for quantification via HPLC or UV-vis are withdrawn). [62]

Analytical techniques used to characterize drug formulations can be combined with imaging to gain valuable information regarding the interactions between formulations and tissues. [63] Among imaging techniques, two-photon microscopy is suitable to image permeated thick tissues. [64, 65]. A detailed description of two-photon microscopy (2PM) is reported in Sec. A.1.

In this chapter, four different case studies are presented, focussing the attention on the advantages that two-photon microscopy can give in the study of formulation-tissue interaction compared to confocal microscopy.

The first two studies demonstrate the crucial role of 3D images and hyperspectral images in the characterization of formulations for drug delivery in ocular and skin tissues (see Sec. A.3 for the characterization of non-treated tissues with 2PM). On the other hand, the later studies illustrate how the ability to acquire images and spectra deep within thick tissues enables the investigation of formulation permeation capabilities.

2.2 3D resolution and hyperspectral images: the formulation fate

2.2.1 The hyaluronic acid - PVA film case

In the study presented in this section, two-photon microscopy is applied to the investigation of the interactions between the formulation and ocular tissues, specifically cornea and sclera.

Drug delivery to ocular tissues is a challenging topic due to the physiological features of this organ. Indeed, several static, dynamic, and metabolic barriers present in the eye prevent the effective permeation of drugs and an adequate retention time, leading to limited bioavailability. [66] For these reasons, our collaborators at the ADDRes lab of the Food and Drug department of the University of Parma are developing new formulations for improved delivery of drugs in ocular tissues. Among the various administration routes, inserts and implants answer predominantly to the need of a reduction of the administration frequency, since they allow for increased residence time in the site of application and a controlled release of the drug. [67, 68] The reduction of the administration frequency is of outmost importance since it increases adherence to the treatment while reducing fluctuations in drug tissues concentration and related side effects. Thus, both efficacy and patient's compliance are increased.

Taking these considerations into account, our collaborators developed an ocular film composed of polyvinyl alcohol (PVA) and hyaluronic acid (HA) for the controlled release of dexamethasone (DEX) and levofloxacin (LVX). Polymeric films containing PVA or HA have been previously investigated as ocular drug delivery systems: PVA is well known for its excellent film-forming properties and has been used, for instance, in combination with PVP to prepare films for the ocular release of progesterone, [69] while

films containing HA have demonstrated biocompatibility and an extended release profile. [70]

DEX is one of the most potent corticosteroids used for the treatment of diseases affecting both the anterior and the posterior eye segments, [71] while LVX is a drug approved in 1996, belonging to the fluoroquinolones family, a group of antimicrobial agents useful in the treatment of infections. [72] Since DEX is a poorly water-soluble drug, its loading in the HA and PVA hydrophilic films was possible thanks to the inclusion in cyclodextrins (HPCD).

Spectroscopic characterization

Two different films were prepared using HA, HPCD and PVA with different hydrolysis degree (PVA87 or PVA98) by our collaborators of the ADDRes lab (Fig. 2.1).

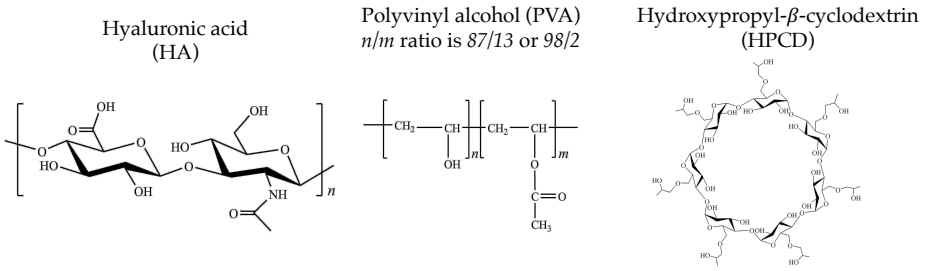

Figure 2.1: Molecular structure of PVA films components.

The films obtained were evaluated by our collaborators in terms of swelling, drug loading/release, and delivery capability. The physicochemical properties of the films changed with the type of PVA: PVA87-based films showed 3D swelling and a slower DEX release, while the PVA98-based film showed a 2D swelling and a faster DEX release. [73] On the other hand, when the release properties were evaluated on *ex vivo* tissue, no significant differences were observed between the two films interacting with cornea and

sclera. Thus, further 2PM analysis was carried out, testing only the PVA87-based film.

Once the physicochemical properties were fully addressed, 2PM analyses were performed to further study the penetration of the HPCD in two ocular tissues: sclera and cornea.

For this purpose, DEX was replaced by Nile Red (NR) that was solubilized in HPCD and loaded in PVA87-based films. NR was selected as fluorescent probe since it shares with DEX a low water solubility and similar size (DEX MW: 392.5 Da vs NR MW:318.4 Da). Additionally, the formation of an inclusion complex between NR and HPCD has been already reported in the literature [74, 75].

The preparation of PVA87-based film loaded with NR was conducted by our collaborators starting from the formation of NR-HPCD complex. To assess whether the inclusion of NR in the HPCD was successful, an emission spectrum was acquired on the obtained suspension and compared to the emission spectrum of a NR solution in water[1]. In fact, being NR a solvatochromic probe, [76] the spectral position of its emission changes with the polarity of the environment, allowing the differentiation between NR included in the HPCD and NR in water.

Fig. 2.2 shows emission spectra of NR in water and of NR-loaded HPCD in water. The spectrum of NR-loaded HPCD is blue shifted compared to the spectrum acquired on the NR solution in water, indicating that NR is experiencing different polarities when loaded in HPCD or in water solution. More specifically, the blue shift is ascribed to a less polar environment, a result that is compatible with the inclusion of NR in HPCD.

[1]Solution obtained by diluting in water a NR solution in DMSO until the percentage of DMSO in the final solution was <1%.

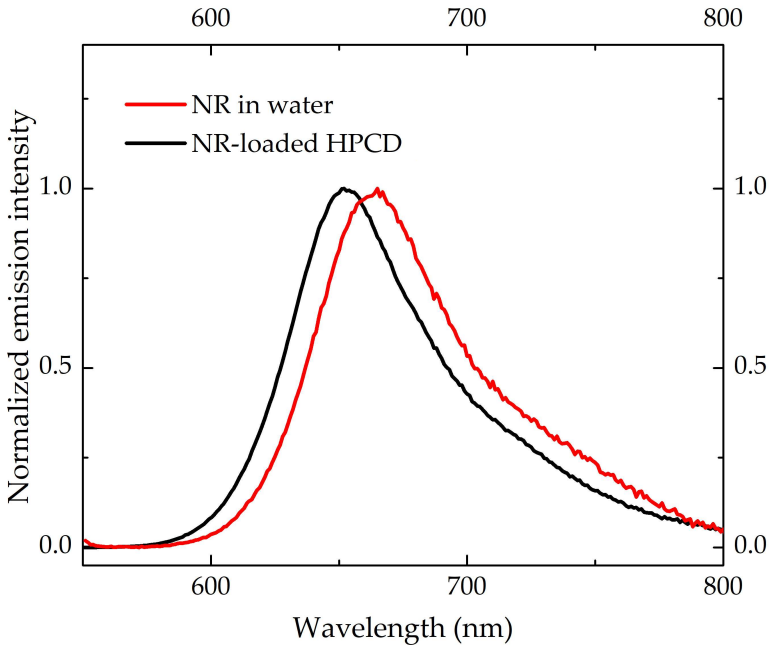

Figure 2.2: NR emission spectra acquired on NR-loaded HPCD and NR in water solution with the fluorometer ($\lambda_{exc} = 540\,\text{nm}$).

Two-photon microscopy characterization

Once the NR inclusion was confirmed, the PVA87-based films loaded with NR were prepared and the ocular tissues were treated (see Sec. 2.2.4 for details regarding the tissues treatment).

After the treatment, the tissues were placed in a dedicated plexigalss holder and imaged with an excitation wavelength of 1100 nm to maximize NR signal. The images collected on the corneal epithelium and stroma are reported in Fig. 2.3.

Panel 2.3.A shows corneal epithelial cells in orange. The orange color is the result of the superposition of the green cell autofluorescence [77] and the red emission of NR. On the other hand, Fig. 2.3.B shows corneal stroma characterized by the presence of

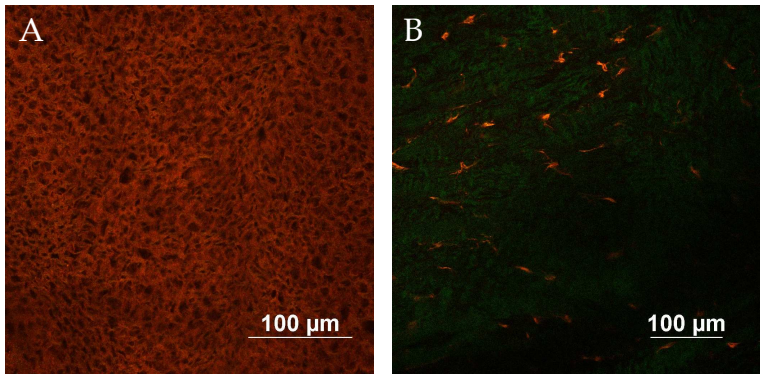

Figure 2.3: Two-photon microscopy images obtained on corneal tissue after irradiation at 1100 nm. Laser power and detector gains were adjusted for each sample.

collagen fibers detected thanks to the Second Harmonic Generation (SHG) signal (green for excitation at 1100 nm). [77, 78] For further details about SHG and the tissue structure see Sec. A.1 and Sec. A.3. Moreover, in the stromal matrix, several orange spots were detected: the orange signal is attributed to the presence of fibroblasts, cells that are commonly present in the stromal region (see Sec. A.3.1). From the images acquired, it is clear that NR accumulates inside the cells present in the corneal tissue.

A different outcome is obtained from the permeation in the scleral tissue. In Fig. 2.4 are reported the images acquired on the surface of scleral tissue and 50 µm below it.

In both images, an intense green signal was detected, due to the SHG generated by scleral collagen filaments (see Sec. A.3.1), and a less intense red signal, due to the presence of NR in the space between collagen fibers.

Thanks to the images acquired with the two-photon microscope, a first difference in the interaction between the film and the tissues was highlighted: in the cornea, NR is clearly localized in cells, both

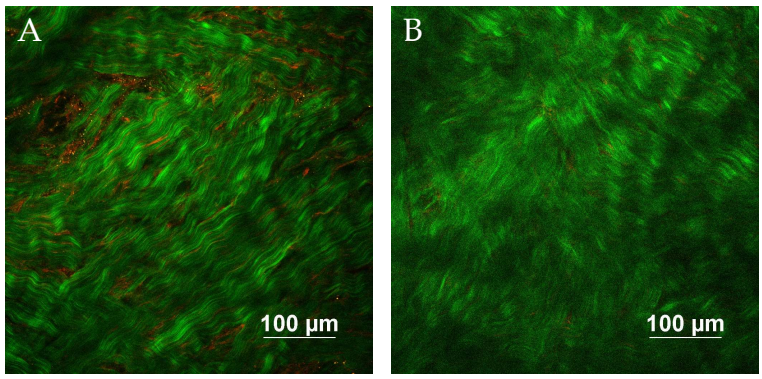

Figure 2.4: Two-photon microscopy images obtained on scleral tissue after irradiation at 1100 nm. Laser power and detector gains were adjusted for each sample.

epithelial cells and fibroblasts of the stroma, while in the sclera, an inter-fibrillar localization is observed.

Further information regarding the permeation mechanism can be inferred by the comparison of the NR emission spectra acquired on the tissues and on the water suspension of NR-loaded HPCD, exploiting NR solvatochromism. The emission spectra acquired on the treated tissues with the microscope are reported in Fig. 2.5.

The spectrum recorded on the treated cornea (Fig. 2.5, red line) is sizeably blue-shifted (25 nm) compared to the spectrum of NR-loaded HPCD (black line), suggesting that NR has been released from HPCD and is located in a less polar environment. [64] This is compatible with the NR localization inside the lipophilic domains of the epithelial cells.

A similar spectrum profile of NR is obtained also from the corneal stroma, confirming that the NR-HPCD complex dissociates in contact with the corneal surface or in the epithelial cells.

The spectral profiles obtained from the scleral surface (Fig. 2.5, blue line) and 50 µm below it (Fig. 2.5, green line) are not superim-

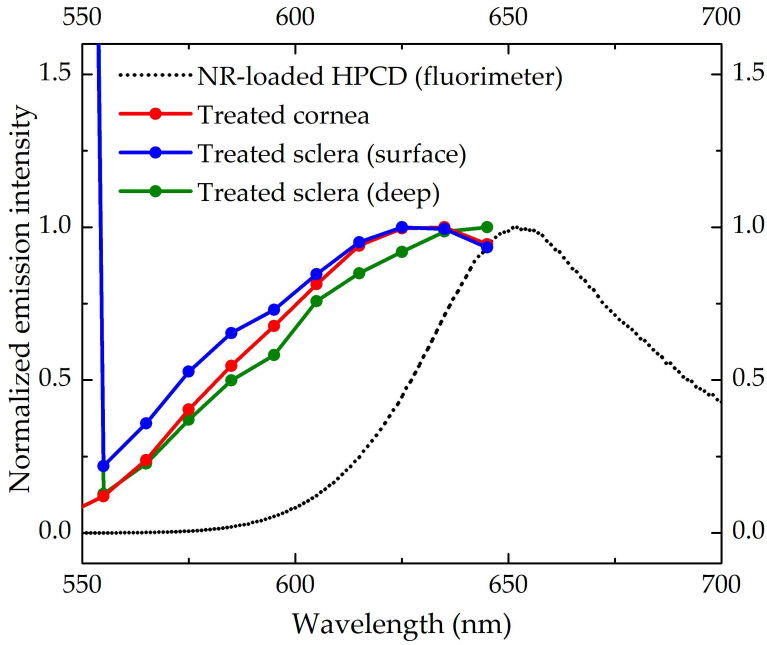

Figure 2.5: Emission spectra acquired on tissues ($\lambda_{exc} = 1080\,\text{nm}$) and on NR-loaded HPCD water suspension ($\lambda_{exc} = 540\,\text{nm}$).

posable: the one acquired on the surface resembles the spectrum acquired on the cornea, while the spectrum acquired 50 µm below the surface is slightly red-shifted. Since sclera is strongly hydrophilic, in case the NR was released from the HPCD, we would expect an emission spectrum resembling the NR emission in water (*i.e.* red shifted compared to NR-loaded HPCD). [64] However, the spectra recorded on the scleral tissue (blue and green line) are both blue-shifted compared to the NR-loaded HPCD and NR in water.

The blue-shift has been ascribed to the diffusion into the tissue of other film components such as HA, PVA or glycerin. These compounds would affect the hydrophilicity of the tissue and thus change the environment polarity and the position of NR emission. Moreover, it is reasonable to assume that the accumulation of those

compounds is higher in the first strata of the tissue altering the environment polarity on the surface more and, thus, leading to a greater blue-shift. While going deeper in the sample, the environment polarity tends to return to its native hydrophilicity and the NR spectrum shifts toward higher wavelength. Unfortunately, from the spectra acquired it is not possible to conclude whether NR is still included in the HPCD or not or if both conditions coexist.

2.2.2 New nanovesicles for topical skin delivery

Skin is the outermost and largest organ of our body and it is the first layer of defense against external elements such as pathogens, temperature, radiation etc. [79] Since skin is designed as a barrier, topical drug delivery is far from being trivial and has attracted the interest of many researchers. [80]

Nanotechnology-based drug delivery systems became remarkably popular in the past years due to their capacity of increasing drugs solubility and absorption and, thus, improving their bioavailability. [81] The most exploited nanotechnology in both drug delivery and cosmetic sectors are liposomes. [82] Although the several advantages that liposomes offer, *e.g.* protection of the loaded drug, controlled drug release and biocompatibility [83], their greater limitations concern the physicochemical properties and the stability that limit their application. [84]

Our collaborators from ICMAB and NanoMol Technologies SL designed a new self-assembled nanovesicle (NV) systems for drug delivery starting from β-sitosterol (Sit), a plant-based sterol, and lauryl glucoside (LGL), a sugar based surfactant (Fig. 2.6).

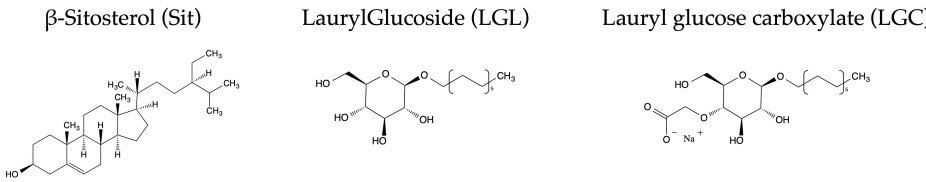

Figure 2.6: Molecular structures of the nanovesicles components.

Sit is a widely used phytosterol approved for cosmetic, food and pharmaceutical use. Sit is normally employed as a skin conditioner and shows several interesting properties for topical application such as antioxidant or anti-inflammatory activities. [85, 86, 87] LGL is a green, biocompatible and biodegradable non-ionic surfactant composed by a sugar moiety and fatty alcohol, [88] that is also

used and approved for cosmetics. Finally, to improve the colloidal stabilization, lauryl glucose carboxylate (LGC) was used as additive.

NVs composed by Sit:LGL:LGC in 1:0.8:0.2 ratio were produced by Marta Alcaina-Hernando (NanoMol Technologies SL) through the DELOS method, a single-step green methodology that uses compressed CO_2 as a co-solvent. [89, 90, 91] With this method, homogeneous, opalescent colloidal dispersions of NVs in water with 15% of ethanol (v/v) were obtained. Our collaborators produced the formulation and performed its physicochemical characterization.

Evaluation of skin integrity and of permeation with 2PM imaging

To better understand the interaction between the whole formulation and the skin tissue, four different studies were carried out employing 2PM:

1. skin treated with the dispersion medium
2. skin treated with the whole formulation (dispersion medium + NVs)
3. skin treated with the whole formulation loaded with Nile Red (NR)
4. skin treated with a NR solution in water as control

Although the *in vitro* skin irritation test carried-out by Marta Alcaina-Hernando at the ADDRes Lab of the University of Parma showed that the formulation had no irritant effect, it was pivotal to test whether the high percentage of ethanol could lead to undesired effects on *ex vivo* samples. Thus, skin tissues were treated with the dispersant media (experiment 1.) and with the whole formulation (experiment 2.) for 3 h and 6 h, and then imaged with the

two-photon microscope (Fig. 2.7). These experiments were carried out without staining: tissues were imaged using $\lambda_{exc} = 850\,\text{nm}$ to enhance tissue autofluorescence (due to endogenous fluorophores of skin tissue), while keeping the SHG signal (that at this excitation wavelength is at 425 nm) in a spectral region that is accessible by our experimental set-up (see Sec. A.1). The colors observed in Fig. 2.7 are due to the tissue autofluorescence (green) and to the SHG generated by the dermal collagen (blue) (see Sec. A.3.2).

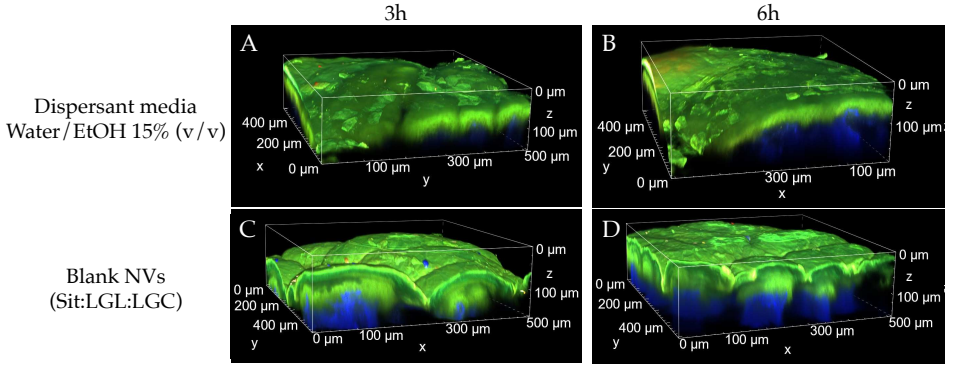

Figure 2.7: 3D renderings of the different skin samples. Panels A and B: dispersant media treatment (experiment 1.) and panels C and D: blank NVs treatment (experiment 2.). All images were collected exciting the samples at 850 nm, the laser power and detector gains were adjusted for each sample to prevent detector saturation.

The first stratum of skin epithelium looks different in the tissues treated with the dispersant media compared to the one treated with the whole formulation. Indeed, the stratum corneum (see Sec. A.3.2) in Fig. 2.7.A and B appears damaged, while in Fig. 2.7.C and D it looks intact. To highlight the status of stratum corneum after 6 h of treatment, the XY view of the previous 3D images were extrapolated and reported in Fig. 2.8.

Panel 2.8.A reports skin images collected from the tissue ex-

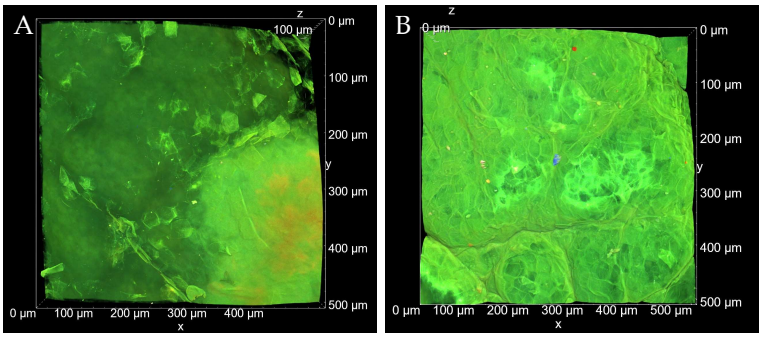

Figure 2.8: Panel A: XY view of a 3D reconstruction acquired on skin sample treated with the dispersant medium for 6 h. Panel B: XY view of a 3D reconstruction acquired on skin sample treated with whole formulation for 6 h. Images acquired exciting the samples at 850 nm.

posed to the dispersant medium: only a small portion of the stratum corneum (light green) appears intact and the inner strata of cells are visible (dark green). On the other hand, in Fig. 2.8.B, that shows the skin exposed to the whole formulation, the stratum corneum is well preserved and covers the whole surface of the sample.

This comparison allowed us to highlight the first important effect of the interaction between the formulation and the tissue: although the percentage of ethanol in the dispersant medium is high enough to lead to skin dehydration and the following disruption of the first layers of epithelial cells, the presence of NVs can actually mitigate this effect and protect the stratum corneum of the tissue. Moreover, we noticed that the treatment duration does not affect the tissue, as observed from the comparison between 3h and 6h experiemnts in Fig. 2.7.

To further investigate the permeation of NVs through the skin, NVs loaded with NR were prepared by our collaborators. As men-

tioned in Sec. 2.2.1, NR is a fluorescent probe extremely useful to highlight carrier-tissue interactions thanks to its solvatochromism. Thus, two full-thickness porcine skin specimens were treated with NR-loaded NVs for 3 h and 6 h while other two specimens were treated with a solution of NR in water/DMSO 1% (v/v)[2] and evaluated as controls. Both treatments were prepared to have the same final concentration of NR, *i.e.* 1.6 µM.

The samples were imaged using the same excitation wavelength employed in previous experiments (850 nm) and the 3D reconstructions obtained are reported in Fig. 2.9. The blue signal is SHG due to the presence of collagen (detected only in deep strata); the autofluorescence is green, while NR emission is orange/red.

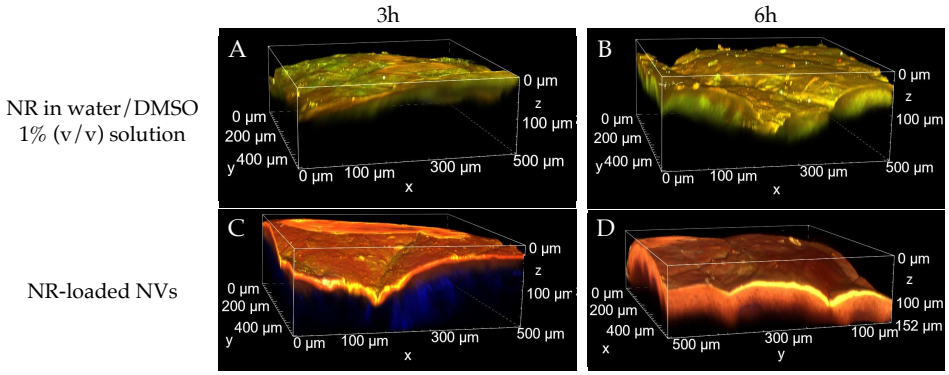

Figure 2.9: 3D renderings of the different skin samples. Panels A and B: NR water/DMSO 1% (v/v) solution treatment. Panels C and D: NR-loaded NVs treatment. All images were collected exciting the samples at 850 nm, the laser power and detector gains were adjusted for each sample to prevent detector saturation.

Looking at the images acquired on the specimens treated with the NR in water/DMSO solution (Fig. 2.9 panels A and B), it is clear

[2]Solution prepared by diluiting in water a solution of NR in DMSO until the proper concentration is reached. Final amount of DMSO < 1%

that the signal detected from epithelial cells is not homogeneous. Indeed, after 3 h of permeation (Fig. 2.9.A), the fluorescence signal detected on the surface presents regions with a more intense NR emission (orange/yellow regions) and others with a more greenish emission due to autofluorescence. On the other hand, after 6 h of permeation (Fig. 2.9.B), the signal acquired on the surface and in the first strata of the skin is more homogeneous and reddish, indicating a higher accumulation of NR. Nevertheless, the signal arising from the deeper strata of epidermis is mostly green, and hence is due to autofluorescence, indicating that the dye permeation is limited to the most superficial skin layers.

On the contrary, in Fig. 2.9.C and D the cells autofluorescence cannot longer be observed and the NR emission is the predominant signal throughout the whole epithelium.

From the 2D images reported in Fig. 2.10 more detailed information regarding the penetration of the treatments can be inferred. Indeed, the images acquired on the surface of the tissues (Fig. 2.10.A, E, I and M) show that the NR signal is homogeneous in all the samples but brighter when the tissue is treated with NR-loaded NVs. Conversely, from the images acquired 20 µm below the surface of the samples (Fig. 2.10.B, F, J and N) some differences between the treatments can be noticed. While the tissues treated with NR-loaded NVs still exhibit a homogeneous NR signal, those treated with NR in a water/DMSO suspension show both the dye signal and the tissue autofluorescence. Notably, the tissue treated for 6 h shows a stronger NR signal. The images acquired at both 40 µm and at 60 µm reveal a similar trend, with the tissues treated with NR-loaded NVs displaying a bright and homogeneous red emission, while the others exhibit a green signal over most of the imaged area.

Thus, the comparison between the images acquired on the differently treated specimens unveils another important feature of the formulation: the NVs enhance NR permeation and emission inten-

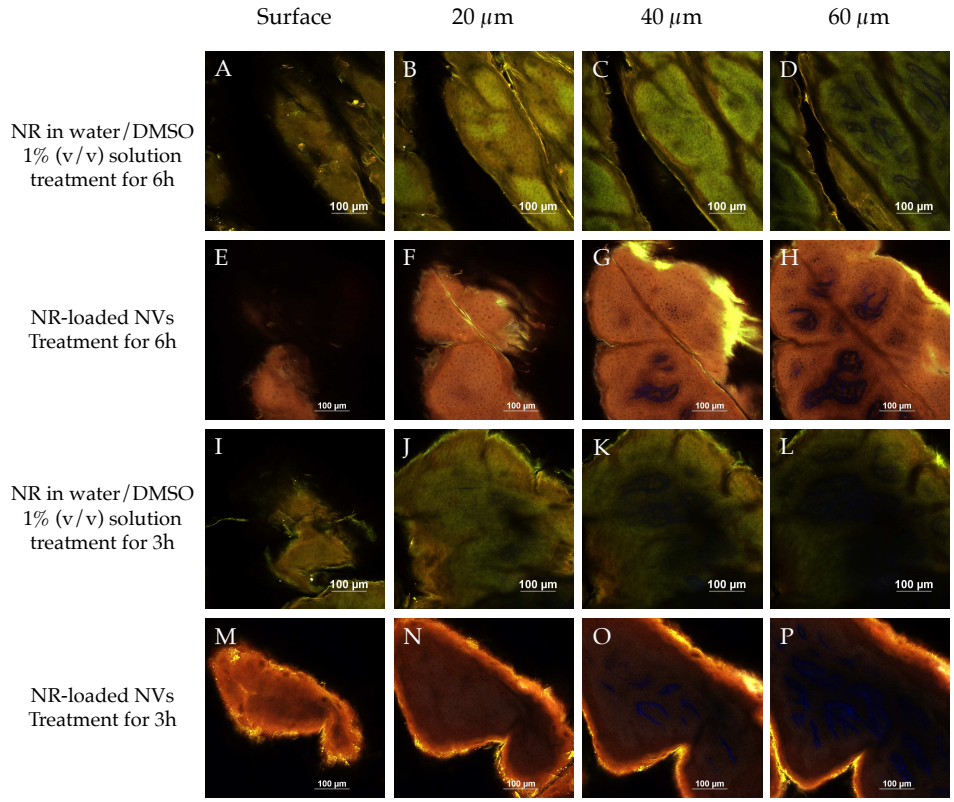

Figure 2.10: XY images acquired at different depths on skin samples differently treated. Panels A to D: NR in water/DMSO solution for 6 h. Panels E to H: NR-loaded NVs for 6 h. Panels I to L: NR in water/DMSO solution for 3 h. Panels M to P: NR in water/DMSO solution for 3 h. Images acquired exciting the samples at 850 nm, the laser power and detector gains were adjusted for each sample to prevent detector saturation.

sity by preventing the dye aggregation and thus, they increase the amount of active compound that is delivered in the tissue. Indeed, NR is a lipophilic dye with low solubility in polar solvents, that leads to aggregation and a decrease in its emission intensity in hy-

drophilic environments. [75]

From Fig. 2.10, it is also possible to gain insight about the NR location within the tissue. Interestingly, the treatment does not influence the final localization of NR: the dye is detected inside epithelial cells in all the images reported in Fig. 2.10.

To assess whether NR is released from NVs, the emission spectra acquired on both samples were compared with the emission spectrum collected on a water suspension of NR-loaded NVs (Fig. 2.11).

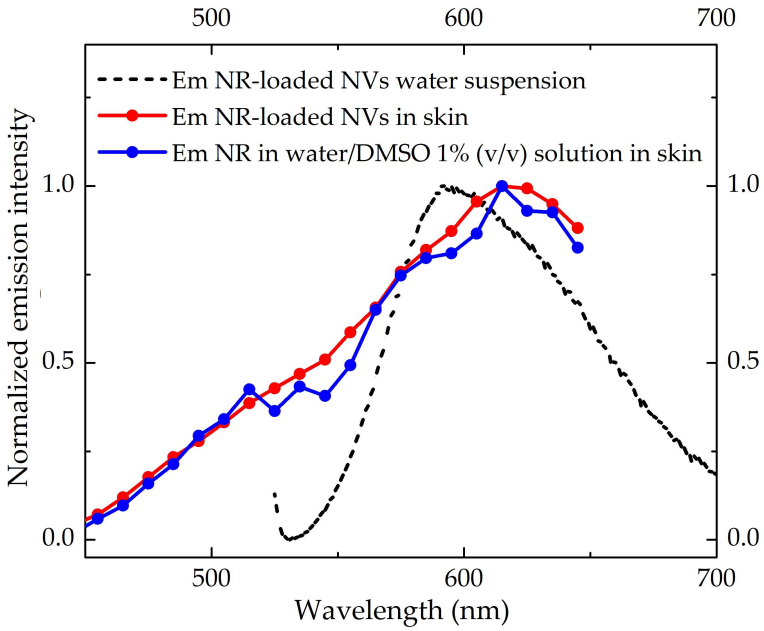

Figure 2.11: Emission spectra acquired on the differently treated skin samples 40 µm below the surface (red and blue lines) with the two-photon microscope exciting the sample at 850 nm and emission spectrum acquired on a water suspension of NR-loaded NVs (black line) with a fluorometer exciting the sample at 520 nm.

The emission spectra of the tissues treated with NR-loaded NVs and NR in water/DMSO solution fall in the same spectral region

and their maxima are shifted towards higher wavelength compared to the spectrum acquired on the water suspension of NR-loaded NVs. This spectral shift, combined with the images, indicates that, regardless of the vehicle, NR permeates in the tissue and enters the cells without the carrier. Thus, the comparison between the spectra acquired indicates that the NVs release NR once in the tissue.

2.2.3 Conclusions and future perspectives

The case studies presented in Sec. 2.2.1 and Sec. 2.2.2 show how the acquisition of 3D images and emission spectra can be exploited to gain pivotal information regarding the interaction between formulation and tissues.

In both studies, the location of the fluorescent probes in the tissues was clearly inferred from the 2D and 3D images. Moreover, the use of solvatochromic dyes allowed us to obtain crucial information regarding the release of the fluorescent cargo from the delivery system. By coupling the results obtained from the two measures important insights on the carrier behavior inside the target tissue can be gained.

In Sec. 2.2.1 the characterization of a novel formulation for the topical administration of dexamethasone and levofloxacin in *ex vivo* eye tissues was presented. Two-photon microscopy allowed to visualize the treated tissues complementing the characterization performed by Martina Ghezzi at the ADDRess lab at the University of Parma. Notably, thanks to the acquisition of hyperspectral images at different depths of both tissues, different interactions between the formulation and the corneal and scleral tissues were observed. Indeed, in cornea a clear location of NR in cells after the release from HPCD was evaluated, while the interaction with the scleral tissue was more complex to assess. From the images, it was observed the accumulation of NR in the space between collagen fibers and from the spectra an influence from the other film components was highlighted, although it was not possible to clearly demonstrate whether NR was released from HPCD.

The work presented in Sec. 2.2.1 was published on the International Journal of Pharmaceutics in May 2023. [73]

In Sec. 2.2.2, the characterization of a novel formulation for the topical administration in skin tissue was evaluated on *ex vivo* porcine samples. The two-photon analysis complemented the characteriza-

tion performed by Marta Alcaina-Hernando at ICMAB, Nanomol and at the ADDRess lab and helped to unveil crucial information regarding the formulation interactions with the tissue. The comparison between the 3D images acquired on differently treated tissues allowed to highlight the capacity of the nanovesicles to prevent skin dehydration caused by the high percentage of ethanol in the formulation and their ability to enhance NR permeation and prevent its aggregation. Moreover, the hyperspectral images acquired on the tissues were pivotal to understand that the NVs released NR inside the epithelium, a pivotal feature for carriers exploited in the treatment of topical diseases or in the cosmetic sector.

The work presented in Sec. 2.2.2 was published on Applied Materials Today in December 2024. [92]

Further information in drug delivery investigations could be achieved by conducting experiments with fluorescent drugs that would allow to directly study the interaction between the whole formulation and the tissue and to assess the final location of the active pharmaceutical ingredient inside the biological target. Indeed, ongoing studies are exploiting formulations containing ofloxacin, a fluorescent antibiotic.

2.2.4 Materials and Methods

Ex vivo permeation of NR-loaded PVA87-based film

Porcine eyes handling was performed by Martina Ghezzi. Porcine eyes were provided by a local slaughterhouse and were explanted within 3 h from animal death (pig breed, Large White and Landrance; weight, 145–190 kg; age, 10–11 months; sex, male and female). Eye bulbs were transported to the lab in PBS buffer; the adherent muscle and the conjunctiva were removed. Porcine eyes were dissected to isolate the sclera. For corneal experiments only bulbs with macroscopically intact corneas were employed, whereas eyes showing opaque corneas were discarded. During the dissection to isolate sclera, the anterior segment of the eye was circumferentially cut behind the limbus and discarded. The vitreous was removed, the eye cup was cut into two halves and retina and Retinal Pigment Epithelium (RPE) were removed by using a cotton swab to obtain the trilayer composed of sclera, choroid and Bruch's layer. When the isolated sclera was used, the choroid was eliminated by careful removal with tweezers.

The permeation experiments were performed by Martina Ghezzi using a Franz-type vertical diffusion cells (area 0.6 cm^2 for sclera and 0.2 cm^2 for cornea). The tissues were clamped between the donor and the receptor compartments. The receptor compartment contained 4 mL of pH 7.4 PBS kept at 37 °C, and magnetically stirred. Before film application, the tissues were wetted with 24 µL of PBS to favor film adhesion to the tissue. Then, the NR-loaded films were applied to cornea and sclera for 4 h. After the permeation experiments, the samples were frozen at −20 °C until 2PM imaging.

Ex vivo permeation of NR-loaded NVs

Skin experiments were carried out by Marta Alcaina-Hernando and Silvia Pescina using porcine tissues. Porcine skin samples come

from a local slaughterhouse. They were isolated through a scalpel from the cartilage and correspond to the outer part of pig ears (both 10–11 months age male and female from Large White and Landrace, ranging in weight from 145 kg to 190 kg). Skin samples were frozen at $-20\,^{\circ}C$ and used within 3 months. Thawed skin sample was mounted on glass Franz-type diffusion cells (DISA, Milano, Italy; $0.6\,cm^2$ surface area) with the stratum corneum facing the donor compartment. Donor compartment was filled with 200 µL of NVs systems Sit/LGL/LGC (1:0.8:0.2) or NR-loaded NVs systems Sit/LGL/LGC (1:0.8:0.2) or the dispersant medium water/EtOH 15% (v/v) or the water solution of NR. The receiving compartment was filled with saline solution (0.9% NaCl) previously degassed and kept at $37\,^{\circ}C$ under magnetic stirring. After 3 h or 6 h the donor was carefully removed, the surface washed three times with saline solution and gently cleaned with filter paper. Then the cell was dismantled and the area of the skin sample in contact with formulation punched (area $0.6\,cm^2$), placed in the dedicated plexiglass holder and visualized via two-photon microscopy.

2.3 Deep strata imaging: how efficient is the formulation penetration?

2.3.1 siRNA trimethyl chitosan nanoparticles case

In this section the study of a novel formulation for the intranasal delivery of RNA interference to the brain is presented.

The group of Prof. Fabio Sonvico at the Food and Drug department of the University of Parma is specialized in the drug delivery through nasal tissue. They synthesized and characterized the physicochemical properties of trimethyl chitosan nanoparticles for the delivery of siRNA to the brain. 2PM analysis was exploited to study the mucopenetration and mucoahdesion of the formulation on rabbit nasal mucosa.

RNA interference (RNAi) is a promising therapy for genetic diseases and cancer. The term "RNAi" indicates a pathway capable of silencing specific gene expression in mammalian cells. [93] RNAi is mediated by three kinds of small RNA: microRNA (miRNA), small interfering RNA (siRNA) or short hairpin RNA (shRNA). siRNA is a synthetic short double-stranded RNA that can be directly incorporated into the RNA-induced silencing complex (RISC). Once activated, RISC is able to identify and degrade messenger RNA (mRNA) or block its translation, leading to the gene suppression. [94]

Although gene therapy reduces the side effects of non-targeted treatments, its main limitation is the delivery. [95] Indeed, siRNA is an anionic macromolecule which struggles to cross the cellular membranes and has a very short half-life due to its enzymatic degradation. [96] For the delivery of siRNA both viral and non-viral vectors have been considered: while viral vectors are more effective, non-viral vectors represent a safer option for the patient since they are less immunogenic and easier to synthesize. [97]

Among the several vectors, nanoparticles (NPs) are a valuable RNA delivery system. Specifically, NPs based on cationic lipids or polymers have been frequently studied for gene delivery. [98]

Chitosan is a natural cationic polysaccharide, studied in gene therapy for its absorption enhancement, excellent mucoadhesive properties, biocompatibility, biodegradability, and low cost of production. [99] However, the primary amine of chitosan (pKa = 6.5) limits its solubility, that indeed is low at neutral and alkaline pH, allowing its use only in body areas with acidic pH. [100] To overcome this limitation, synthetic derivatives of chitosan were developed and investigated. Notably, trimethyl chitosan (TMC) conserves the quality of its precursor with improved solubility and permeability. [101]

Thus, our collaborators developed and characterized a novel TMC nanoparticle formulation capable of encapsulating siRNA for intranasal delivery. Two-photon microscopy was exploited to evaluate the adhesion and penetration of the formulation on *ex vivo* rabbit nasal tissues. To perform 2PM analyses the formulation was labeled with cyanine3 (Cy3).

Mucoadhesion characterization

Mucoadhesion studies were performed by comparing the images and spectra of tissues exposed to the Cy3-siRNA loaded TMC NPs with blank tissues and tissues exposed to Cy3-siRNA solution. *Ex vivo* rabbit nasal mucosa was prepared following the procedure described in Sec. 2.3.4 and imaged at $t = 0$ and after $t = 30$ min of washing (Fig. 2.12).

Both tissue autofluorescence and Cy3 emission fall mainly in the green spectral region (Fig. 2.12). Although some differences between blank and treated tissues can be observed, the acquisition of emission spectra is pivotal to assess the presence of the Cy3 dye on tissues surface (Fig. 2.13).

The difference between autofluorescence and Cy3 emission is

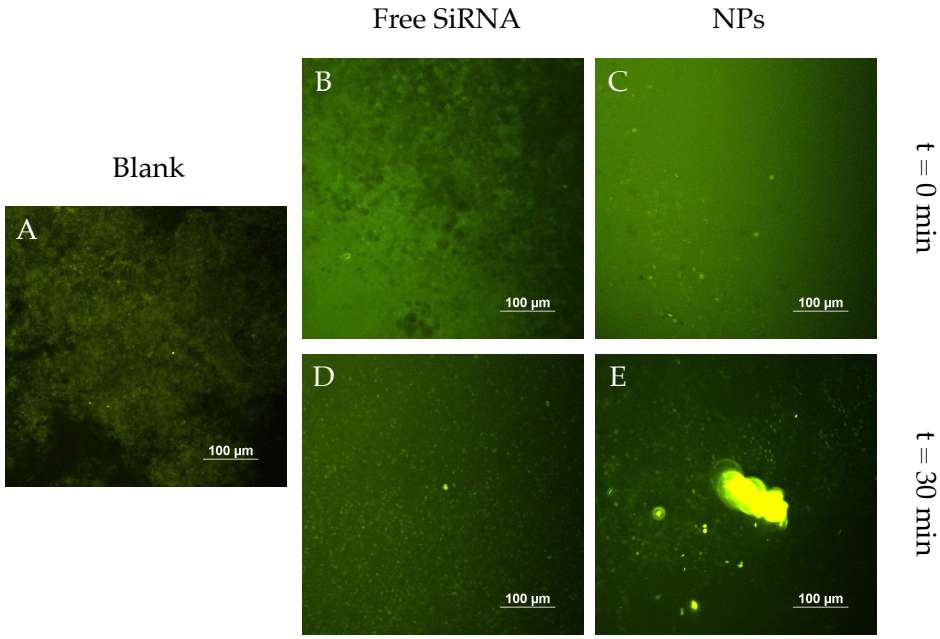

Figure 2.12: Images acquired on the rabbit nasal mucosa surface. Panel A: Blank mucosa. Panels B & C: mucosa treated with Cy3-siRNA solution. Panels D & E: mucosa treated with Cy3-siRNA loaded TMC NPs. The images reported in panels B-E were acquired in the same experimental conditions with λ_{exc} =1000 nm.

clear from the analysis of emission spectra (Fig. 2.13): the first is a broad band, while the second presents the characteristic shape of Cy3 emission, with the resolved vibronic structure. [102] Autofluorescence is significantly less intense than Cy3 emission, and in samples containing Cy3, the autofluorescence signal becomes indistinguishable. The Cy3 emission is present on both treated samples even after the 30 min washing period. Nevertheless, after washing, the intensity of Cy3 emission was much lower for the free Cy3-siRNA compared to the Cy3-siRNA loaded TMC NPs, confirming the better mucoadhesion of the formulation.

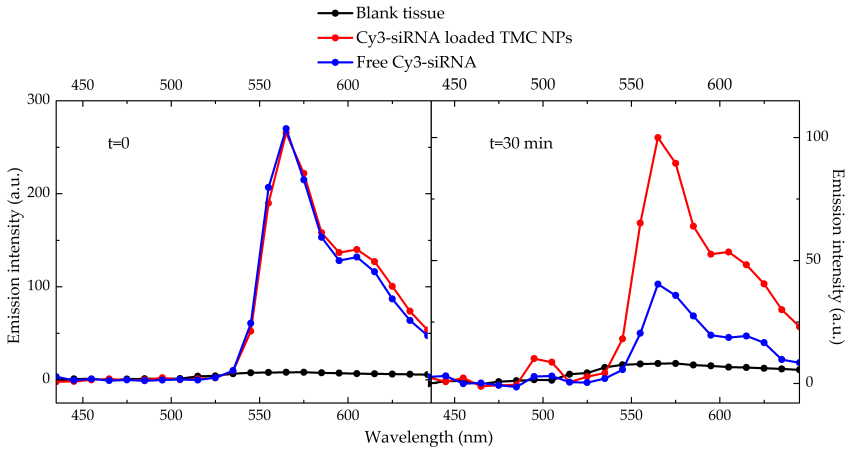

Figure 2.13: Emission spectra acquired on rabbit nasal tissue as such (black line) or treated with Cy3-siRNA loaded TMC NPs (red line) or the free Cy3-siRNA (blue line). All the emission spectra have been acquired in the same experimental conditions with λ_{exc} =1000 nm.

Additionally, after the treatment with Cy3-siRNA loaded TMC NPs, several aggregates were visible on the tissue, possibly because of the interaction between the NPs and the mucins present on the surface of nasal mucosal tissue (Fig. 2.12.E), further confirming an increased adhesion to the mucosa.

Mucopenetration characterization

To evaluate the mucopenetration of the formulation two nasal tissues have been analyzed by 2PM acquiring 3D images at different time points after the deposition of 20 µL of Cy3-siRNA loaded TMC NPs or free Cy3-siRNA on the mucosal surface. A blank tissue was also imaged as reference. For these analyses, the excitation wave-

length was set to λ_{exc} =950 nm with the aim to detect the SHG that arises from collagen present in the deepest strata of the tissue, while maintaining a good excitation of Cy3 (at 1000 nm SHG cannot be detected with NDD detectors, since the NDD detectors are blind around 500 nm, see Sec. A.1).

In Fig. 2.14 the 3D reconstructions, acquired on the blank tissue on the tissue treated with Cy3-siRNA loaded TMC NPs, are reported.

On the surface of the blank tissue (Fig. 2.14.A) a green emission was detected, similar to the one already observed in Fig. 2.12.A, while deeper in the tissue a blue signal was observed due to the SHG generated by the collagen. When looking at the 3D reconstructions of the tissues treated with Cy3-siRNA loaded TMC NPs, a strong green-yellowish signal, due to Cy3, is detected. In Fig. 2.14.B ($t = 0$) the Cy3 signal is mainly located on the surface, while after only 20 min its intensity decreases on the surface and increases in the deeper strata.

Thanks to the 3D images acquired at different time points, the data about the progressive penetration of the formulation across the tissue over two hours were accessible. Moreover, as indicated by the white arrows in Fig. 2.12, the penetration of the formulation seems to be promoted by the presence of channels generated by the cell organization in the tissue.

A further evidence of the mucopenetration of TMC NPs loaded with Cy3-siRNA was obtained thanks to the acquisition of emission spectra on both the treated tissue and the blank one at 300 µm below the surface after 60 min of permeation (Fig. 2.15).

In Fig. 2.15 two distinct signals are detected: the Cy3 emission indicated by the green arrow and the SHG of collagen pointed-out by the blue arrow. As expected, in the spectrum acquired on the blank tissue, only the SHG signal is detected while, in the spectrum acquired on the treated tissue, the Cy3 signal is present together with the SHG one.

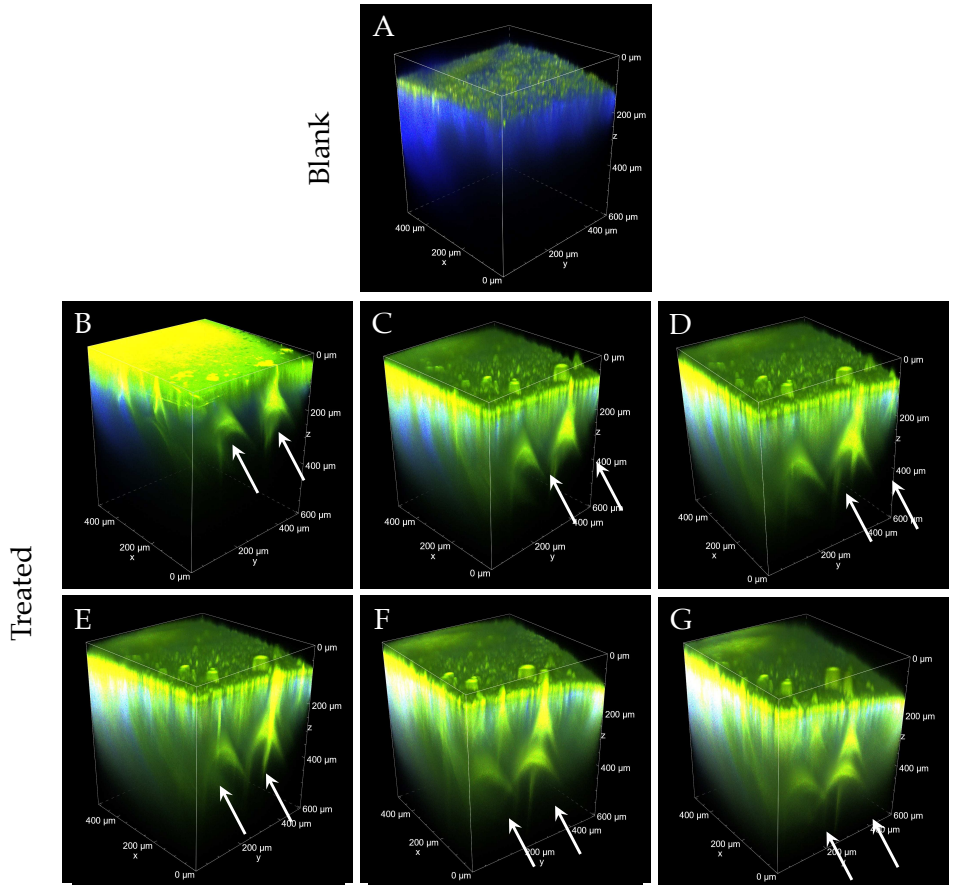

Figure 2.14: 3D images of the nasal mucosa treated with Cy3-siRNA loaded TMC NPs obtained with λ_{exc}=950 nm. Panel A: blank tissue. Panel B: $t = 0$. Panel C: t =20 min. Panel D: t =40 min. Panel E: t =60 min. Panel F: t =90 min. Panel G: t =120 min.

Thus, the spectra confirmed what was observed from the images: the TMC NPs promoted a deep penetration of Cy3-siRNA.

On the other hand, the sample treated with free Cy3-siRNA was analyzed with an excitation wavelength of 1000 nm. Indeed, in this case we preferred to maximize the Cy3 signal since no SHG could

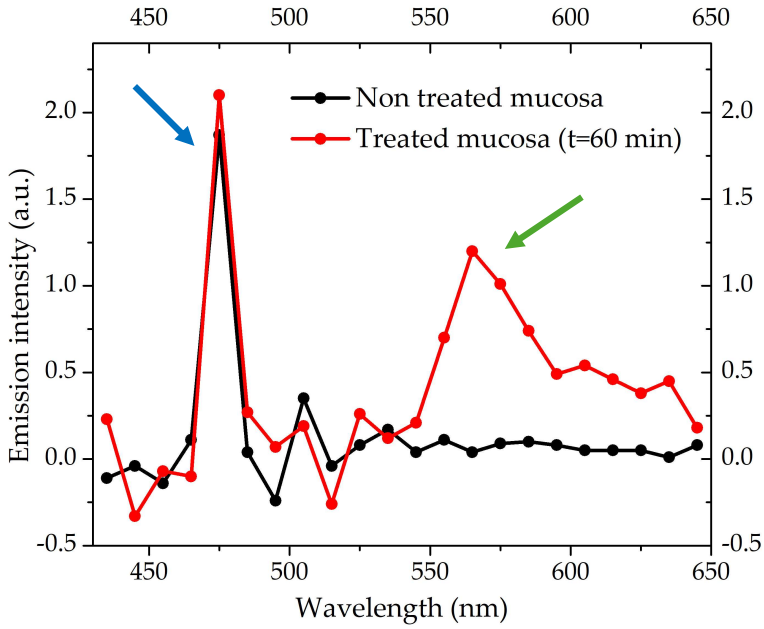

Figure 2.15: Emission spectra acquired at 300 µm of depth in the blank mucosa and after the permeation of Cy3-siRNA loaded TMC NPs with λ_{exc} =950 nm. Blue arrow indicates the SHG signal, while green arrow shows Cy3 emission.

be detected.

The images in Fig. 2.16 show the XZ view of the 3D reconstructions acquired on the tissue treated with free Cy3-siRNA at different time points.

In all XZ views, two distinct regions are present: a brighter one at the top, corresponding to the Cy3-siRNA solution, and a darker one at the bottom, corresponding to the mucosal tissue. Comparing the images at different time points, it is evident that the thickness of the Cy3-siRNA signal decreases over time, but no changes are observable on the surface of the nasal tissue. This behavior is compatible with the spreading of the treatment on the mucosal tissue

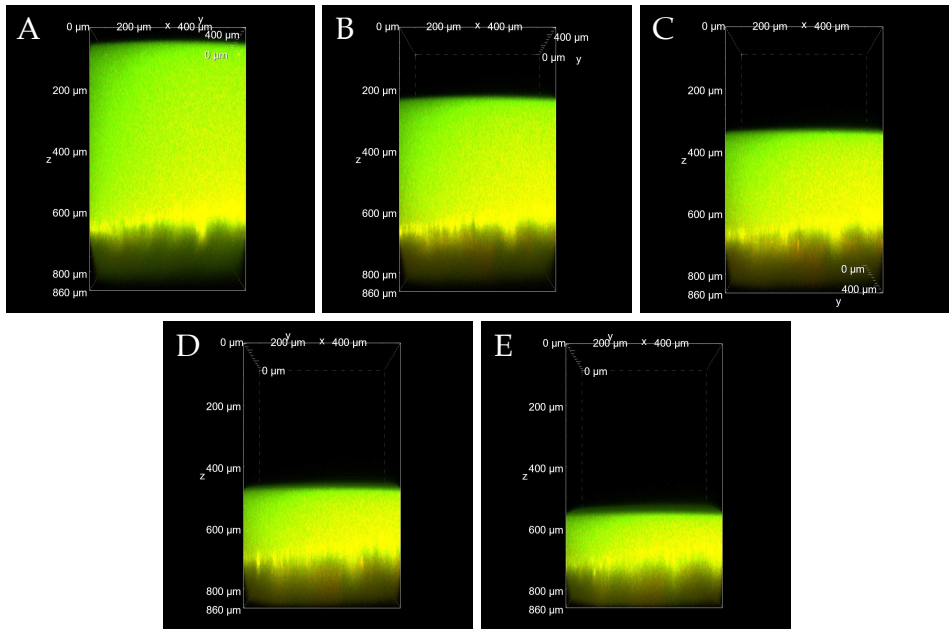

Figure 2.16: XZ views of the 3D images acquired on the nasal tissue treated with the free Cy3-siRNA at different time points with λ_{exc}=1000 nm. Panel A: $t = 0$. Panel B: t =10 min. Panel C: t =20 min. Panel D: t =35 min. Panel E: t =45 min.

and indicates that the penetration of the solution inside the tissue is limited.

To assess the differences in the permeation of the treatments over time, the comparison between the signal collected in the green channel for both experiments was performed (Fig. 2.17). From Fig. 2.17, it is clear that the NPs enhance the permeation of Cy3-siRNA within the nasal tissue. After only 20 minutes of permeation, the signal observed from the NPs at a depth of 200 µm showed an almost 4-fold increase when compared to the initial value, while the signal of the free Cy3-siRNA remained almost constant throughout the experiment.

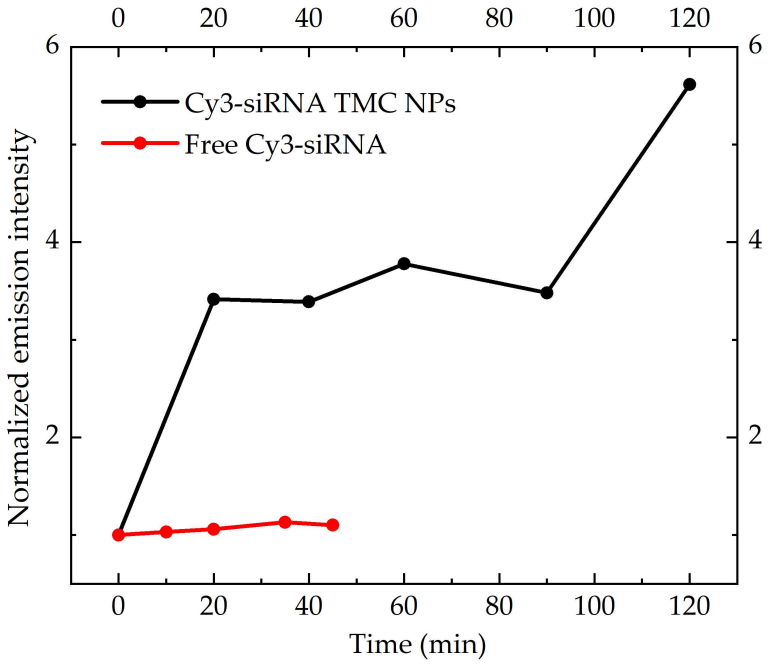

Figure 2.17: Comparison of Cy3 signal variations after treating the rabbit nasal tissue with Cy3-siRNA loaded TMC NPs acquired 200 µm below the surface with $\lambda_{exc} = 950$ nm or free Cy3-siRNA, acquired 150 µm below the surface with $\lambda_{exc} = 1000$ nm.

2.3.2 Testing the permeation ability of phosphatidylcholine liposome in ocular tissues

In this section the permeation ability of two formulations for ocular delivery of latanoprost (LAT) is presented. Marco Brugnera from the faculty of Pharmacy at the Universidad Complutense de Madrid synthesized and characterized phosphatidylcholine liposomes for LAT delivery in ocular tissue. Moreover, in collaboration with Prof. Silvia Pescina from the ADDRess lab at the University of Parma, he carried out the characterization of the carrier in *ex vivo* animal models.

Latanoprost (LAT) (Fig. 2.18), a small hydrophobic molecule, is an isopropyl ester prodrug similar to prostaglandin F2α. LAT showed a remarkable ability to reduce intraocular pressure (IOP) and received the approval from European Medicines Evaluation Agency and the USFDA as a first-line treatment for ocular hypertension or primary open-angle glaucoma. [103]

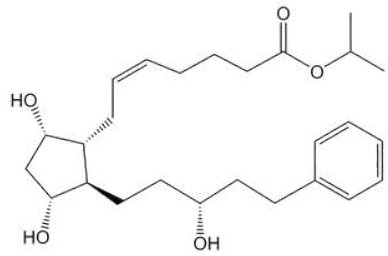

Figure 2.18: Chemical structure of latanoprost

Unfortunately, due to the physiological structure and function of the eye, the delivery of ophthalmic drugs is limited. Indeed, the main challenge for this route of administration is the drug bioavailability, estimated to be only 5%. [104]

Thus, it is pivotal to increase the uptake of LAT close to the target site and its penetration across the ocular surface. [105] To overcome these challenges, LAT was included in phosphatidylcholine

(Fig. 2.19) liposomes. Liposomes are frequently used as carriers for the delivery of lipophilic topical ophthalmic drugs, such as LAT. [106]

To enhance retention time and stability of the formulation, our collaborators employed hyaluronic acid (HA). Indeed, HA is an anionic polymer that exhibits biocompatibility and biodegradability with low toxicity. [107] Moreover, it has the ability to retain water, forming a viscous polymeric chain dispersion with mucoadhesive properties that can enhance the residence time of the drug in ocular tissue. [108, 109]

Furthermore, the chronic applications of preserved topical hypotensive medicines induce a progressive instability and disruption of the preocular tear film, which results in increased tear hypertonicity and desiccation of the ocular surface, inducing the development of dry eye disease (DED). [110] Thus, to increase the protection against DED, osmoprotective agents,specifically betaine (BET) and leucine (LEU) (Fig. 2.19), were incorporated into the aqueous dispersion of the liposomal formulation.

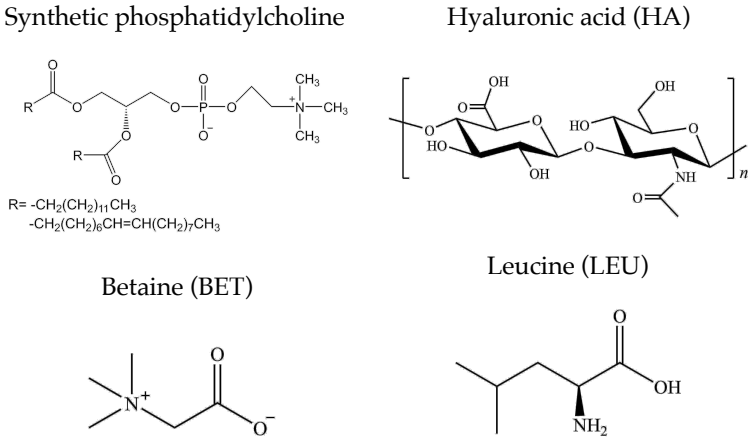

Figure 2.19: Chemical structure of liposomes components.

Evaluation of the effect of HA on the permeation ability *via* 2PM

2PM experiments were carried out to evaluate the effect of HA on the permeation ability of the formulation.

To this aim, two formulations were prepared: one without HA (LAT-LIP) and one with HA at a final concentration of 0.2% w/v (LAT-HA-LIP). For two-photon microscopy studies, both formulations were stained with coumarine6 (COU). COU was dissolved in chloroform and included into the lipid mixture to a final concentration of 0.005‰w/v. The two formulations were characterized by Marco Brugnera in terms of physicochemical properties, stability and retention inside ocular tissues. [111]

Corneal and scleral tissues were treated with either COU-LIP or COU-HA-LIP for a duration of 2 h with a Franz cell (Sec. 2.3.4 for details on the treatment procedure). Images and spectra were acquired by exciting the sample at 900 nm to minimize tissue autofluorescence and, at the same time, maximize the COU signal.

Images acquired at different depths of corneal tissues treated with both formulations and a 3D reconstruction of the samples are reported in Fig. 2.20.

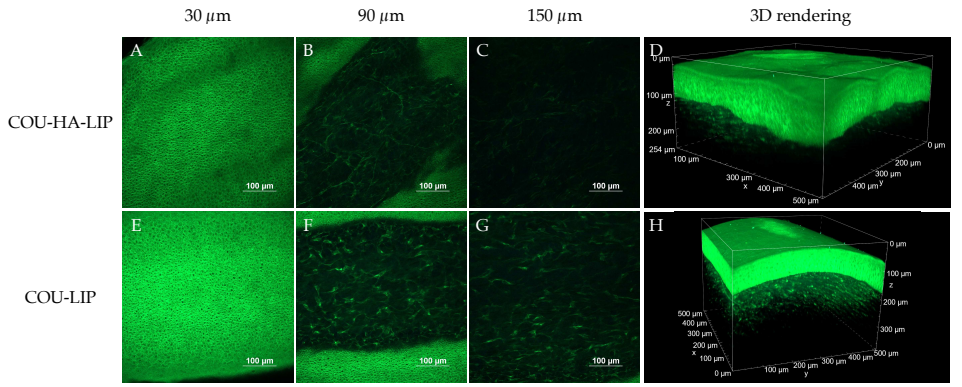

Figure 2.20: Two-photon images taken at different depths of cornea treated with either COU-LIP or COU-HA-LIP ($\lambda_{exc=} = 900\,\text{nm}$).

The intense green fluorescence signal arises from both epithelial cells and stromal region. The emission spectra acquired from the tissues indicated that the green signal was entirely due to COU emission. Moreover, from the images acquired at 150 µm, a first evidence of the different penetration ability of the two formulations can be noticed, since a more intense green signal can be observed for the formulation without HA.

Emission spectra were acquired at different depths in specimens treated with both formulations (Fig 2.21). Moreover, the endothelium (*i.e.* the deepest stratum in cornea see Sec. A.3.1) was analyzed by flipping the sample upside down and collecting the emission spectrum.

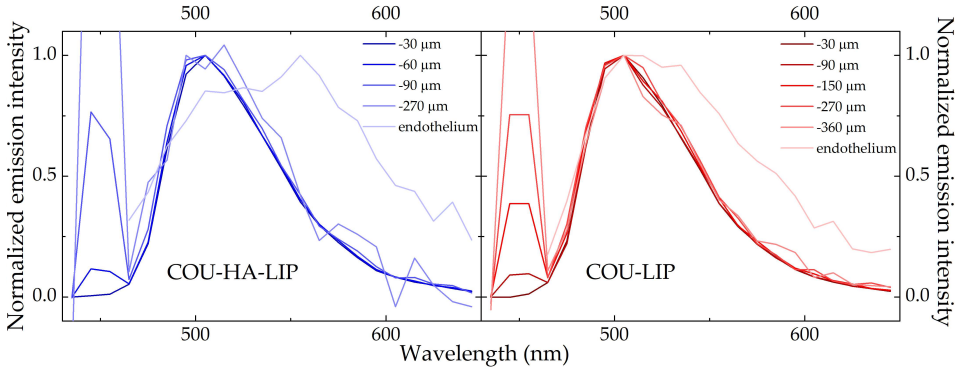

Figure 2.21: Emission spectra acquired at different depth in corneal tissues treated with COU-HA-LIP or COU-LIP ($\lambda_{exc=} = 900$ nm).

Two different signals are present in the spectra acquired from the treated tissue: the SHG signal of stromal collagen at 450 nm and the COU emission with a maximum peak at 500 nm.

The COU signal can be detected up to 270 µm below the surface of the sample treated with the formulation with HA, and up to 360 µm in the sample treated with the formulation without HA. Moreover, the emission spectrum acquired on the endothelium of

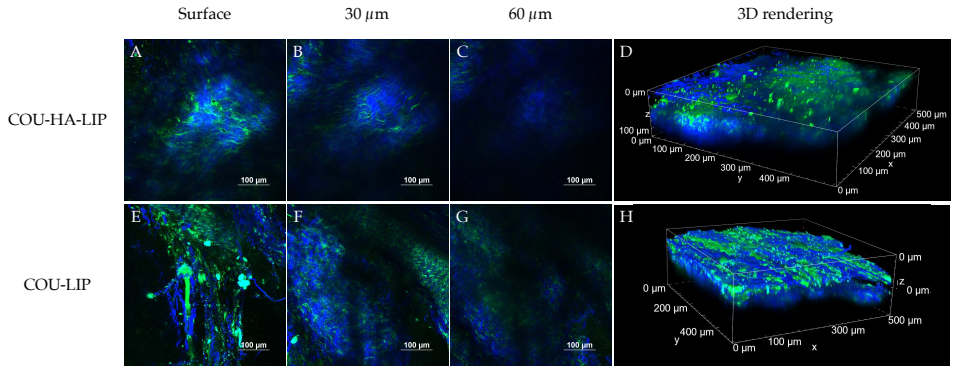

Figure 2.22: Two-photon images taken at different depths of sclera treated with either COU-LIP or COU-HA-LIP ($\lambda_{exc=} = 900\,\text{nm}$).

the sample treated with COU-LIP indicated the presence of the fluorophore in the deepest stratum of cornea. The bandshape is more broadened than in the other spectra probably because of the autofluorescence contribution, that has a similar intensity compared to COU at this depth. On the opposite, in the spectrum acquired on the endothelium of the sample treated with the formulation without HA, the contribution of COU signal cannot be observed.

A similar investigation was conducted also on scleral tissue. Images acquired at different depths of scleral tissues treated with both formulations and a 3D reconstruction of the samples are reported in Fig. 2.22.

Blue and green signals were detected: the blue signal is due to the SHG generated by the collagen fibers that compose the scleral tissue, while the green signal is the COU emission. The analysis of 2D images suggests that the COU is located between the collagen fibers and, as in the corneal tissue, that the formulation with HA permeates less than the one without it.

To confirm what observed in the images, emission spectra at different depths of the samples were acquired (Fig. 2.23). The COU signal was detected up to 60 µm below the surface of the sample

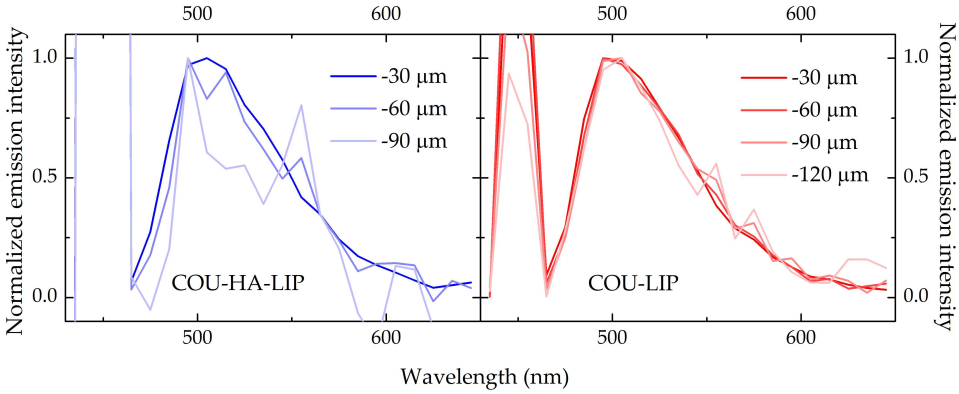

Figure 2.23: Emission spectra acquired at different depth in scleral tissues treated with COU-HA-LIP or COU-LIP ($\lambda_{exc=} = 900\,\text{nm}$).

treated with the formulation with HA, and up to 120 µm on the sample treated with the formulation without HA, indicating that also in scleral tissue COU-LIP permeates deeper.

2.3.3 Conclusions and future perspectives

The case studies presented in 2.3.1 and 2.3.2 showed the importance of acquiring images deep into thick tissues when evaluating the penetration ability of novel formulations. Both works are currently under revision in Journal of Controlled Release.

In Sec. 2.3.1, the evaluation of mucoadhesion and mucopenetration properties of TMC NPs was presented. Notably, the possibility to acquire hyperspectral images deep in the sample with the two-photon microscope, allowed us to follow the permeation of formulations in the tissue and to highlight that the the presence of TMC NPs increased both the adhesion on and the penetration into the nasal tissue of Cy3-siRNA. Moreover, from the 3D reconstructions acquired on the nasal mucosa treated with Cy3-siRNA loaded TMC NPs a possible penetration mechanism was inferred. Indeed, the 3D images suggested that the formulation was capable of permeate through inter-cells channels.

In Sec. 2.3.2, the effect of HA in the permeation ability of the formulation was assessed thanks to the acquisition of both spectra and images at different depths of thick samples with the two-photon microscope.

From images, it was possible to infer the localization of COU inside each sample and to visually assess which formulation had the best permeation ability. The acquisition of emission spectra up to 360 µm in the cornea and up to 120 µm in the sclera allowed us to determine up to which depth the COU emission was detectable in our experimental conditions. The obtained results indicate that the formulation without HA penetrates the most in ocular tissue, probably because HA increases the adhesion property of the formulation preventing an efficient permeation inside the samples.

Two-photon microscopy is the technique of choice for visualizing biological tissues in depth. This is because the near-infrared light used to excite samples in 2PM experiments penetrates biolog-

ical tissues much more effectively than UV-visible radiation, allowing the acquisition of images over 1 mm deep in the samples.

Nonetheless, the penetration can be limited by the intrinsic characteristics of the tissues such as transparency and pigmentation. Indeed, in the studies presented here, the penetration of light, *i.e.* the maximum depth we could image, across sclera, a white, opaque tissue was always less efficient compared to the penetration into the non-colored, transparent cornea.

Furthermore, the choice of the fluorescent probe is of paramount importance for the specific investigation. In this chapter, three different commercial dyes have been tested. Solvatochromic dyes, like Nile Red, offer the opportunity to exploit their sensitivity to the environment to investigate the fate of the carrier in biological tissues, as shown in Sec. 2.2. Cyanines (Cy3) are widely employed for their high extinction coefficient and good fluorescence quantum yield. The choice of Coumarine 6 for labeling liposomes was actually done by the group in Spain, since they had already experience with this dye. Remembering that scattering decreases with increasing wavelengths (both excitation and emission), and that tissues have transparency windows in the infrared spectral region, the use of higher excitation wavelengths combined with more red-emissive fluorescent probes, will further increase the ability to image deep strata also in non-transparent tissues (always considering that the maximum penetration achievable is equal to the working distance of the objective). For this purpose, efficient red/near infrared fluorescent probes for bioimaging have been developed to improve the in-depth imaging of samples. [112, 113]

2.3.4 Materials and Methods

Mucoadhesion study on rabbit nasal mucosa

Handling of nasal mucosa was performed by the group of Prof. Fabio Sonvico. Fresh nasal mucosal tissue was isolated from rabbit heads kindly provided by a local slaughterhouse (Bertoni Carni S.r.l., Busana, Reggio-Emilia, Italy). The heads were stored in ice and used within 4 h from animal death. Nasal mucosa discs (8 mm) were attached on a Petri dish with a double-sided tape (Tesafix® 4934, KaiserKraft, Stuttgart, Germany) and treated with 20 µL of the Cy3-siRNA included in TMC NPs (∼332 ng Cy3-siRNA: ∼6640 ng of TMC) or the free Cy3-siRNA solution. The tissues were imaged immediately after the formulations deposition and after 30 min of washing with ultrapure water.

Nasal mucosal tissue penetration studies

The mucopenetration of Cy3-siRNA loaded TMC NPs (siRNA:TMC ratio of 1:20 w:w) and the free Cy3-siRNA used as control was evaluated by placing 20 µL of each formulation on a different 8 mm diameter disc of rabbit nasal mucosa. The samples were imaged immediately after the deposition of the formulations and then after selected time points.

Liposomes preparation

Liposomes were elaborated according to the lipid film hydration protocol explained by Bangham et al. with some modifications by Marco Brugnera. [114, 115] The lipid bilayer was composed by a borate buffer (0.84% w/v H_3BO_3, 0.14% w/v $Na_2B_4O_7{\cdot}10H_2O$), 1.04% w/v TREH, 0.40% w/v BET and 0.90% w/v LEU, DOPC (0.75% w/v), DMPC (0.25% w/v), CHOL (0.125% w/v) and VE (0.01% w/v). To assess the impact of mucoadhesive HA, two formulations

were prepared: one without HA (LAT-LIP) and one with a final concentration of 0.2% w/v HA (LAT-HA-LIP). For two-photon microscopy studies, COU-loaded liposomes with (COU-HA-LIP) and without (COU-LIP) 0.2% w/v HA were elaborated. COU was dissolved in chloroform and included into the lipid mixture to a final concentration of 0.005‰ w/v.

Ex vivo liposomes study

Handling of porcine tissues was performed by Marco Brugnera and Silvia Pescina. Fresh porcine ocular bulbs (Sus scrofa domestica, female and male animals, age 10−11 months, weight 145−190 kg) were taken from a local slaughterhouse (Macello Annoni S.p.a., Busseto, Italy), transferred under refrigeration in physiological solution (0.9% w/v NaCl) and manipulated within 4 h from the enucleation. Muscular and connective adnexa around the ocular bulbs were meticulously removed with scissors. Only eyes with macroscopically intact corneas were used. Corneal and scleral tissues were mounted on a Franz cell with a 0.6 cm^2 permeation area. The donor chamber was filled with 400 µL of the COU-HA-LIP or COU-LIP formulations, whereas N-2-hydroxyethylpiperazine-N'-2-ethanesulphonic acid (HEPES) 65 mM at pH 7.4 was gently pipetted in the receptor chamber and kept under magnetic stirring. After 2 h, COU-LIP or COU-HA-LIP was removed, the tissues were washed, dismantled from the Franz-type cell, punched to obtain 9 mm diameter discs, placed in a dedicated plexiglass holder and imaged. Saline solution was used to dip the objective and avoid dehydration.

Chapter 3

Micro-Raman spectroscopy for microplastics identification

3.1 Introduction

During the XX century, plastic production reached more than 320 million tons per year. [116] Atmospheric agents such as abrasion, waves and UV radiation in combination with bacteria degrade plastic fragments in micro- and nanosized particles. [117, 118]

These particles are pervasive across various ecosystems and were detected in marine, [119] freshwater, [120] terrestrial, [121] and airborne environments [122], generating global concern.

As a consequence, microplastics (MPs) have also been detected in both animal and human samples. [123, 124] MPs accumulation in tissues may lead to various adverse effects, such as immune responses, [125] physical injury, [126] inhibition of growth and development, [127] metabolic disorders [128] and genotoxicity. [129]

In the last years, many studies demonstrated that MPs can be found in the human placentas. [130, 131, 132, 133, 134, 135, 136] The placenta finely regulates the equilibrium between fetal and mater-

nal compartments, acting as a crucial interface via distinct complex mechanisms. [137] The presence of MPs in this organ and in this stage of life may lead to improper differentiation between nonself and self-compartments. [138] Moreover, the presence of MPs was demonstrated also in human amniotic liquid [139] and carbon black particles were found in maternal blood, cordon blood and fetal organs, [140] proving that particles can cross the placenta and reach the fetus.

The study presented in this chapter aims to assess whether microplastics are present in the placentas and fetuses at an early stage of pregnancy. Thanks to the collaboration with the Department of Veterinary Science of the University of Parma it was possible to analyze stray cats that were used as a model of a real *in vivo* exposure. Our collaborators used a standardized protocol for the digestion of biological matter, as well as a plastic-free approach for sample collection and manipulation. The sample collected were analyzed using micro-Raman spectroscopy immediately after the digestion to avoid any contamination. Raman microscopy is one of the most widely used techniques for detecting and identifying MPs across a broad range of samples, from environmental [141, 142] to biological [143, 144], due to its ability to acquire spectra unique to the compounds being analyzed.

3.2 Results and discussion

Eight animals before the thirtieth day of pregnancy, numbered from 1 to 8 based on the chronological order of the analysis, were used in this study. For each animal, a placenta and a fetus were exported, digested, and filtered following the procedure described in Sec. 3.4. Two portions ($700\times500\,\mu m$) of each filter, selected with a $10\times$ objective lens, were then analyzed with a $50\times$ objective lens to better detect and characterize the particles present. Only colored particles were considered in our study since they present a better contrast compared to the filter. Moreover, only particles between 1 and 10 µm were selected since they are more likely to be transported by the bloodstream and pass the placenta barrier. Four of eight animals showed contamination of colored particles of size $\leq$10 µm, with a total of 19 MPs detected in both fetal and placental samples. Specifically, fetuses from cats 4 and 7 were contaminated, as were the placentas from cats 5, 6, and 7.

Table 3.1 summarizes the main results, reporting the particle number, the cat and the organ (F= fetus, P= placenta) where they were detected, their size, and, where possible, the identified pigment and the polymer matrix.

Particle 11 is the only particle for which, despite its orange color, the pigment could not be identified. However, the Raman spectrum (spectral region $850\,cm^{-1}-450\,cm^{-1}$) of this particle, that is shown in Fig. 3.1 together with the microscope image, is very interesting: the Raman peaks are indeed attributable to a polyethylene (PE) polymeric matrix. Specifically, $C-C$ stretchings are responsible for 1061 and $1130\,cm^{-1}$ peaks, $1297\,cm^{-1}$ is the CH_2 twisting peak, and the peaks at 1420, 1440, and $1464\,cm^{-1}$ are associated to the CH_2 bending. [145] Similar Raman peaks are identified also in particles 2, 3, 6, 8, 9, 10.

Fig. 3.2 shows the microscope images and Raman spectra of the other colored particles found in the placentas and fetuses. The spec-

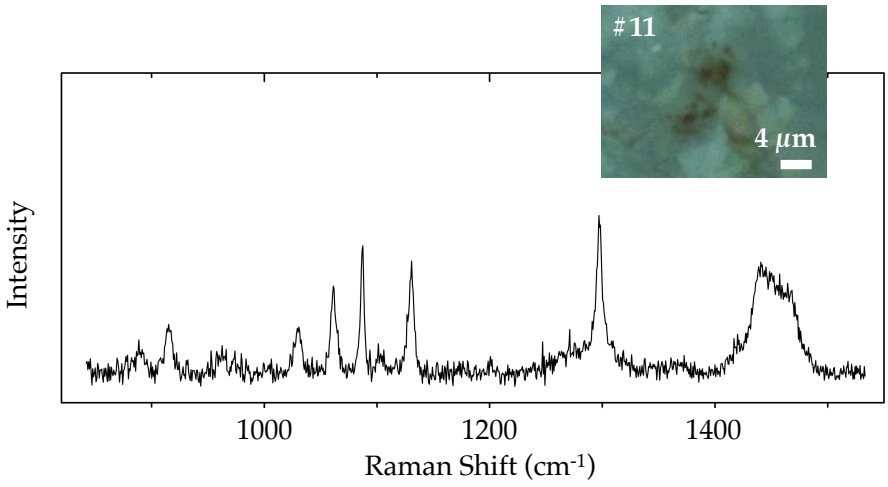

Figure 3.1: Microscope image and Raman spectrum of Particle 11.

tra show only the spectral region where bands of dyes and pigments are detected (for particles 2, 3, 6, 8, 9, and 10, the peaks attributed to PE are reported in Fig. 3.3). Seven different types of dyes and additives were recognized: Anatase, Mars Red, Raw Sienna, Goethite, Haematite, Burnt Umber and Alcian Blue.

According to their Raman spectra, the analyzed microparticles could be divided into seven groups based on their additives:

1. **Particles 1**, **7**, and **10** (Fig. 3.2.A): The Raman spectra of these particles are composite spectra resulting from the superposition of different components. The Raman bands match the bands of Anatase (145, 198, 401, 640 cm^{-1}) and Mars Red (224, 291, 407, 496, 611 cm^{-1}). Anatase and rutile are two different forms of titanium dioxide and are known for their use in plastics as inexpensive, efficient, chemically and biologically inert additives. [146] Mars pigments, which were synthetically developed in the eighteenth century, are part of the iron oxide group of additives. They cover a large range of colors ranging

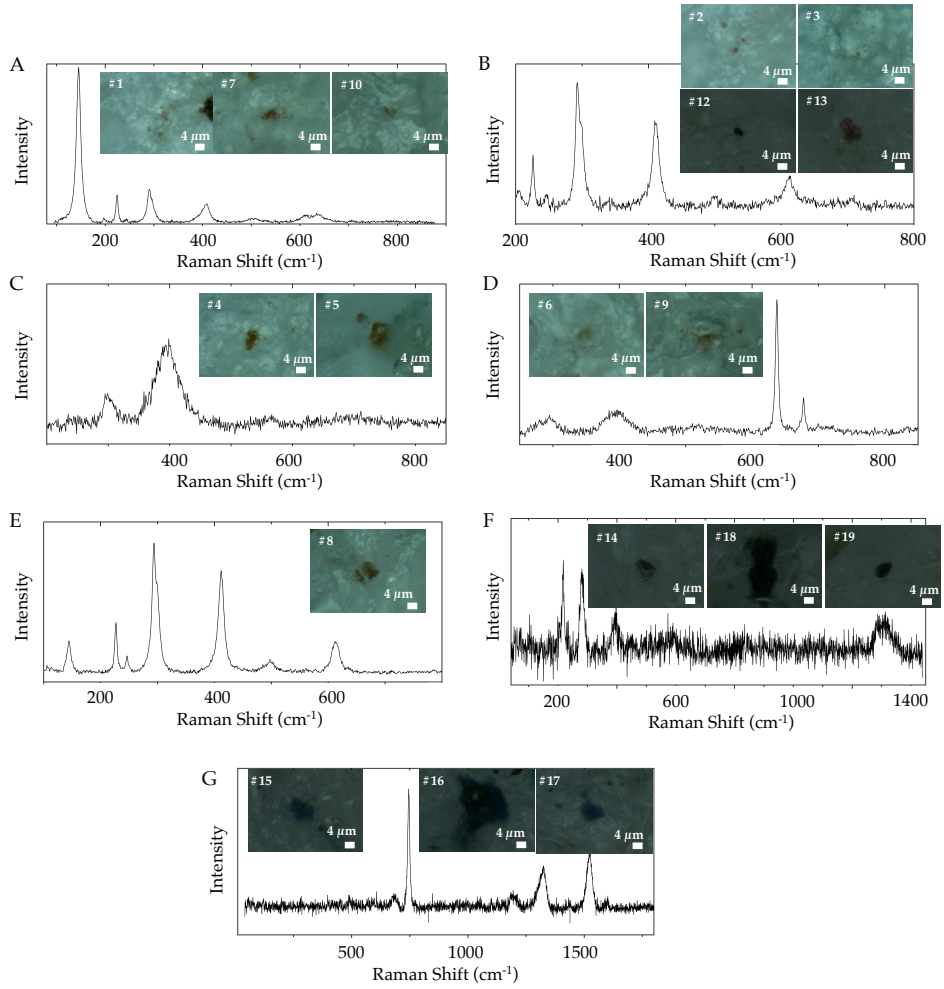

Figure 3.2: Microscope images and Raman spectra of colored particles smaller than 10 µm detected in feline placentas and fetuses.

from yellow to red, purple and black. [147]

2. **Particles 2**, **3**, **12**, and **13** (Fig. 3.2.B): The Raman spectra of these particles share the main peaks at 226, 293, 409, 499, and 611 cm^{-1} with one pigment among the iron oxides, Mars Red,

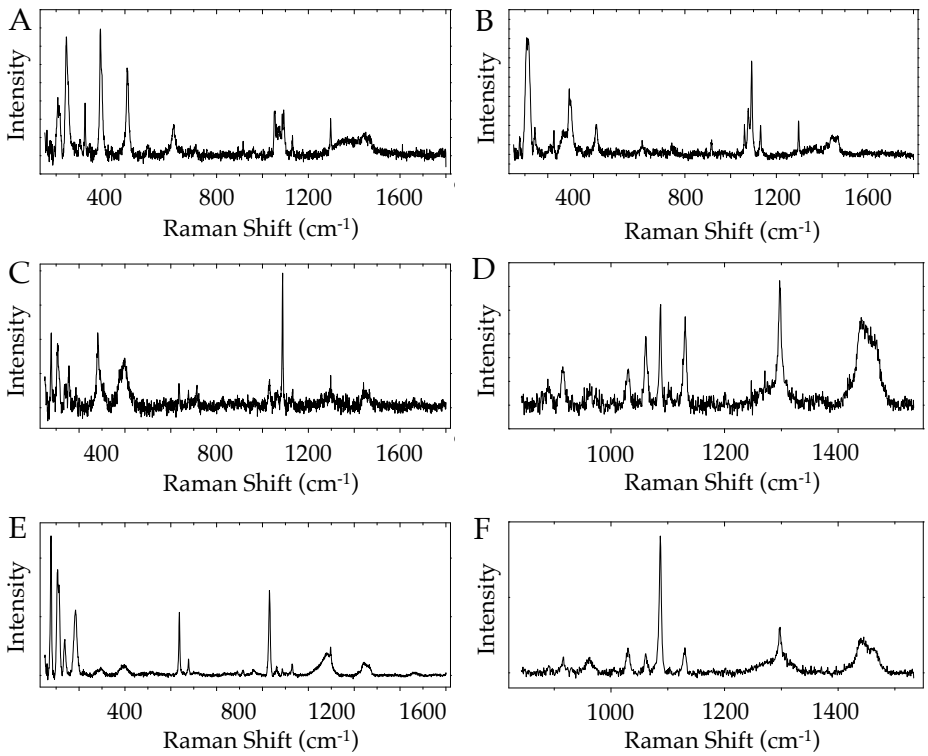

Figure 3.3: Raman spectra acquired on particle 2 (panel A), particle 3 (panel B), particle 6 (panel C), particle 8 (panel D), particle 9 (panel E), and particle 10 (panel F) in the spectral region where the polymer matrix bands are detected.

as determined by KnowItAll software.

3. **Particles 4** and **5** (Fig. 3.2.C): The peaks at 302, 396, 559, and 708 cm^{-1} are superimposed onto those of the pigment known as the Raw Sienna. This additive contains manganese oxides and is also rich in iron hydroxides, which are responsible for the brownish-yellow shades. [147]

4. **Particles 6** and **9** (Fig. 3.2.D): The Raman spectra of these particles are composite spectra resulting in the sum of the polymer matrix and the pigment bands. In particular, the peaks at 290 and 392 cm^{-1} are assigned to the pigment iron hydroxide oxide yellow (Goethite). [148]

5. **Particle 8** (Fig. 3.2.E): The peaks at 226, 247, 294, 412, 497, and 612 cm^{-1} are attributed to a pigment classified as an iron oxide, Haematite ($\alpha - Fe_2O_3$). [148]

6. **Particles 14**, **18**, and **19** (Fig. 3.2.F): Raman peaks at 216, 276, 387, and 590 cm^{-1} are ascribed to a common iron oxide pigment called Burnt Umber. Generally, umber contains manganese oxide along with iron oxides in a fraction that makes it different from ochres and siennas. [147]

7. **Particles 15**, **16**, and **17** (Fig. 3.2.G): The bands at 683, 745, 1198, 1328, 1432, 1525, and 1601 cm^{-1} are related to Raman signals of a phthalocyanine blue pigment, Alcian Blue, according to KnowItAll software.

Under the same experimental conditions, blank filters did not show the presence of colored particles with a Raman spectrum compatible with the presence of plastic matrices or pigments.

Out of the 16 investigated samples (8 placentas and 8 fetuses), 5 were found contaminated by colored MPs. 6 colored MPs were found in fetal samples while 13 were found in placentas.

It is worth noting that the methodology applied underestimates the real number of MPs, possibly leading to false negatives. Only colored particles were considered in our study since they present a better contrast on the white filter and can be distinguished from the inorganic salts derived from the digestion process (KOH can react with atmospheric CO_2 generating $KHCO_3$ and K_2CO_3). Moreover, only particles between 1 and 10 µm were selected since they

are more likely to be transported by the bloodstream. Nonetheless, the aim of this work was to determine whether MPs can be found in placentas and fetuses in the early stage of pregnancy and not to quantify them. Therefore, even if underestimated, MPs were found in 2 fetuses out of 8, hinting that this contaminant can overcome the placental barrier and reach the fetus even in the early stages of pregnancy. Through the comparison with spectra reported in the literature (the SLOPP library and peer-reviewed publications) and using the KnowItAll software, it was possible to identify the dye in 18 particles and the backbone of the polymeric matrix in 7 particles (out of 19). Since Raman response is usually more intense for dyes then polymer matrices, it is common [133, 144, 149] to detect the pigment but not the polymer. For the same reason, it is not surprising that the polymer matrix was always identified as PE. PE is structurally composed by the repetition of the CH_2 motif, a building block present in the backbone of several polymers such as polypropylene, nylon 6, polyethylene terephthalate, etc. Since the backbone is the most repeated feature in a polymer, it is reasonable that the peaks associated with the CH_2 motif arise the strongest signals of the polymeric matrix, leading to the identification of those signals as PE.

Table 3.1: List of the main features of the detected color particles. First column: particle number; second column: information regarding where they were found (cat number; F: fetus and P: placenta); third column: dimension of the particle; fourth column: identified pigments (n.d.= not determined); fifth column: polymer matrix (n.d.=not determined).

Particle	**Cat**	**Size**	**Pigment**	**Polymer matrix**
1	4 - F	∼2 µm	Mars Red+Anatase	n.d.
2	4 - F	∼2 µm	Mars Red	PE
3	4 - F	∼2 µm	Mars Red	PE
4	5 - P	∼5 µm	Raw Sienna	n.d.
5	5 - P	∼5 µm	Raw Sienna	n.d.
6	5 - P	∼3 µm	Goethite	PE
7	5 - P	∼2 µm	Mars Red+Anatase	n.d.
8	5 - P	∼10 µm	Haematite	PE
9	5 - P	∼5 µm	Goethite	PE
10	5 - P	∼2 µm	Mars Red+Anatase	PE
11	5 - P	∼5 µm	n.d.	PE
12	6 - P	∼5 µm	Mars Red	n.d.
13	6 - P	∼10 µm	Mars Red	n.d.
14	6 - P	∼5 µm	Burnt Umber	n.d.
15	7 - F	∼5 µm	Alcian Blue	n.d.
16	7 - F	∼10 µm	Alcian Blue	n.d.
17	7 - F	∼5 µm	Alcian Blue	n.d.
18	7 - P	∼10 µm	Burnt Umber	n.d.
19	7 - P	∼5 µm	Burnt Umber	n.d.

3.3 Conclusions and future perspectives

The high production and consumption of plastics is a serious and practical issue. MPs are pervasive across global ecosystems, are capable of contaminating water and animals and can be detected in the internal organs of the human body.

In the study presented in this chapter, we demonstrated for the first time that MPs can accumulate in feline placentas at the early stage of pregnancy, and, even more interestingly, also in fetuses. The dimensions of all the MPs detected were $\leq 10\,\mu m$, which is compatible with transportation via the bloodstream.

The use of micro-Raman spectroscopy was pivotal in this study. Indeed, thanks to the images it was possible to visualize and detect the colored particles present on the filter but only with the spectra acquisition, it was possible to identify the dye and/or the polymer matrix. This study is currently under revision in PlosOne.

This work represented a first approach for the research group to the investigation of microplastics. While the results were promising, we encountered several challenges during the experimental analysis. First, we found that the filters were not optimal for this application due to the presence of fibers, which made particle identification very challenging. Additionally, the size of the filters was too large to conduct the analysis within a reasonable time, forcing us to image only a small portion of them. In future analyses, we plan to use silicon filters with defined pore sizes and smaller dimensions. Furthermore, we will explore the use of software tools to facilitate particle detection.

3.4 Materials and Methods

Animals

For this study, 8 pregnant queens (before day 30 of pregnancy) were brought to the Obstetrics Unit at the Veterinary Teaching Hospital (OVUD) at the Department of Veterinary Medicine of the University of Parma. The total number of placentas and fetuses was 16 (8 placentas and 8 fetuses). All queens were stray cats who came to the hospital for the population control program of the Emilia–Romagna Region. All cats were clinically healthy on physical examination, and the gestational ages were estimated to be between 15 and 30 days. The Ethical Commission of the University of Parma, approved the present study on February 2022 (protocol number 3/CESA/2022). The surgical procedure carried out by the group at the Department of Veterinary Science of the University of Parma was performed without the use of plastic.

Sample digestion

The digestion procedure was conducted by the group at the Department of Veterinary Science of the University of Parma following a plastic free method previously published, with some modifications. [150] Briefly, both types of samples were incubated in a glass container with a 10% (w/v) KOH water solution. The ratio between the grams of sample and the volume of KOH was 1:8 (w/v). The water used for the preparation of the KOH solution had been previously filtered three times through a 1.6 µm pore-size filter membrane (Whatman GF/A) under vacuum. The samples were then stored at room temperature for 3 days. To avoid contamination of the samples, all the protective devices (laboratory coats, gloves, glasses, masks, etc.) employed were rigorously plastic free. Filtered water (1.6 µm) was used to prepare the 70% ethanol (v/v) solutions employed for cleaning bench working surfaces and for rinsing

(three times) all the glassware and instruments (scalpels, scissors, and tweezers) used for the preparation of the samples. After the end of the incubation, the digested samples were filtered under vacuum through the same type of 1.6 µm pore-size filter used for the preparation of the water. The filters were dried at room temperature and then stored in a glass Petri dish until further processing. Three samples of the same KOH solution used for the digestion of the biological samples were subjected to the same procedure, and the resulting filters represented the blanks used to assess the eventual environmental contamination by plastic particles. [151]

Microplastic identification by micro-Raman spectroscopy

Raman spectra were acquired with a Horiba LabRAM HR Evolution Raman microspectrometer equipped with a liquid nitrogen-cooled CCD and a 600 mm grating blazed at 750 nm. Daily calibration was performed with a silicon slice using the 520.7 cm^{-1} band. The filters containing the digested were first imaged with a $\times 10$ objective to locate all the particles. Two distinct sections of the filter surface were selected for examination to analyze several filters in a reasonable amount of time. A $50\times$ magnification objective was then used to focus a 785 nm laser diode, with a spot radius of 2 mm, on the sample and collect higher-quality Raman spectra. The acquisition parameters were modified to ensure the best signal-to-noise ratio always starting from the minimal laser power (below 0.1 mW) to prevent thermal degradation of the materials. Only colored particles smaller than 10 µm were considered for the analysis. A blank filter was prepared and analyzed under the same operating conditions as the specimen filters to track potential contamination during sample preparation. Raman spectra were collected for each particle, and identification of the pigment and/or of the polymer matrix was performed via comparison with spectra reported in the literature (the SLOPP library and peer-reviewed publications) and with

KnowItAll software. Spectra were subjected to baseline correction before the fitting procedure to ensure data comparison between the acquired Raman spectra and those reported in the literature.

Chapter 4

From basic research to applied research in collaboration with the non-academic sector: two case studies

4.1 Introduction

During my PhD, I had the opportunity to collaborate with various non-academic partners. In this chapter, I present the work (Sec. 4.2) developed in collaboration with Elvesys (now the Microfluidic Innovation Center (MIC)), a French SME and partner of the Micro4Nano European project, with renowned expertise in flow control and a mission focused on accelerating European research projects to enhance the impact of European scientific achievements. The work presented here represents a preliminary step towards combining microfluidics with imaging, a cutting-edge research activity that could eliminate the use of animal tissue in preliminary drug formulation tests, replacing it with 'organ-on-a-chip' models.

The second work was carried out in the framework of a collaboration with an international pharmaceutical company, with a strong focus on research and development in the field of respiratory diseases (for confidentiality reasons, the name of the company will not be mentioned in this thesis). The company was interested in testing the potentialities of 2PM for their needs, and conducted some experiments on pulmonary tissues exposed to formulations labeled with a fluorescent probe (Sec. 4.3).

4.2 Combining microfluidics with bioimaging: cells culture in microfluidics chips

In this section the application of microfluidics to cells culture is exploited. The term "microfluidics" indicates the science and engineering that deal with small volumes of fluids (from 10^{-9}L to 10^{-18}L) confined into micro-scale channels. [152]

Microfluidics attracted the attention of several researchers, from life science to engineering, thanks to the advantages that the handling of such small volumes of fluid provides (*e.g.* low reagent consumption). The main advantage of microfluidics is related to the controlled flow that is generated in micro-scale channels. A flow can be described as laminar or turbulent, depending on its Reynolds number (Re) value: when Re $\sim$ 2000 the flow is laminar, when Re $>$ 2000 the flow is turbulent. The Re is defined as:

$$Re = \rho v d / \mu \tag{4.1}$$

where ρ is the fluid density (g/cm^3), v is the fluid velocity (cm/s), d is the channel hydraulic diameter (cm) and μ is the fluid viscosity ($g/(cm \cdot s)$). The difference between laminar or turbulent flow is depicted in Fig. 4.1. In a laminar regime, the flow is organized, predictable and thus, controllable; while, in a turbulent regime, particles move randomly. The micro-scale dimensions of channels used in microfluidics result in low values of Re and thus, in a flow regime that is always laminar. [153, 154] Hence, the use of microfluidics allows to precisely control the flow, use low amount of reagents and run parallel experiments. Moreover, the set-up dimensions are compatible with biological systems (*e.g.* cells) making these devices a valuable tool for life science investigations. [155] Indeed, microfluidics systems enabled the culture of cells in a highly controlled environments and in more physiological-like conditions. [156] These advantages led to the development of the so called "organ-on-a-

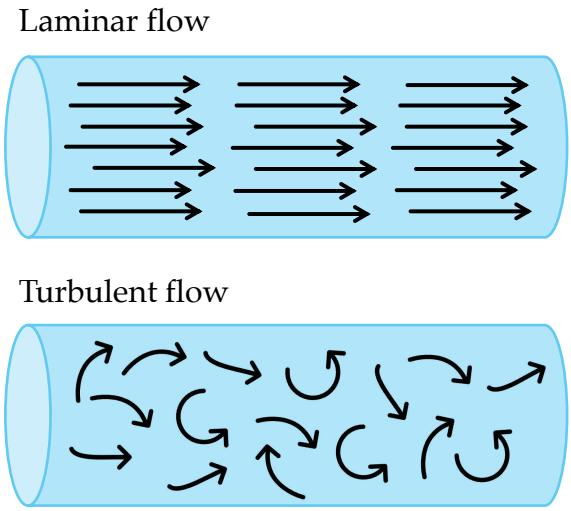

Figure 4.1: Laminar and turbulent flow regimes

chip", *i.e.* cultures of cells in 3D models that mimic the structure and physiology of tissues. [157, 158, 159]

In this section, two microfluidic experiments are presented: the culture of cells for 24 h on a microfluidic chip and the introduction of a recirculation system in the same circuit. These basic analyses were performed at Elvesys (now the Microfluidic Innovation Center) in Paris, with the purpose to acquire the expertise necessary to conduct permeation tests on cultured 3D models instead of animal ones.

Independently from the complexity of the experiment, three set-up components are fundamental to achieve a precise control over the flow during the experiments: the Elveflow software, the pressure controller and the flow sensor.

The Elveflow software is connected to the pressure controller and is the device through which the operator can control the experiment. From the software interface, the flow rate can be selected as

well as the flow profile (steady, pulsatile etc.) and the reservoir to which apply the pressure.

The pressure controller is connected to the source of pressure (in our experiments, compressed air), to the Elveflow software, to the flow sensor and to the circuit reservoirs. This device applies the proper pressure to the selected reservoir to make the fluid flow.

The flow sensor is placed inside the circuit and it is connected to the pressure controller to form a feedback loop. Indeed, this device measures the actual flow rate in the circuit and transmits the information to the controller that adjust the pressure applied to keep the flow as desired.

4.2.1 Experiment 1: 24 h cells culture

For culturing cells on a microfluidics chip, the set-up shown in-Fig. 4.2 was employed. The circuit was composed by two reservoirs and a chip: the culture medium flowed from one reservoir to the other, passing through a seeded chip.

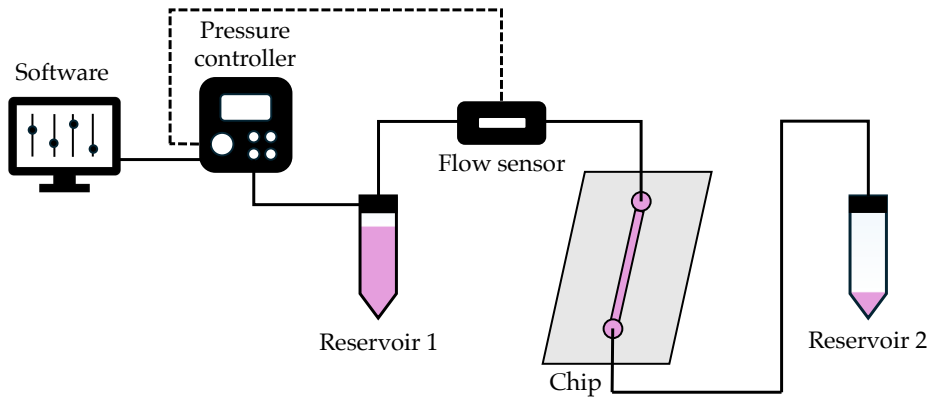

Figure 4.2: Schematic view of the set-up used for culture cells for 24 h.

Before assembling the circuit, the following preliminary proce-

dures were executed:

1. The chip was seeded with U-251MG cells (human glioblastoma astrocytoma transfected with Green Fluorescent Protein (GFP)) and left in the incubator overnight

2. All the tubings and connectors were placed in the autoclave

When all the components were sterilized, the circuit was assembled and rinsed with ethanol, water and culture medium. As last step, the seeded chip was connected with the circuit. We set a constant flow rate of 10 µL/min for 24 h and all the non-electric part of the circuit were placed in the incubator. After 24 h the chip was disconnected from the circuit, the reservoirs were drained and the circuit was rinsed with water and, then, with ethanol.

To monitor the cells viability after the perfusion, cells were imaged with an Axio Observer inverted microscope (Zeiss). For the imaging, the cells were stained with DAPI to visualize cells nuclei and Propidium Iodide (PI), a stainer that cannot permeate the membrane of healthy cells. [160]

Fig. 4.3 shows that only few cells were stained by PI meaning that the majority of cells was still healthy after the 24 h perfusion.

4.2.2 Experiment 2: medium recirculation

In order to obtain organ-on-a-chip, long lasting experiments are needed. Medium recirculation is a valuable option to conduct long lasting experiments without a high consumption of reagents.

To this aim, four check valves were introduced in the perfusion set-up to achieve medium recirculation while keeping a unidirectional flow inside the chip. A check valve is a conical device that allows fluid to flow in only one direction (from the wider end to the narrower end) while preventing backflow. The valve has a movable membrane that displays based on the pressure difference

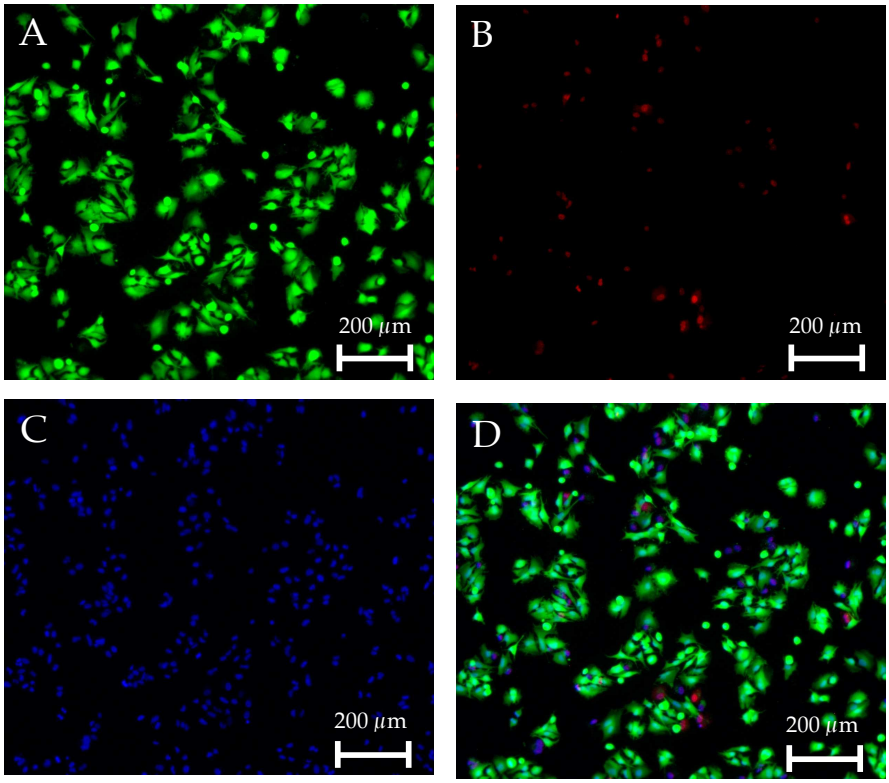

Figure 4.3: Images acquired on seeded cells after 24 h of perfusion. Panel A: GFP, $\lambda_{exc} = 498\,\text{nm}$, $\lambda_{em}^{max} = 517\,\text{nm}$. Panel B: Propidium Iodine, $\lambda_{exc} = 535\,\text{nm}$, $\lambda_{em}^{max} = 617\,\text{nm}$. Panel C: DAPI, $\lambda_{exc} = 358\,\text{nm}$, $\lambda_{em}^{max} = 461\,\text{nm}$. Panel D: merged image.

on the two sides of it, allowing or blocking the flow depending on the direction. The four check valves system is designed as a squared device with one check valve placed on each side and one T-junction placed on each edge to split the incoming flow (Fig. 4.4).

If the check valves are placed correctly, one corner (corner 1 in Fig. 4.4) of the square should only allow the flow to exit from the four check valves system and that corner should be the one

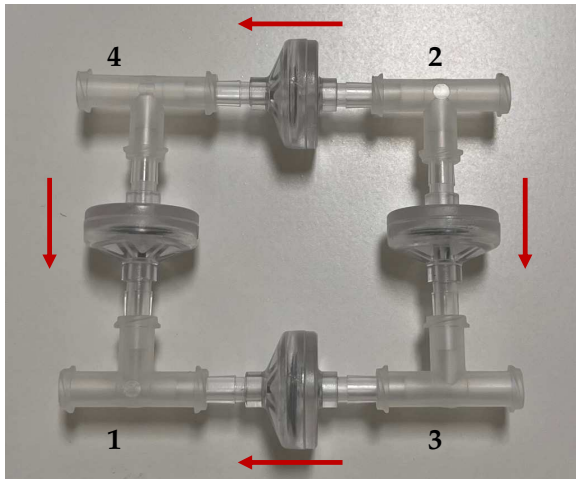

Figure 4.4: Four check valve system. The red arrows indicate the direction in which the fluid can flow.

connected to the chip inlet, while the opposite corner (corner 2 in Fig. 4.4) should only allow the flow to enter the four check valves system and that corner should be connected to the chip outlet to be sure to obtain always a uni-directional flow, the other two corners (corners 3 and 4 in Fig. 4.4) should be connected to the two reservoirs.

Thanks to the four check valves system, two different paths are created depending on which reservoir the pressure is applied to (Fig. 4.5).

Before starting the perfusion, the same steps described in the previous section were carried out:

1. The chip was seeded with U-251MG cells (human glioblastoma astrocytoma transfected with GFP) and left in the incubator overnight

2. All the tubings, connectors and valves were placed in the autoclave

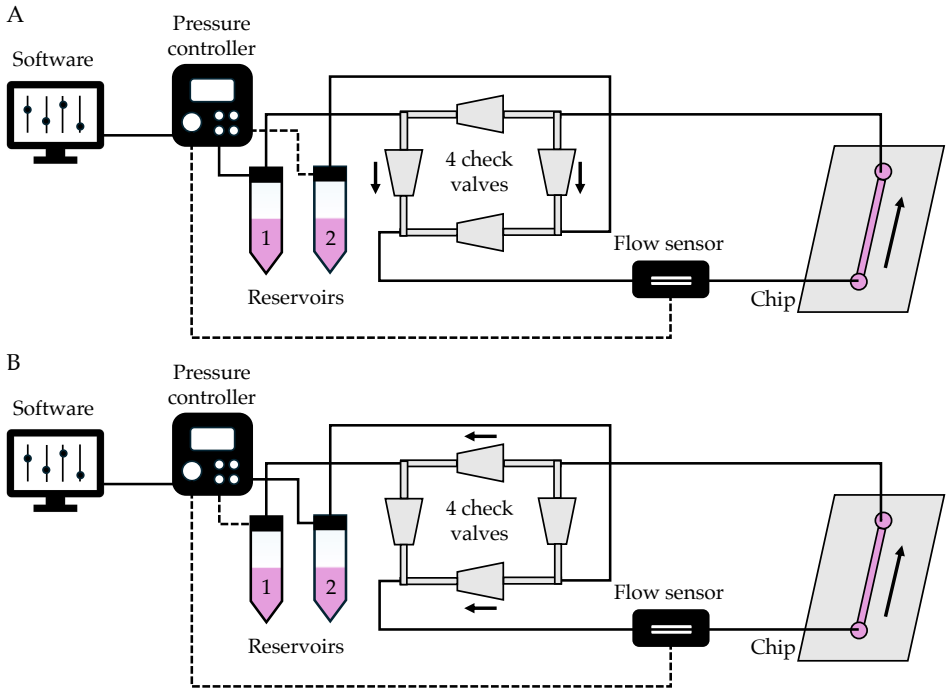

Figure 4.5: Schematic view of the two paths generated thanks to the 4 check valves system. Panel A: path generated when the reservoir 1 is pressurized. Panel B: path generated when the reservoir 2 is pressurized.

3. The circuit was assembled and rinsed with ethanol, water and cells culture medium

4. The chip was connected to the circuit

To obtain medium recirculation with the four check valves, both reservoirs needed to be pressurized alternately. Thus, we created a sequence on Elveflow software that automatically pressurized one reservoir for 6 h keeping a constant flow rate of 10 µL/min and then pressurized the other one in the same way for other 6 h. The experiment lasted a total of 22 h. After 22 h the chip was disconnected

from the circuit, the reservoirs were drained and the circuit was rinsed with water and, then, with ethanol.

In Fig. 4.6 are reported the profile of the pressure applied to each reservoir and the profile of the total flow rate that were recorded by the Elveflow software.

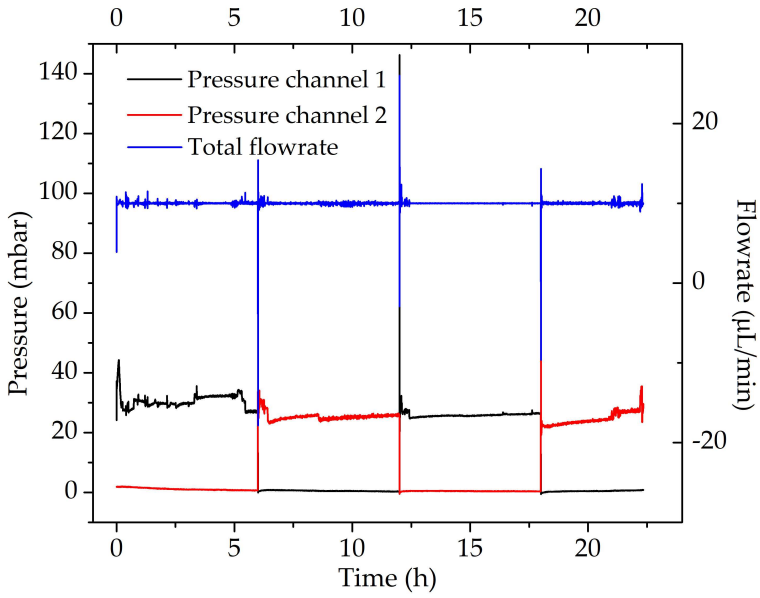

Figure 4.6: Graphs of recirculation pressure profiles (black and red lines) and total flow rate (blue line).

The total flow rate remained constant during the whole experiment (with some fluctuations only at the moment of the pressure switch), while the pressure applied to each reservoir is perfectly alternated.

Once the chip was disconnected, the cells were stained with PI to evaluate their viability and imaged with an Axio Observer inverted microscope (Zeiss): Fig. 4.7 shows that only few cells were stained by PI meaning that the majority of cells was still healthy after the 22 h perfusion.

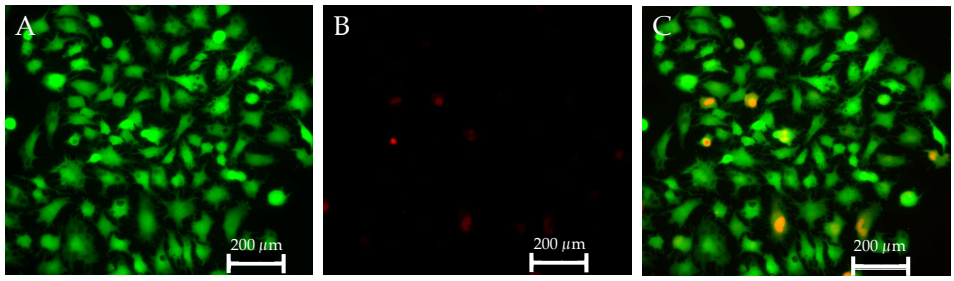

Figure 4.7: Images acquired on seeded cells after 24 h of perfusion. Panel A: GFP, $\lambda_{exc} = 498\,\text{nm}$, $\lambda_{em}^{max} = 517\,\text{nm}$. Panel B: Propidium Iodine, $\lambda_{exc} = 535\,\text{nm}$, $\lambda_{em}^{max} = 617\,\text{nm}$. Panel C: merged image.

The set-up and procedure used in this section were published as a non-peer-reviewed application note on the MIC website. [161]

4.3 Evaluating the potentialities of 2PM for industrial research applications

This section presents the collaboration with an international pharmaceutical company that involved the use of 2PM to investigate a novel pharmaceutical formulation for drug delivery in rat pulmonary tissue. The formulation was constituted by poly(lactic-co-glycolic) acid (PLGA) particles - the carrier - and by a patented small molecule (SM) - the active pharmaceutical ingredient (API). The aim of the work was to evaluate the distribution of the carrier and of the API in the pulmonary tissue at different times after administration.

In order to visualize the formulation with the 2PM, the SM was labeled with BODIPY 650/665 and 10% of PLGA was labeled with Rhodamine B. Although labeling the SM with BODIPY could alter its physical properties, such as for example the diffusion coefficient of the SM, the analyses presented in this chapter serve as a preliminary test to evaluate the potential of 2PM for this type of investigation, rather than a reliable assessment of the SM location within the tissue.

4.3.1 Preliminary characterization

A preliminary analysis was carried out on non-treated lung tissue with 2PM to visualize its physiological structures and the respective autofluorescence spectra (Fig. 4.8).

Two main signals are detected from pulmonary tissue: a green-yellowish autofluorescence and SHG. Although the images show very different structures, the spectra reported in Fig. 4.8.D show that the autofluorescence band is the same for all the images while the SHG signal differs only for its intensity.

The comparison between the images acquired with the two-

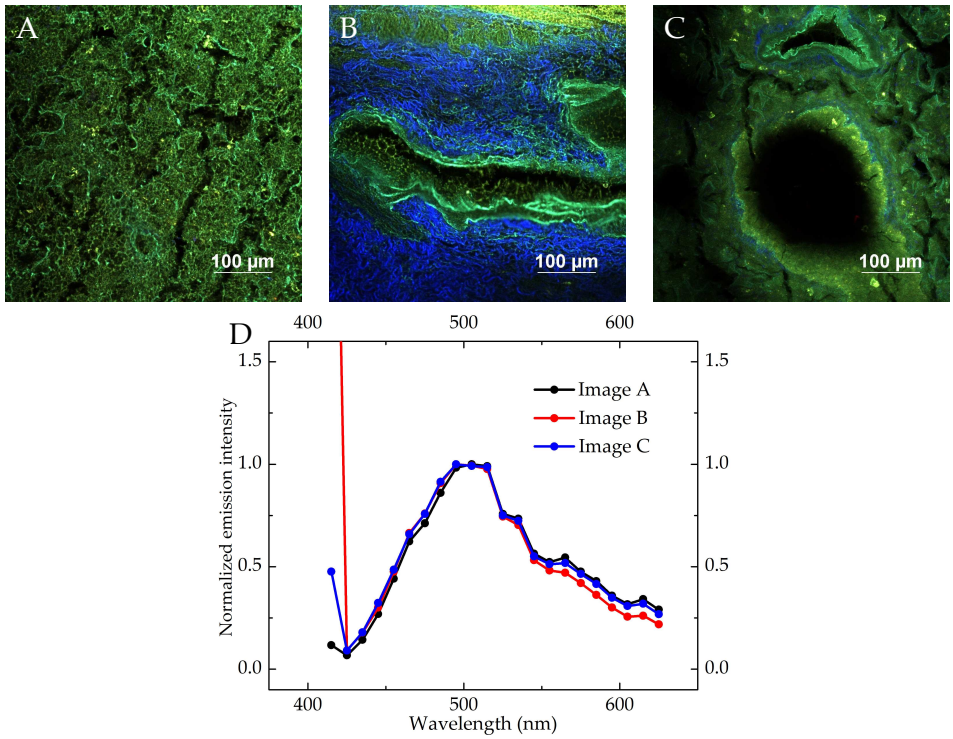

Figure 4.8: Images and spectra acquired on non-treated pulmonary tissue $\lambda_{exc} = 820\,\text{nm}$.

photon microscope and similar images reported in literature, allowed us to identify the structure in Fig. 4.8.A as an alveolar structure, [162] and the circular structures in Fig. 4.8.B and C as vessels and airways. [163] The difference in the edges of the circular structures allows us to distinguish between the two. Specifically, airways have thicker edges due to the epithelial lining while the edge of vessels are composed of a thin endothelium. Moreover, around airways, sub-epithelial collagen is usually present, that can be easily detected due to its SHG signal. [164]

Once the non-treated tissue was characterized, we analyzed a solution of the formulation in Pluronic 1% p/v with the two-photon

microscope and the fluorometer (Fig. 4.9).

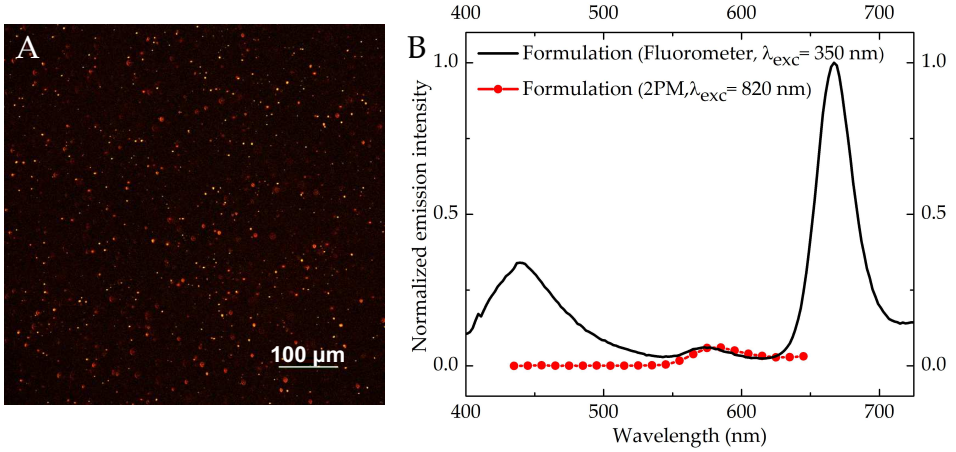

Figure 4.9: Image and spectra acquired on the formulation solution. Panel A: image acquired with the two-photon microscope with $\lambda_{exc} = 820\,\text{nm}$. Panel B: spectra acquired with the fluorometer (blank line, $\lambda_{exc} = 350\,\text{nm}$, a bandpass filter at 395 nm was used) and with the two-photon microscope on the field of view reported in panel A (red line, $\lambda_{exc} = 820\,\text{nm}$).

Fig. 4.9.A reports an image of the formulation: red and yellow fluorescent particles are clearly visible. Looking at Fig. 4.9.B, three distinct signals were detected with the fluorometer: the band around 450 nm was attributed to the SM, the band at ∼580 nm is due to the rhodamine B while, the band at 665 nm is the BODIPY one. Unfortunately, when the same spectrum was acquired with the microscope, only the rhodamine band was fully recorded. Indeed, only a tail of the BODIPY emission falls in the spectral detector range, while the SM signal was not detected. The differences between the emission spectrum collected with the fluorometer (one-photon excitation) and the emission spectrum collected with the microscope (two-photon excitation) can be attributed to the different excitation wavelengths, that selectively excite different flu-

orophores. Specifically, the two-photon excitation at $\lambda_{exc} = 820\,\text{nm}$ cannot excite the SM, that absorbs in the UV. Moreover, energy transfer phenomena could be responsible for excitation-dependent emission.

4.3.2 Pulmonary tissue treated with the fluorescent formulation

As introduced at the beginning of this section, the aim of this work was the evaluation of the spatial and temporal distribution of the formulation different components (nanocarrier and API). Moreover, the formulation was administered at two different concentrations (high and low). Samples were divided into four groups and handled as follows:

- Animals suppressed after 15 min from the administration of the formulation at high concentration (2 mg/mL)
- Animals suppressed after 6 h from the administration of the formulation at high concentration
- Animals suppressed after 15 min from the administration of the formulation at low concentration (0.5 mg/mL)
- Animals suppressed after 6 h from the administration of the formulation at low concentration

The formulation at low concentration was obtained by diluition of the one at high concentration. In all cases the administration was performed *via* aerosol.

In order to highlight different behaviors of the formulation due to differences in treatment, a comparison between images and spectra acquired on the tissue of each group was performed. For the

sake of clarity, here we report only one image of the alveolar structure and one of the airways structure for each group, and the comparison will be presented between two groups at a time. Moreover, the blue signal visible in the images mainly due to SHG generated by collagen was not recorded in the spectra to focus on the dyes emission. A comparison between the blue signals will be discussed in a separate section.

Low concentration: 15 min vs 6 h

The images and spectra acquired on tissues treated with the low concentration formulation for 15 min or 6 h are reported in Fig. 4.10.

The treated tissues present an intense red emission due to the formulation. Notably, when looking at the alveolar structures (Fig. 4.10.A and B) an extended diffusion of the red signal can be observed. On the other hand, in the airways structures (Fig. 4.10.D and E) the red signal is mainly located in the epithelium.

Another interesting feature that can be noticed when comparing Fig. 4.10.A and B is that the formulation signal becomes less diffuse, intense round spots are observable and overall the emission seems less red after 6 h of treatment. Unfortunately, from the images is hard to tell what is causing the change. Thus, the acquisition of emission spectra was necessary to explain this behavior.

The spectra reported in Fig. 4.10.C show three different types of signal: the emission band at $\sim$500 nm due to tissue autofluorescence (see Fig. 4.8), the one at $\sim$600 nm due to rhodamine emission and the partial band at 650 nm due to BODIPY emission (see Fig.4.9). All the spectra reported in this image are normalized, thus no information can be gained regarding the absolute amount of each dye. Nevertheless, it is possible to gain information regarding the relative amount of two dyes. By comparing the spectra acquired on the tissues treated for 15 min or 6 h, it is clear that despite hav-

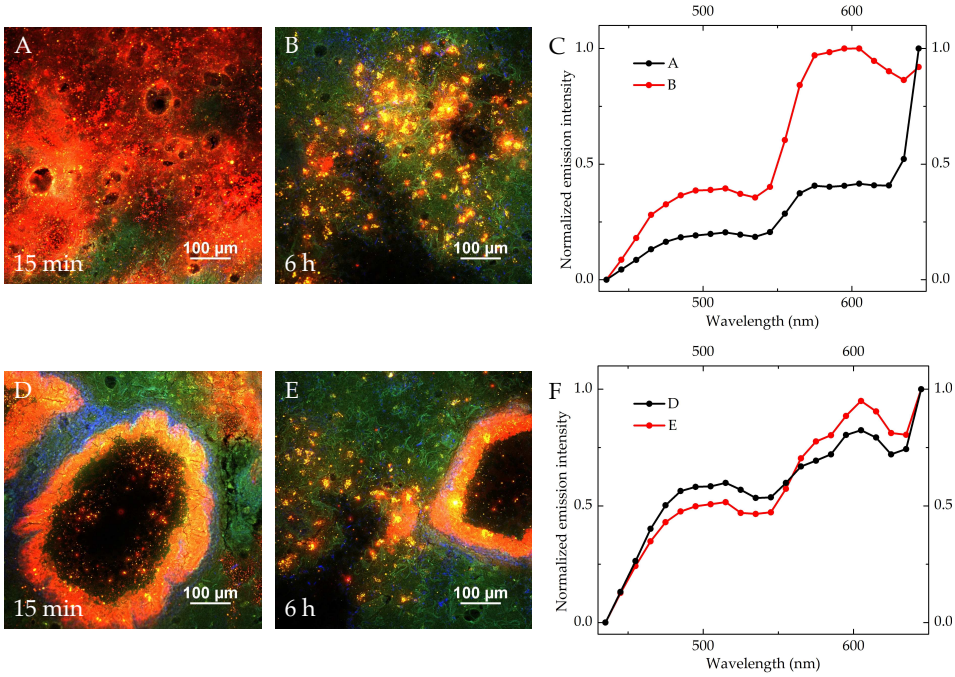

Figure 4.10: Images and spectra acquired on tissues treated with low concentration formulation at different time points. Panel A: image of alveolar structure treated for 15 min. Panel B: image of alveolar structure treated for 6 h. Panel C: spectra acquired on the images in panel A and B. Panel D: image of airways treated for 15 min. Panel E: image of airways treated for 6 h. Panel F: spectra acquired on the images in panel D and E. $\lambda_{exc} = 820$ nm.

ing a similar intensity for the BODIPY signal, the one acquired on Fig. 4.10.B shows a higher intensity in rhodamine emission, indicating that a higher concentration of this dye was present with respect to the BODIPY one. Since both animals were treated with the formulation at the same concentration, the most reasonable explanation for this phenomenon is that in the 6 h between the administration and the animal sacrifice, the tissue was able to metabolize part

of the SM (that was labeled with BODIPY).

The comparison between the images and spectra acquired on the airway structures did not reveal significant differences, except for a slight increase in rhodamine emission intensity in the sample exposed to the formulation for 6 h.

High concentration: 15 min vs 6 h

The images and spectra acquired on the tissues treated with the formulation at high concentration for 15 min or 6 h are reported in Fig. 4.11.

From the images, a yellowish emission due to the formulation can be observed both in alveolar structures and in airways ones. As in the previous comparison, the signal in Fig. 4.11.A and B seems to be randomly diffuse on the alveolar structures. The accumulation of the formulation in the airways epithelium is in accordance with what observed in the previous comparison. The spectra acquired on these samples present the same kind of emission signal as the ones reported in Fig. 4.10. C and F. Nonetheless, in this case the comparison between spectra acquired on structures treated for 15 min or 6 h did not present relevant differences.

An interesting feature can be inferred when looking at Fig.4.11.E. Indeed, a non-stained circular structure can be observed at the higher edge of the image. This structure could be identified with a vessel that, in contrast with airways, is not stained by the formulation since the administration was performed *via* aerosol.

15 min: low vs high concentration

The images and spectra acquired on the tissues treated for 15 min with the formulation at high or low concentration are reported in Fig. 4.12.

As already observed in the previous comparisons, the formulation is differently distributed in the alveolar or airways structures.

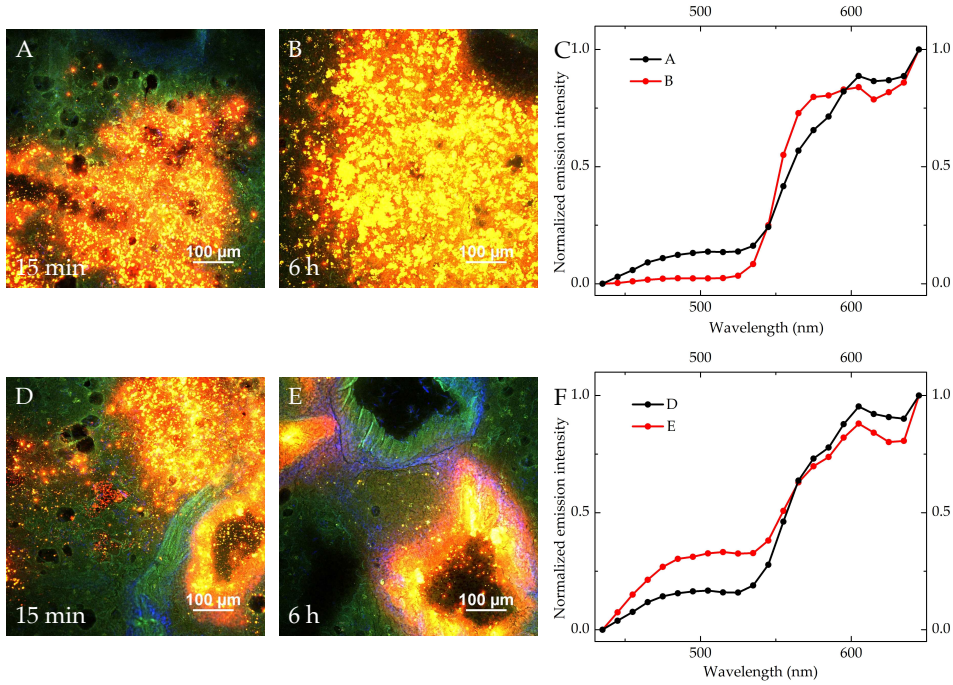

Figure 4.11: Images and spectra acquired on tissues treated with high concentration formulation at different time point. Panel A: image of alveolar structure treated for 15 min. Panel B: image of alveolar structure treated for 6 h. Panel C: spectra acquired on the images in panel A and B. Panel D: image of airways treated for 15 min. Panel E: image of airways treated for 6 h. Panel F: spectra acquired on the images in panel D and E. $\lambda_{exc} = 820$ nm.

Moreover, looking at Fig. 4.12.A and B it is clear that the formulation signal is more yellowish in the sample treated at higher concentration. Although in the comparison shown in Fig. 4.10 this phenomenon was attributed to an higher concentration of rhodamine compared to BODIPY, the spectra reported in Fig. 4.12.C does not indicate any differences in the relative intensities of the two dyes signals. Thus, the difference in the two images (Fig. 4.12.A and B)

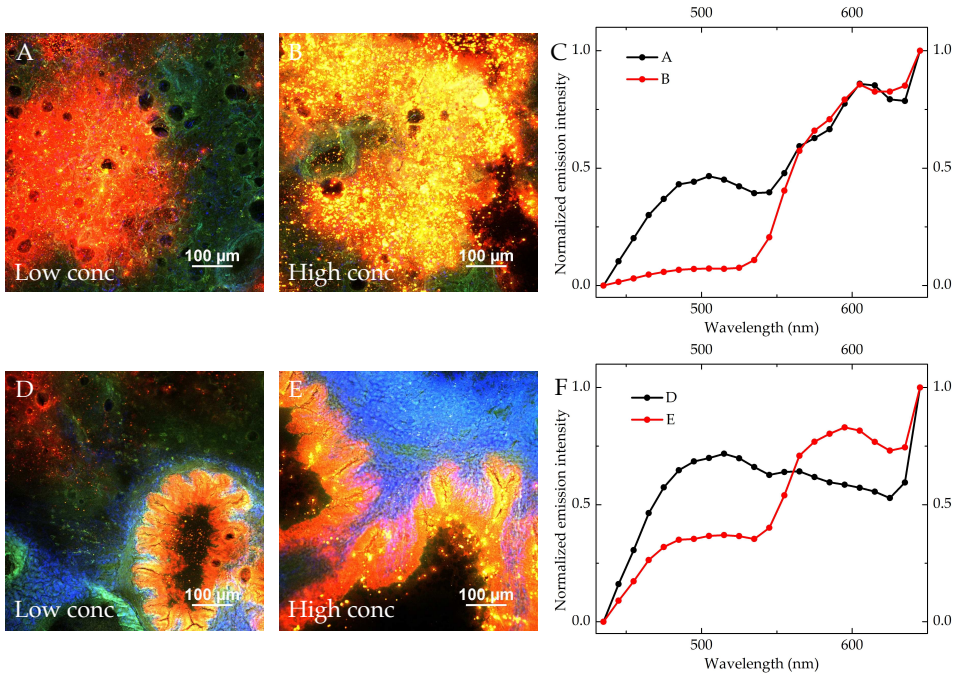

Figure 4.12: Images and spectra acquired on tissues treated for 15 min with different formulation concentration. Panel A: image of alveolar structure treated with formulation at low concentration. Panel B: image of alveolar structure treated with formulation at high concentration. Panel C: spectra acquired on the images in panel A and B. Panel D: image of airways treated with formulation at low concentration. Panel E: image of airways treated with formulation at high concentration. Panel F: spectra acquired on the images in panel D and E. $\lambda_{exc} = 820$ nm.

can be ascribed to the higher concentration of the whole formulation and a probable saturation of the detector dedicated to the red spectral region. Since the BODIPY emission falls within the detectors assigned to both the red and green spectral regions, saturation in the red detector would result in an increase only in the

signal recorded by the green one, leading to an overall shift toward a more yellow signal.

On the other hand, the comparison between the spectra reported in Fig. 4.12.F indicates an higher concentration of rhodamine with respect to BODIPY in Fig. 4.12.E compared to D.

6 h: low vs high concentration

Images and spectra acquired on the tissues treated for 6 h with the formulation at high or low concentration are reported in Fig. 4.13.

The main difference observable between Fig. 4.13.A and B is the intensity of formulation signal. Indeed, both images show a yellow emission, diffused on alveolar structures with the presence of several spots. Nevertheless, the comparison between the relative spectra (Fig. 4.13.C) reveals that in Fig. 4.13.A there is an higher concentration of rhodamine with respect to BODIPY.

This phenomenon has been already observed in the first comparison (see Fig. 4.10.C) but in this case both tissues were treated for 6 h, thus the sole explanation given in that section is not enough to justify what observed in Fig. 4.13.C. Indeed, the different concentration of the formulations administered has to have contributed to this behavior.

Since the low concentration formulation was obtained by dilution of the high concentration one, it is reasonable to hypothesize that the dilution step starts to solubilize the PLGA that composes the particles leading to their partial degradation and to a consequent leak of the labeled SM. The labeled SM is then metabolized by the animal in the 6 h between the administration and the organ excision.

As seen in Fig. 4.12.F, the tissue treated with the formulation at high concentration presents a higher concentration of rhodamine with respect to BODIPY (Fig. 4.13.F).

Moreover, in both Fig. 4.13.D and E a non-stained vessel struc-

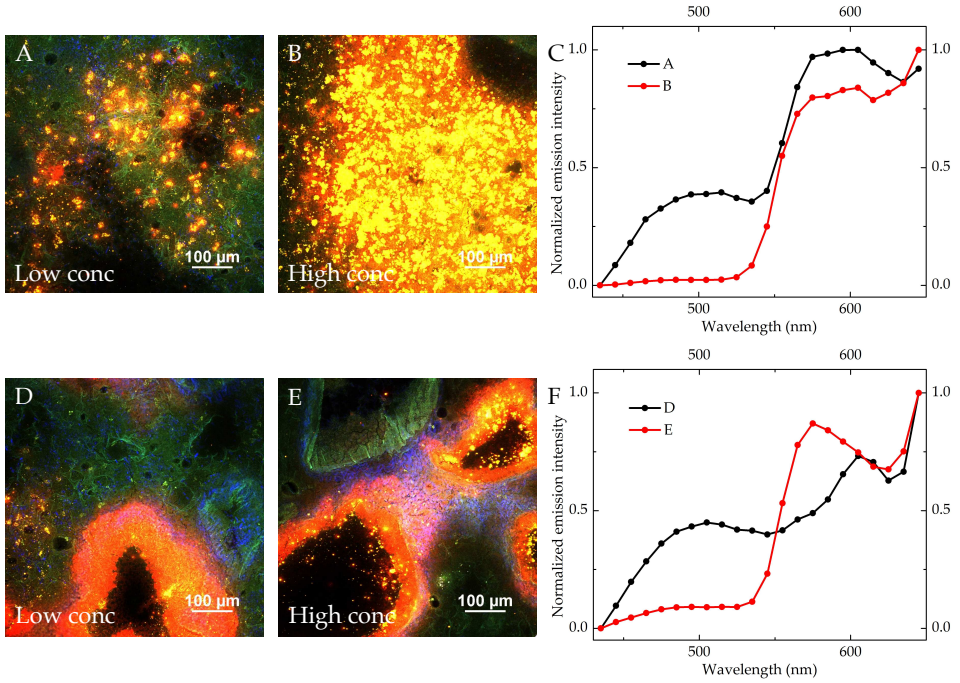

Figure 4.13: Images and spectra acquired on tissues treated for 6 h with different formulation concentration. Panel A: image of alveolar structure treated with formulation at low concentration. Panel B: image of alveolar structure treated with formulation at high concentration. Panel C: spectra acquired on the images in panel A and B. Panel D: image of airways treated with formulation at low concentration. Panel E: image of airways treated with formulation at high concentration. Panel F: spectra acquired on the images in panel D and E. $\lambda_{exc} = 820$ nm.

ture can be observed.

Blue signals comparison

To better analyze the nature of blue signals observed in each tissue a comparison between images acquired with different excitation wavelengths was performed.

The use of two different excitation wavelengths was needed to distinguish between SHG signal and blue signals due to emission. Indeed, due to the blue detector sensitivity range, SHG at 460 nm (obtained with $\lambda_{exc} = 920$ nm) results more intense than SHG at 410 nm (obtain with $\lambda_{exc} = 820$ nm). Nevertheless, in the images there are blue particles (indicated in Fig. 4.14 with white arrows) that show a more intense emission when excited at 820 nm.

Unfortunately, it was not possible to record the spectrum of the blue particles because of their low photo-stability. Nevertheless, since the blue particles were never detected in non-trated tissues and their signal it is not SHG, it is reasonable to link the presence of these particles to the presence of non-labeled SM, whose emission falls in the blue spectral region (see. Fig. 4.9).

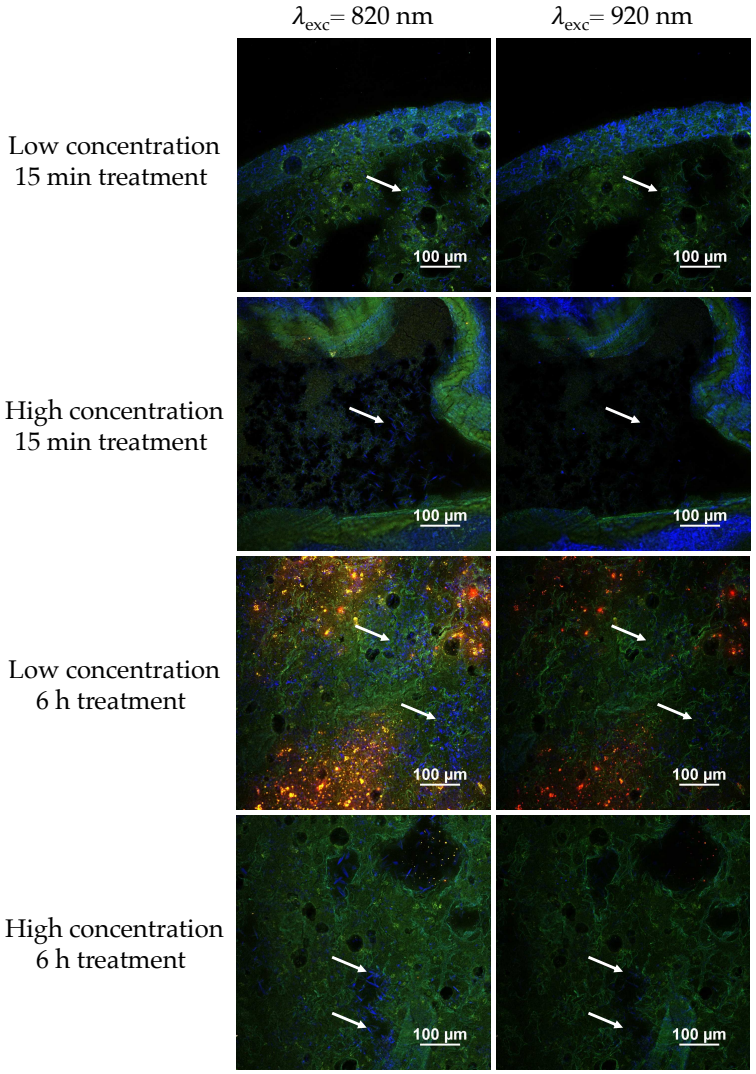

Figure 4.14: Images acquired on each sample with $\lambda_{exc} = 820\,\text{nm}$ and $\lambda_{exc} = 920\,\text{nm}$. The white arrows indicate the blue signals that increase when going from $\lambda_{exc} = 920\,\text{nm}$ to $\lambda_{exc} = 820\,\text{nm}$.

4.4 Conclusions and future perspectives

In Section 4.2, the description of two simple perfusion experiments is reported. The experiments were carried out at Elvesys to culture cells in a microfluidic chip and introduce a medium recirculation device into a microfluidic circuit. The main goal of these experiments was to enhance our knowledge and expertise in handling microfluidic devices. Both cell perfusion experiments, with and without medium recirculation, were successfully conducted, as confirmed by the presence of only a few dead cells at the end of each experiment (Fig. 4.3 and Fig. 4.7). The next step in advancing our understanding of microfluidic devices involves culturing cells on membrane chips. These chips consist of two chambers separated by a semipermeable membrane, which can mimic physiological barriers. Culturing cells on both sides of the membrane could provide a valuable alternative for performing permeation studies without the need for animal models.

In Sec. 4.3 the characterization of novel pharmaceutical formulation in terms of spatial and temporal distribution was performed thanks to 2PM analysis. Thanks to the comparisons described above it was possible to gain important information regarding the formulation behavior in pulmonary tissue:

- The formulation free diffuses in alveolar structure, stains the airways epithelium but is not present around vessel structures.
- The dilution step compromises the particles integrity leading to a leak of SM
- The presence of blue particles could indicate the diffusion of non-labeled SM

Further investigations could focus on tracking the diffusion of the individual components of the formulation to determine the time

point at which the SM is released from the PLGA particles. Indeed with 2PM it is possible to observe the spectrum of a selected region of interest (ROI). In Fig. 4.15 is reported an example.

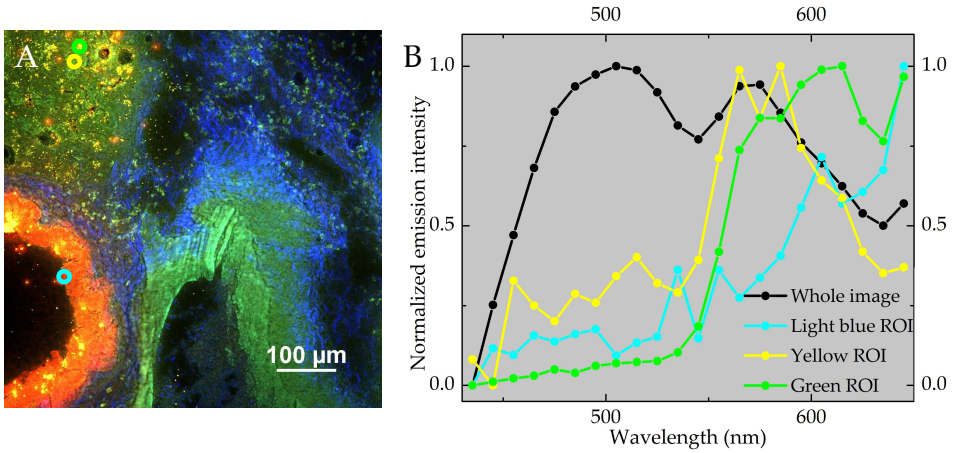

Figure 4.15: Image and spectra acquired on the tissue treated for 6 h with the formulation at high concentration. Panel A: whole image with ROIs highlighted (small colored circles). Panel B: emission spectra acquired on the whole image (black line) and on ROIs (light blue, yellow and green lines). $\lambda_{exc} = 820$ nm.

The spectra reported in Fig. 4.15.B highlight how the spectra acquired on ROIs can be severely different from the one acquired on the whole image. Indeed, in the example here reported, the most intense signal of the whole image is autofluorescence (peaked at $\sim$500 nm), but when looking at the ROIs spectra the dyes signals become predominant.

The light blue ROI selects a limited portion of the airway epithelium and its spectrum reflects the high amount of BODIPY present in that region. In the same way, the spectrum of the green ROI, placed on a red/yellowish spot in the alveolar structure, is characterized by both dyes signals. Interestingly enough, from Fig. 4.15.A we could suppose that the yellow ROI selects a non-stained portion

of the alveolar structure but the spectrum acquired in that region reveals a high accumulation of rhodamine.

Thus, the following information can be inferred by Fig. 4.15:

- The airway epithelium is mostly stained by BODIPY, probably due to the released of the SM from the particles
- The round emissive spots in the alveolar structure are composed by both dyes, probably indicating the presence of the whole formulation
- In the alveolar structure there are regions stained by the sole rhodamine, indicating the possible disaggregation of PLGA particles.

Therefore, this kind of image analysis represents a valuable tool to monitor each dye separately and retrieve pivotal information about their diffusion.

4.5 Materials and methods

Chip seeding

For the chip seeding U-251 MG GFP cells (human glioblastoma astrocytoma transfected with GFP) were cultured in the Dulbecco's Modified Eagle Medium (DMEM) supplemented with 10% fetal bovine serum, 1% penicillin/streptomycin at 37 °C in a humidified 5% CO_2. The cells were suspended, counted using a Burker chamber and immediately used. The chip was seeded by pipetting the cells suspension in the chip chamber. For the perfusion experiments a solution of $7.5 \times 10^5 cells/mL$ was used. The chip was, then, left in the incubator overnight to let the cells adhere to the chip surface.

Cells staining

After the perfusion, the cells were stained inside the chip chamber by pipetting the dyes solutions inside the chamber while with another pipette the medium inside the chamber was removed. This step was repeated three times to completely replace the medium. Then, the cells were left in the incubator for 5 min and washed with PBS before the imaging.

For the experiments a solution of PI at 75 µM and of DAPI at 36 µM were used.

Imaging of pulmonary tissues

The synthesis of the tested formulation, the animal treatment and the slicing of lungs was fully performed by the company.

We were provided with at least 3 lung slices (12 µm thick) for each type of treatment. The slices were placed on a microscope slide and imaged without dipping the objective in water (see Sec. A.1) to avoid any samples movements.

Due to technical reasons the scan of a whole lung slice would have been impractical, so only a central longitudinal portion (1 mm wide) of each sample was imaged.

General conclusions

In this work of thesis the application of three microscopy techniques to biological targets has been presented. Notably, this work aims to highlight the several advantages that the combination of microscopy and spectroscopy can bring. Indeed, the acquisition of hyperspectral images as well as the exploitation of dyes spectroscopic properties, *e.g.* solvatochromism, allowed us to retrieve information difficult to obtain with other analyses.

Each technique was applied to the investigation it was more suitable for. Thus, confocal fluorescence microscopy was applied to the characterization of two novel mitochondria trackers with *in vitro* experiments while, two-photon microscopy was mainly applied to permeation studies of novel formulations in thick biological samples (*ex vivo* models). Finally, micro-Raman spectroscopy was applied to the detection and identification of microplastics in digested biological tissues.

Regarding two-photon microscopy, my PhD work contributed to demonstrate the potential and effectiveness of this technique in applications related to drug delivery. The images and spectra collected using the two-photon microscope not only allowed for the localization of fluorophores within tissues but also provided specific insights into the interaction between the fluorophore and its carrier

in the tissue, as well as the carrier's fate within the tissue—a crucial aspect for drug delivery. These promising results were achieved thanks to a fruitful multidisciplinary collaboration with the ADDRes Lab at the Food and Drug Department of the University of Parma. The lab not only supplied the animal tissues but also played a key role in interpreting the acquired images, particularly those of blank tissues.

As spectroscopists, our expertise in fluorophores, nonlinear phenomena, and environmental effects enabled us to design experiments specifically tailored to extract non-trivial information from microscopy studies.

Confocal microscopy experiments were conducted at NJIT during a secondment carried out within the framework of the Micro4Nano European project. The secondment involved researchers from different European institutions (ICHO-PAN and RBI) with entirely different areas of expertise, namely organic chemistry and theoretical chemistry.

This secondment provided me with the opportunity to utilize a microscopy technique not available at my hosting lab. At the same time, it allowed me to collaborate in a multidisciplinary and international environment, which significantly contributed to the development of various soft skills.

The work conducted with micro-Raman spectroscopy for the identification of microplastics provided another opportunity to exploit "chemical imaging" for detecting contaminants in biological tissues.

This project was particularly challenging due to the research group's limited experience in this field. Nonetheless, we obtained satisfactory results that will be published soon. At the same time, the challenges we encountered helped identify several areas for improvement, such as the use of different experimental procedures (*e.g.*, improved filters and automatic particle recognition), which will be implemented in future analyses in this field.

Lastly, I had the opportunity to collaborate directly with two companies that are highly active in research and development. This experience allowed me to gain exposure to non-academic research environments and to understand some of the potential applications of the research I conducted in a different context.

In conclusion, this PhD work has demonstrated how the integration of advanced microscopy and spectroscopy techniques can offer unique insights into biological systems and contribute to addressing complex scientific challenges. Each method was carefully chosen and applied to specific problems, showcasing their versatility and effectiveness in diverse applications. The experiences gained through multidisciplinary collaborations, international exchanges, and industry partnerships have enriched this research journey, broadening both scientific knowledge and professional skills.

Appendix A

Technical section

A.1 Two-photon microscope

The two-photon microscope primarily exploits two nonlinear phenomena to generate image contrast: two-photon excited fluorescence (TPEF) and second harmonic generation (SHG).

TPEF refers to a fluorescence signal generated by two-photon absorption (TPA), a nonlinear phenomenon that implies the simultaneous absorption of two photons by one molecule. In Fig. A.1 the Jablonski diagrams of one-photon excited fluorescence and TPEF are reported.

As shown in the picture, the main difference between one-photon absorption (OPA) and TPA is the energy of the photons involved. Indeed, if the OPA involves photon with energy falling in the UV-vis spectral region, the energy of TPA photons falls in the NIR spectral region. Thus, exciting photons used for TPA can better penetrate in biological tissue, are less scattered and produce less photobleaching. [165]

Moreover, the probability of two-photon absorption (TPA) to occur is proportional to the square of the excitation intensity (I^2),

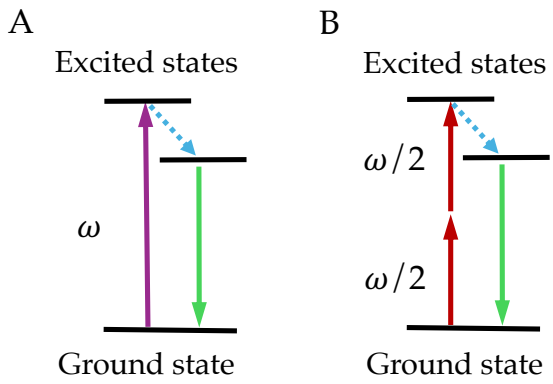

Figure A.1: Panel A: Jablonski energy level diagram of one-photon excited fluorescence. Panel B: Jablonski energy level diagram of two-photon excited fluorescence.

whereas linear absorption is proportional only to I. This quadratic dependence on excitation intensity implies that TPA can occur only within a small volume around the focal point of the excitation light, *i.e.*, the voxel, where the photon density is sufficiently high to allow TPA to take place. [166]

The second nonlinear phenomenon exploited in the application of 2PM was SHG. The SHG process does not involve the absorption or emission of photons but, the conversion of two photons at ω frequency in one photon at 2ω frequency due to the interaction with the sample. In Fig. A.2 the Jablonski diagram of SHG is reported.

SHG has some symmetry constraints regarding the samples by which it can be generated. Indeed, due to the specific selection rules of this phenomenon, only non-centrosymmetric samples can generate a SHG signal. [167] In the projects presented in this thesis only SHG generate by collagen was detected (see Sec. A.3).

As stated for TPA, also SHG requires a high photon density, since two photons interact in the same place at the same time with

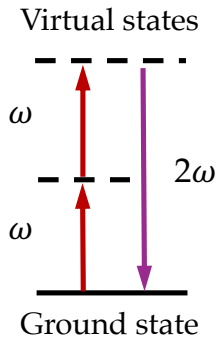

Figure A.2: Jablonski energy level diagram of second harmonic generation.

the samples. The photon density needed for TPA and SHG are reached only in the voxel of a focused laser beam with ultrashort pulses (<1 ps).

The two-photon microscope employed in this thesis is a Nikon A1R MP+ multiphoton upright microscope equipped with a Coherent Chameleon Discovery femtosecond pulsed laser ($\sim$ 100 fs pulse duration with 80 MHz repetition rate and a tunable excitation range of 700-1300 nm). A schematic representation of the instrument is shown in Fig. A.3. A 25× water dipping objective with a numerical aperture of 1.1 and 2 mm working distance was employed for focusing the excitation beam and for collecting the TPEF and SHG. Due to a temporary unavailbility of the objective, for the analysis described in Sec. 4.3 a 20× water dipping objective with a numerical aperture of 0.75 and 0.33 mm working distance was used. For the acquisition of images, the TPEF/SHG signal was detected by four non-descanned detectors (NDDs). Three of the NDDs are high sensitivity Gallium Arsenide Phosphide (GaAsP) photomultiplier tubes (PMTs) while the fourth is a Multi-Alkali PMT. All the NDDs are preceded by a specific filter cube in order to detect different spectral regions simultaneously: blue channel (415-

485 nm), green channel (506-593 nm), red channel (604-679 nm) for the GaAsP PMTs and far-red (698-750 nm) for the Multi-Alkali PMT.

For the acquisition of spectra, the TPEF/SHG the signal was directed by a dichroic mirror to a high sensitivity photomultiplier GaAsP detector, connected to the microscope through an optical fiber and preceded by a dispersive element. This detector allowed the acquisition of the TPEF/SHG signal spectrum in the range of 430 to 650 nm and with a bandwidth of 10 nm.

Images were acquired with a field of view of 500 µm×500 µm with 1024×1024 pixels definition.

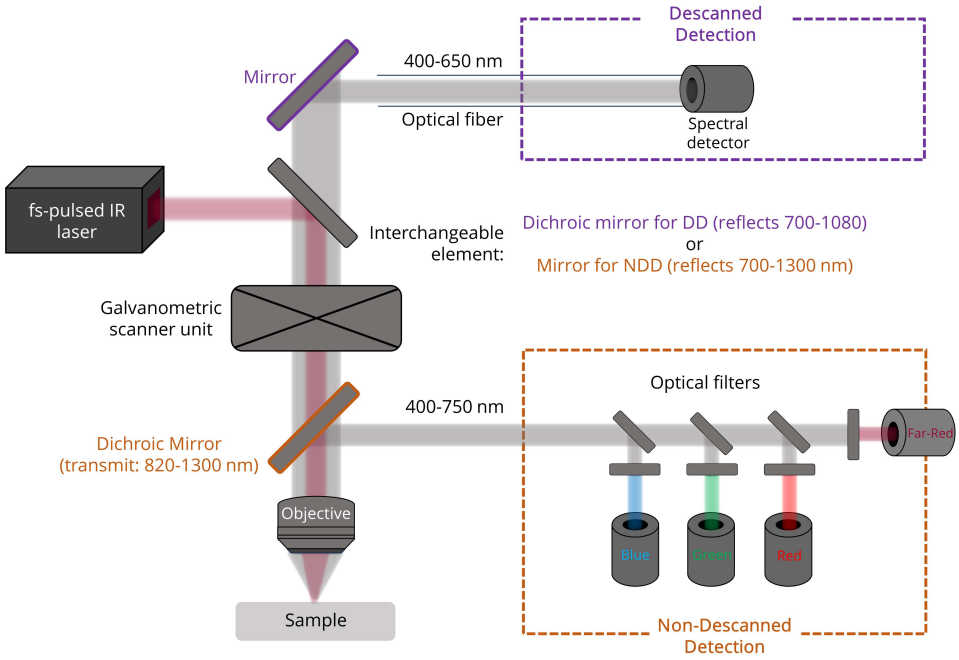

Figure A.3: Two-photon microscope set-up used for the analysis presented in this thesis.

A.2 Spectroscopic measurements

Fluorescence emission spectra were measured using an Edinburgh FLS1000 fluorometers on solutions with absorbance < 0.1 in 1 cm path length cuvettes.

A.3 Non-treated tissues

In this appendix the images acquired on non-treated ocular and skin tissues are reported. For the characterization of formulations in *ex vivo* tissues, it was necessary to study the physiological structures of those samples. Thus, the imaging of the non-treated tissues was performed as a preliminary step at the beginning of all studies reported in this thesis (the preliminary studies performed for the investigation described in Sec. 2.3.1 and in Sec. 4.3 are reported in the respective section for clarity).

Notably, in Sec A.3.1 the characterization of ocular tissues is presented, while in Sec. A.3.2 the analysis of non-treated skin tissue is reported.

All the images reported in this section were acquired on porcine tissues provided by a slaughterhouse (Macello Annoni S.p.a., Busseto, Italy) thanks to the collaboration with the Food and Drug department of the University of Parma. Notably, the group of Prof. Silvia Pescina and Prof. Sara Nicoli handled and prepared the tissues before the imaging.

A.3.1 Ocular tissue

The permeation studies reported in Sec. 2.2.1 and Sec. 2.3.2 evaluate the interaction between the formulation and two different ocular tissues: sclera and cornea.

Sclera

The sclera, commonly known as the "white of the eye", is a connective tissue that represents a protective outer layer for the eye. Sclera is important to maintain the eye shape and provides resistance from both internal and external stimuli. Sclera is mainly composed by collagen fibers arranged in irregular bundles, but also fibroblasts can be found in the collagen matrix. Indeed, fibroblast are cells dedicated to the collagen biosynthesis. [168]

Collagen is a protein organized in non-centrosymmetric fibers which originates the SHG signal. SHG, as described above, falls at half the wavelength used for excitation (Fig. A.4).

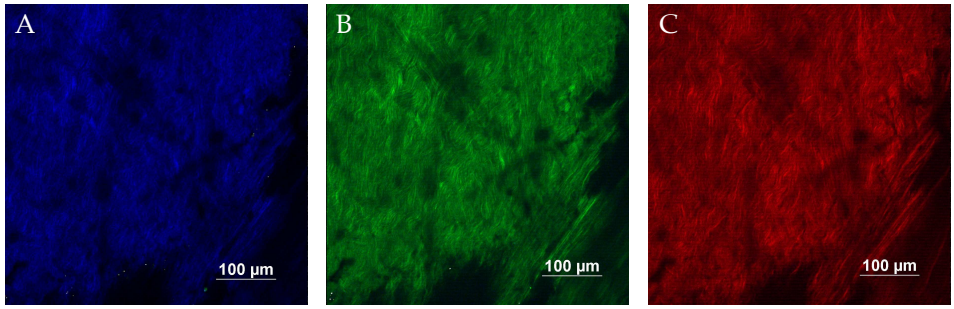

Figure A.4: Sclera SHG signal when exciting the sample at 900 nm (A), 1050 nm (B) and 1280 nm (C).

Indeed, as shown in Fig. A.4, when the samples is excited at 900 nm, the SHG signal falls in the detector dedicated to the blue spectral region, as well as when the sample is excited at 1050 nm or at 1280 nm the SHG falls in the green or red spectral region.

In Fig. A.5 it is reported a 3D reconstruction of the scleral tissue acquired with the two-photon microscope. In the 3D image of the scleral tissue, a green-yellowish fluorescence was detected on the sample surface. This is probably due to residues of choroid, a highly pigmented tissue to which the sclera is in contact with. Notably, the emission is ascribable to elastin fibers and fibroblast.

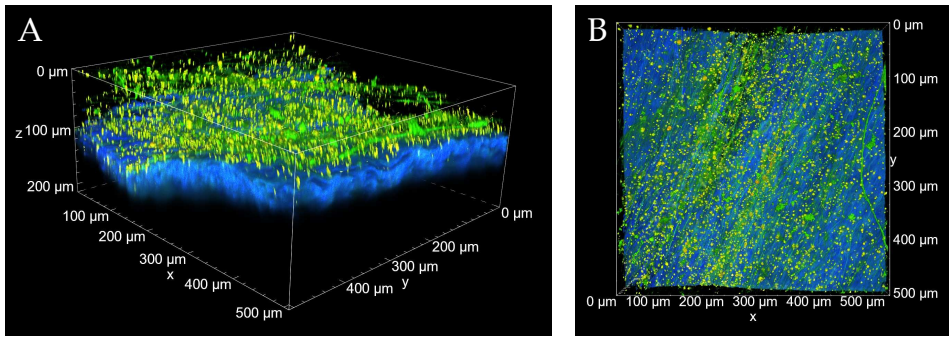

Figure A.5: Images acquired on the scleral tissue with the two-photon microscope. Panel A: 3D image. Panel B: 2D image acquired on the sample surface. $\lambda_{exc} = 820\,\text{nm}$.

Cornea

Cornea is the transparent structure that covers the iris and the pupil in the anterior segment of the eye. It is constituted mainly by three layers: epithelium (the outermost layer), stroma and endothelium (the inner layer). [168]

The epithelium (thickness in porcine: 55 µm-105 µm) is made by several strata of cells that get smaller and smaller the deeper they are located. The stroma (thickness in porcine: 900 µm) is composed by collagen lamellar fibers and corneal fibroblasts, called keratocytes and responsible for collagen generation. Lastly, the endothelium (thickness in porcine: 30 µm) consists in a mono-layer of cells. [168, 169]

When imaged with the 2PM with λ_{exc} =850 nm, the corneal tissue shows two main signals: a green signal detected on the sample surface and a blue signal detected deeper. In the 3D rendering reported in Fig. A.6, both signals can be observed: in the first $\sim$50 µm only the green signal is detected, while below it, a blue signal with green spots is present. Looking at the 2D images reported in Fig. A.7, it is clear that the green signal arises from the

epithelium cells while the blue signal is due to the collagen fibers. Moreover, the green spots present in the collagen matrix are ascribable to keratocytes.

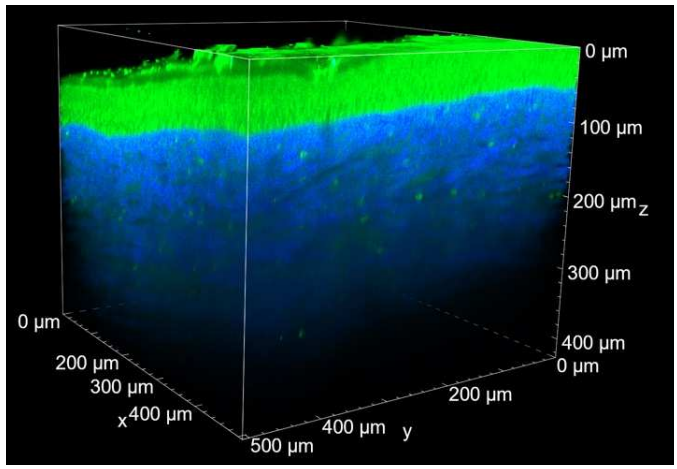

Figure A.6: Corneal tissue 3D rendering imaged with two-photon microscope. $\lambda_{exc} = 850\,\text{nm}$.

Unfortunately, the endothelium could not be detected in Fig. A.6 but it was imaged by flipping the sample upside down (Fig. A.8).

Furthermore, thanks to the acquisition of spectra on the epithelium cells, it was possible to identify the endogenous fluorophore that is responsible for the green emission: the spectrum reported in Fig. A.9 shows a broad band superimposable with the emission of flavoproteins, a class of proteins present in cells. [170]

A.3.2 Skin tissue

The skin is a physical barrier that protects the organism from the external environment, but it also maintains the temperature, electrolyte and fluid balance. [171] The skin is divided in three main layers: epidermis, dermis and hypodermis.

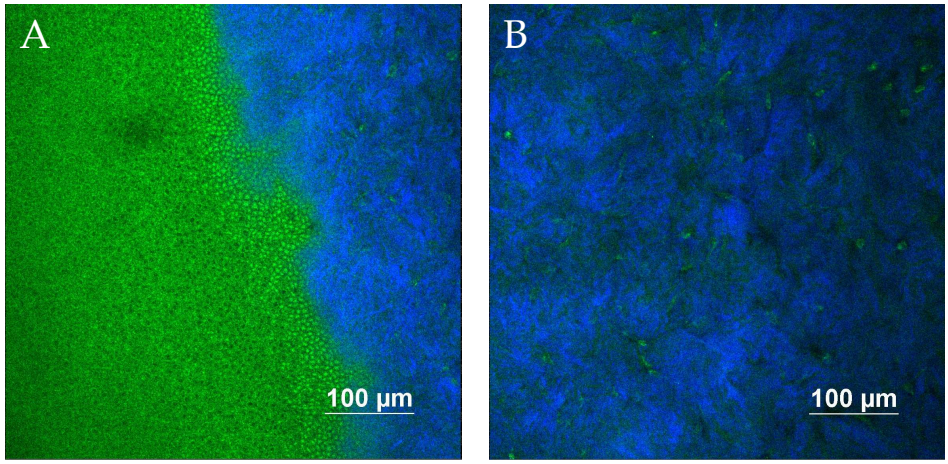

Figure A.7: Images acquired with the two-photon microscope on corneal tissue. Panel A: non flat region of the tissue, showing epithelium cells layers and the initial region of the stroma. Panel B: corneal stroma with keratocytes. $\lambda_{exc} = 850\,\text{nm}$.

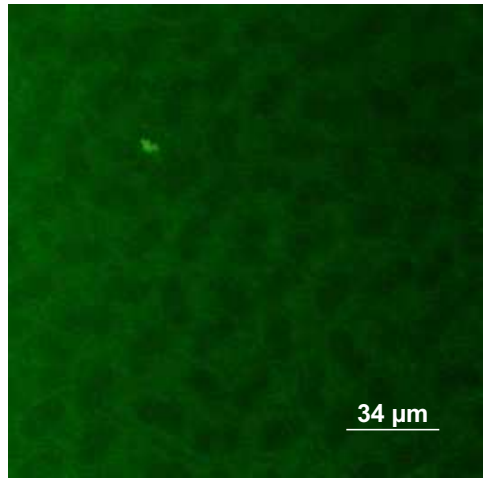

Figure A.8: Endothelium cells imaged with the two-photon microscope. Image size: $170\,\mu\text{m} \times 170\,\mu\text{m}$. $\lambda_{exc} = 850\,\text{nm}$.

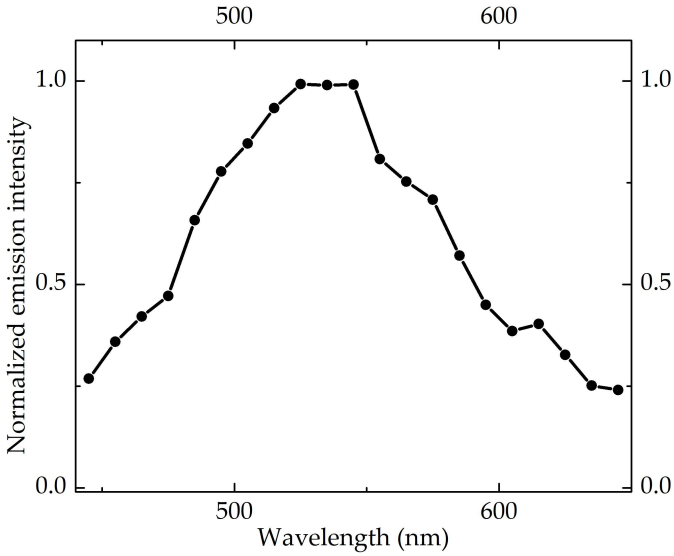

Figure A.9: Normalized emission spectrum acquired on corneal epithelium with the two-photon microscope. $\lambda_{exc} = 850\,\text{nm}$.

Epidermis is the outermost layer of the skin, made of several types of cells, and can be classified into five strata, from the outer to the inner: the stratum corneum, the stratum lucidum, the stratum granulosum, the stratum spinosum and the stratum basale. Epithelial cells, called keratinocytes, are generated in the inner strata and slowly move up to the outer ones, becoming bigger and fuller of keratin. When the stratum corneum is reached, the cells are named corneocytes and are flattered and elongated cells lacking the nuclei and undergoing de-squamation. [172]

Dermis consists mainly of a connective tissue layer that contains hair follicles, different types of glands and blood and lymphatic vessels. The border between dermis and epidermis is not flat but portions of the connective tissue penetrate into the epidermis, generating ridge-like structures. Because of that, this dermis region is called "papillary region" while the inner dermis region is called

reticular dermis. [172]

Hypodermis is the skin innermost layer, composed mainly of subcutaneous fat that contains blood and lymphatic vessels. [172]

The tissue used for the permeation studies presented in this thesis, only had the epidermis and dermis layers.

The images obtained when non-treated skin tissue was imaged with the two-photon microscope are reported in Fig. A.10.

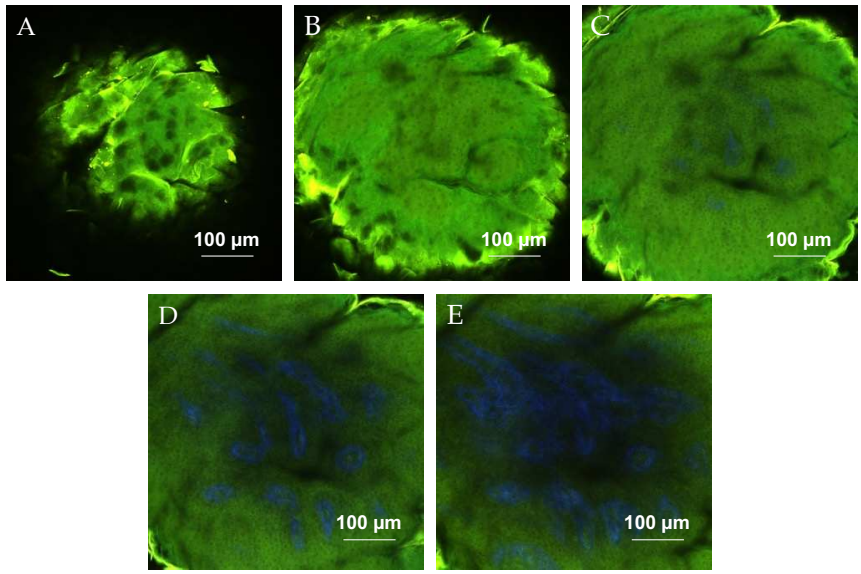

Figure A.10: Images acquired on non-treated skin tissue with the two-photon microscope. Each image was taken 10 µm deeper than the previous one, increasing depth from panel A to panel E. $\lambda_{exc} = 850\,\text{nm}$.

From the images acquired on skin tissue, it can be noticed as the epithelial cells are visible due to their autofluorescence falling in the green spectra region. Fig. A.10.A shows the sample surface where the stratum corneum cells are found. In the images, it is possible to observe how the cells on the surface are bigger, flat, without nuclei and present a more intense emission, while when looking at deeper

strata the cells look smaller and smaller and the nuclei are visible as darker circles. Indeed, the autofluorescence comes mainly from the cells cytoplasm and thus, the nuclei remain darker. In Fig. A.10.C the papillary region starts to be visible, while the blue SHG signal arising from dermis collagen is observable from Fig. A.10.D.

A 3D image of the skin tissue is reported in Fig. A.11.

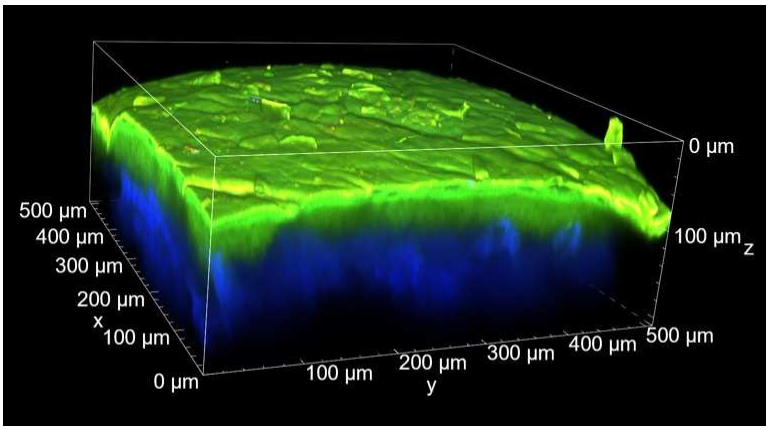

Figure A.11: 3D reconstruction acquired on skin tissue with two-photon microscope. $\lambda_{exc} = 850\,\text{nm}$.

Bibliography

[1] H. Balasubramanian, C. M. Hobson, T.-L. Chew, and J. S. Aaron. *Imagining the future of optical microscopy: everything, everywhere, all at once*. Communications Biology **6**(1), 1096 (2023).

[2] A. J. Wollman, R. Nudd, E. G. Hedlund, and M. C. Leake. *From animaculum to single molecules: 300 years of the light microscope*. Open biology **5**(4), 150019 (2015).

[3] O. D. Lavrentovich. *Confocal fluorescence microscopy*. Characterization of materials pp. 1–15 (2002).

[4] A. D. Elliott. *Confocal microscopy: principles and modern practices*. Current protocols in cytometry **92**(1), e68 (2020).

[5] F. Helmchen and W. Denk. *Deep tissue two-photon microscopy*. Nature methods **2**(12), 932–940 (2005).

[6] R. J. Clark. *Raman microscopy: application to the identification of pigments on medieval manuscripts*. Chemical Society Reviews **24**(3), 187–196 (1995).

[7] R. Frost, T. Kloprogge, and J. Schmidt. *Non-destructive identification of minerals by raman microscopy*. Internet Journal of Vibrational Spectroscopy **3**, 1–13 (1999).

[8] C. F. Araujo, M. M. Nolasco, A. M. Ribeiro, and P. J. Ribeiro-Claro. *Identification of microplastics using raman spectroscopy:*

Latest developments and future prospects. Water research **142**, 426–440 (2018).

[9] C. Pitsalidis, A.-M. Pappa, A. J. Boys, Y. Fu, C.-M. Moysidou, D. van Niekerk, J. Saez, A. Savva, D. Iandolo, and R. M. Owens. *Organic bioelectronics for in vitro systems*. Chemical Reviews **122**(4), 4700–4790 (2021).

[10] T. Hartung and G. Daston. *Are in vitro tests suitable for regulatory use?* Toxicological sciences **111**(2), 233–237 (2009).

[11] C. H. TAKIMOTO and M. WICK. *Preclinical drug development*. In: *Principles of Clinical Pharmacology*, pp. 449–462 (Elsevier, 2007).

[12] N. T. Stewart, K. M. Byrne, H. L. Hosick, J. L. Vierck, and M. V. Dodson. *Traditional and emerging methods for analyzing cell activity in cell culture*. Methods in cell science **22**, 67–78 (2000).

[13] K. V. Vygranenko, Y. M. Poronik, A. Wrzosek, A. Szewczyk, and D. T. Gryko. *Red emissive sulfone-rhodols as mitochondrial imaging agents*. Chemical Communications **57**(63), 7782–7785 (2021).

[14] J. Bereiter-Hahn. *Behavior of mitochondria in the living cell*. International review of cytology **122**, 1–63 (1990).

[15] S. R. Pieczenik and J. Neustadt. *Mitochondrial dysfunction and molecular pathways of disease*. Experimental and molecular pathology **83**(1), 84–92 (2007).

[16] D. C. Chan. *Mitochondrial dynamics and its involvement in disease*. Annual review of pathology: mechanisms of disease **15**(1), 235–259 (2020).

[17] Y. Li, Y. Ma, Q.-Y. Dang, X.-R. Fan, C.-T. Han, S.-Z. Xu, and P.-Y. Li. *Assessment of mitochondrial dysfunction and implications in cardiovascular disorders*. Life Sciences **306**, 120834 (2022).

[18] H. Crawford, M. Dimitriadi, J. Bassin, M. T. Cook, T. F. Abelha, and J. Calvo-Castro. *Mitochondrial targeting and imaging with small organic conjugated fluorophores: A review*.

Chemistry–A European Journal **28**(72), e202202366 (2022).

[19] B. A. Neto, J. R. Corrêa, and R. G. Silva. *Selective mitochondrial staining with small fluorescent probes: importance, design, synthesis, challenges and trends for new markers*. RSC advances **3**(16), 5291–5301 (2013).

[20] X. Zhang, Q. Sun, Z. Huang, L. Huang, and Y. Xiao. *Immobilizable fluorescent probes for monitoring the mitochondria microenvironment: a next step from the classic*. Journal of Materials Chemistry B **7**(17), 2749–2758 (2019).

[21] D. G. Nicholls. *Mitochondrial ion circuits*. Essays in biochemistry **47**, 25–35 (2010).

[22] T. Gayathri, S. Karnewar, S. Kotamraju, and S. P. Singh. *High affinity neutral bodipy fluorophores for mitochondrial tracking*. ACS Medicinal Chemistry Letters **9**(7), 618–622 (2018).

[23] Y. Wang, B. Xu, R. Sun, Y.-J. Xu, and J.-F. Ge. *The application of nitrogen heterocycles in mitochondrial-targeting fluorescent markers with neutral skeletons*. Journal of Materials Chemistry B **8**(33), 7466–7474 (2020).

[24] W. Ma, B. Xu, R. Sun, Y.-J. Xu, and J.-F. Ge. *The application of amide units in the construction of neutral functional dyes for mitochondrial staining*. Journal of Materials Chemistry B **9**(10), 2524–2531 (2021).

[25] J. Jose, A. Loudet, Y. Ueno, R. Barhoumi, R. C. Burghardt, and K. Burgess. *Intracellular imaging of organelles with new water-soluble benzophenoxazine dyes*. Organic & biomolecular chemistry **8**(9), 2052–2059 (2010).

[26] B. A. D Neto, J. R. Corrêa, P. H. Carvalho, D. C. Santos, B. C. Guido, C. C. Gatto, H. C. de Oliveira, M. Fasciotti, M. N. Eberlin, and E. N. d. Silva Jr. *Selective and efficient mitochondrial staining with designed 2, 1, 3-benzothiadiazole derivatives as live cell fluorescence imaging probes*. Journal of the Brazilian Chemical Society **23**, 770–781 (2012).

[27] H. Yao, G. Wei, Y. Liu, H. Yao, Z. Zhu, W. Ye, X. Wu, J. Xu,

and S. Xu. *Synthesis, biological evaluation of fluorescent 23-hydroxybetulinic acid probes, and their cellular localization studies*. ACS Medicinal Chemistry Letters **9**(10), 1030–1034 (2018).

[28] P. E. Kesavan, V. Pandey, M. K. Raza, S. Mori, and I. Gupta. *Water soluble thioglycosylated bodipys for mitochondria targeted cytotoxicity*. Bioorganic Chemistry **91**, 103139 (2019).

[29] Á. Ramos-Torres, E. Avellanal-Zaballa, F. García-Garrido, A. B. Fernández-Martínez, A. Prieto-Castaneda, A. R. Agarrabeitia, J. Bañuelos, I. García-Moreno, F.-J. Lucio-Cazana, and M. J. Ortiz. *Mitochondria selective trackers for long-term imaging based on readily accessible neutral bodipys*. Chemical Communications **57**(43), 5318–5321 (2021).

[30] B. Roy, M. C. Reddy, G. P. Jose, F. C. Niemeyer, J. Voskuhl, and P. Hazra. *All in one: stimuli-responsive, efficient mitotracking, and single source white light emission*. The Journal of Physical Chemistry Letters **12**(4), 1162–1168 (2021).

[31] H. G. Agrawal, P. S. Giri, P. Meena, S. N. Rath, and A. K. Mishra. *A neutral flavin–triphenylamine probe for mitochondrial bioimaging under different microenvironments*. ACS Medicinal Chemistry Letters **14**(12), 1857–1862 (2023).

[32] A. Kawski. *Fluorescence anisotropy: theory and applications of rotational depolarization*. Critical Reviews in Analytical Chemistry **23**(6), 459–529 (1993).

[33] C. Dragonetti, M. Balordi, A. Colombo, D. Roberto, R. Ugo, I. Fortunati, E. Garbin, C. Ferrante, R. Bozio, A. Abbotto, *et al. Two-photon absorption properties of zn (ii) complexes: Unexpected large tpa cross section of dipolar [zny2 (4, 4'-bis (para-di-n-butylaminostyryl)-2, 2'-bipyridine)](y= cl, cf3co2)*. Chemical Physics Letters **475**(4-6), 245–249 (2009).

[34] G. Eisenbrand, B. Pool-Zobel, V. Baker, M. Balls, B. Blaauboer, A. Boobis, A. Carere, S. Kevekordes, J.-C. Lhuguenot, R. Pieters, *et al. Methods of in vitro toxicology*. Food and chemical toxicology **40**(2-3), 193–236 (2002).

[35] A. Kroll, M. H. Pillukat, D. Hahn, and J. Schnekenburger. *Current in vitro methods in nanoparticle risk assessment: limitations and challenges*. European journal of Pharmaceutics and Biopharmaceutics **72**(2), 370–377 (2009).

[36] M. J. Stoddart. *Cell viability assays: introduction*. Mammalian cell viability: methods and protocols pp. 1–6 (2011).

[37] K. W. Dunn, M. M. Kamocka, and J. H. McDonald. *A practical guide to evaluating colocalization in biological microscopy*. American Journal of Physiology-Cell Physiology **300**(4), C723–C742 (2011).

[38] J. Adler and I. Parmryd. *Quantifying colocalization by correlation: the pearson correlation coefficient is superior to the mander's overlap coefficient*. Cytometry Part A **77**(8), 733–742 (2010).

[39] B. Ketterer, B. Neumcke, and P. Läuger. *Transport mechanism of hydrophobic ions through lipid bilayer membranes*. The Journal of Membrane Biology **5**, 225–245 (1971).

[40] R. F. Flewelling and W. L. Hubbell. *Hydrophobic ion interactions with membranes. thermodynamic analysis of tetraphenylphosphonium binding to vesicles*. Biophysical journal **49**(2), 531–540 (1986).

[41] M. F. Ross, G. Kelso, F. H. Blaikie, A. M. James, H. M. Cocheme, A. Filipovska, T. Da Ros, T. Hurd, R. A. Smith, and M. P. Murphy. *Lipophilic triphenylphosphonium cations as tools in mitochondrial bioenergetics and free radical biology*. Biochemistry (Moscow) **70**, 222–230 (2005).

[42] L. Delemotte and M. Tarek. *Molecular dynamics simulations of lipid membrane electroporation*. The Journal of membrane biology **245**(9), 531–543 (2012).

[43] R. F. Flewelling and W. L. Hubbell. *The membrane dipole potential in a total membrane potential model. applications to hydrophobic ion interactions with membranes*. Biophysical journal **49**(2), 541–552 (1986).

[44] B. H. Honig, W. L. Hubbell, and R. F. Flewelling. *Electrostatic*

interactions in membranes and proteins. Annual review of biophysics and biophysical chemistry **15**(1), 163–193 (1986).

[45] R. Mannhold, G. I. Poda, C. Ostermann, and I. V. Tetko. *Calculation of molecular lipophilicity: State-of-the-art and comparison of log p methods on more than 96,000 compounds*. Journal of pharmaceutical sciences **98**(3), 861–893 (2009).

[46] I. Ferraboschi, J. Ovčar, K. V. Vygranenko, S. Yu, A. Minervino, A. Wrzosek, A. Szewczyk, R. Rozza, A. Magistrato, K. D. Belfield, *et al. Neutral rhodol-based dyes expressing localization in mitochondria*. Organic & Biomolecular Chemistry (2024).

[47] A. Ghallab. *In vitro test systems and their limitations*. EXCLI journal **12**, 1024 (2013).

[48] R. R. Tice, C. P. Austin, R. J. Kavlock, and J. R. Bucher. *Improving the human hazard characterization of chemicals: a tox21 update*. Environmental health perspectives **121**(7), 756–765 (2013).

[49] R. Shyam, L. V. K. Reddy, and A. Palaniappan. *Fabrication and characterization techniques of in vitro 3d tissue models*. International Journal of Molecular Sciences **24**(3), 1912 (2023).

[50] K. Rurack and M. Spieles. *Fluorescence quantum yields of a series of red and near-infrared dyes emitting at 600- 1000 nm*. Analytical chemistry **83**(4), 1232–1242 (2011).

[51] K. Swathi, M. Sujith, P. Divya, A. Delledonne, D. A. P. Huu, F. Di Maiolo, F. Terenziani, A. Lapini, A. Painelli, C. Sissa, *et al. From symmetry breaking to symmetry swapping: is kasha's rule violated in multibranched phenyleneethynylenes?* Chemical Science **14**(8), 1986–1996 (2023).

[52] F. Bertocchi, A. Delledonne, G. Vargas-Nadal, F. Terenziani, A. Painelli, and C. Sissa. *Aggregates of cyanine dyes: When molecular vibrations and electrostatic screening make the difference*. The Journal of Physical Chemistry C **127**(21), 10185–10196 (2023).

[53] M. A. Albota, C. Xu, and W. W. Webb. *Two-photon fluorescence*

excitation cross sections of biomolecular probes from 690 to 960 nm. Applied Optics **37**(31), 7352–7356 (1998).

[54] S. de Reguardati, J. Pahapill, A. Mikhailov, Y. Stepanenko, and A. Rebane. *High-accuracy reference standards for two-photon absorption in the 680–1050 nm wavelength range*. Optics Express **24**(8), 9053–9066 (2016).

[55] A. B. Trivedi, N. Kitabatake, and E. Doi. *Toxicity of dimethyl sulfoxide as a solvent in bioassay system with hela cells evaluated colorimetrically with 3-(4, 5-dimethyl thiazol-2-yl)-2, 5-diphenyl-tetrazolium bromide*. Agricultural and biological chemistry **54**(11), 2961–2966 (1990).

[56] V. Nagendrababu, P. Murray, R. Ordinola-Zapata, O. Peters, I. Rôças, J. Siqueira Jr, E. Priya, J. Jayaraman, S. Pulikkotil, and P. Dummer. *A protocol for developing reporting guidelines for laboratory studies in endodontology*. International Endodontic Journal **52**(8), 1090–1095 (2019).

[57] M. Dusinska, E. Rundén-Pran, J. Schnekenburger, and J. Kanno. *Toxicity tests: In vitro and in vivo*. In: *Adverse effects of engineered nanomaterials*, pp. 51–82 (Elsevier, 2017).

[58] Y. Xu, N. Shrestha, V. Préat, and A. Beloqui. *An overview of in vitro, ex vivo and in vivo models for studying the transport of drugs across intestinal barriers*. Advanced Drug Delivery Reviews **175**, 113795 (2021).

[59] R. Kapila, S. Kapila, and R. Vij. *Efficacy of milk-derived bioactive peptides on health by cellular and animal models*. In: *Nutrients in Dairy and their Implications on Health and Disease*, pp. 303–311 (Elsevier, 2017).

[60] S. Shelar, N. K. Mujawar, and S. S. Chakorkar. *In-vivo and ex-vivo methods: advancing the frontiers of ocular pharmacological research*. International Journal Of Pharmaceutical Sciences And Research **15**(1), 78–86 (2024).

[61] S. Pinto, M. E. Pintado, and B. Sarmento. *In vivo, ex vivo and in vitro assessment of buccal permeation of drugs from delivery*

systems. Expert opinion on drug delivery **17**(1), 33–48 (2020).

[62] I. De Hoon, R. Boukherroub, S. C. De Smedt, S. Szunerits, and F. Sauvage. *In vitro and ex vivo models for assessing drug permeation across the cornea*. Molecular Pharmaceutics **20**(7), 3298–3319 (2023).

[63] M. Ghezzi, S. Pescina, C. Padula, P. Santi, E. Del Favero, L. Cantù, and S. Nicoli. *Polymeric micelles in drug delivery: An insight of the techniques for their characterization and assessment in biorelevant conditions*. Journal of Controlled Release **332**, 312–336 (2021).

[64] M. Ghezzi, I. Ferraboschi, A. Delledonne, S. Pescina, C. Padula, P. Santi, C. Sissa, F. Terenziani, and S. Nicoli. *Cyclosporine-loaded micelles for ocular delivery: Investigating the penetration mechanisms*. Journal of Controlled Release **349**, 744–755 (2022).

[65] M. Ghezzi, S. Pescina, A. Delledonne, I. Ferraboschi, C. Sissa, F. Terenziani, P. D. F. R. Remiro, P. Santi, and S. Nicoli. *Improvement of imiquimod solubilization and skin retention via tpgs micelles: exploiting the co-solubilizing effect of oleic acid*. Pharmaceutics **13**(9), 1476 (2021).

[66] O. L. Lanier, M. G. Manfre, C. Bailey, Z. Liu, Z. Sparks, S. Kulkarni, and A. Chauhan. *Review of approaches for increasing ophthalmic bioavailability for eye drop formulations*. Aaps Pharmscitech **22**, 1–16 (2021).

[67] B. Grassiri, Y. Zambito, and A. Bernkop-Schnürch. *Strategies to prolong the residence time of drug delivery systems on ocular surface*. Advances in colloid and interface science **288**, 102342 (2021).

[68] U. B. Kompella, R. R. Hartman, and M. A. Patil. *Extraocular, periocular, and intraocular routes for sustained drug delivery for glaucoma*. Progress in retinal and eye research **82**, 100901 (2021).

[69] A. M. Alambiaga-Caravaca, I. M. Domenech-Monsell,

M. Sebastián-Morelló, M. A. Calatayud-Pascual, V. Merino, V. Rodilla, and A. López-Castellano. *Development, characterization, and ex vivo evaluation of an insert for the ocular administration of progesterone*. International Journal of Pharmaceutics **606**, 120921 (2021).

[70] M. Tighsazzadeh, J. C. Mitchell, and J. S. Boateng. *Development and evaluation of performance characteristics of timolol-loaded composite ocular films as potential delivery platforms for treatment of glaucoma*. International journal of pharmaceutics **566**, 111–125 (2019).

[71] S. A. Gaballa, U. B. Kompella, O. Elgarhy, A. M. Alqahtani, B. Pierscionek, R. G. Alany, and H. Abdelkader. *Corticosteroids in ophthalmology: Drug delivery innovations, pharmacology, clinical applications, and future perspectives*. Drug Delivery and Translational Research **11**, 866–893 (2021).

[72] S. M. Wimer, L. Schoonover, and M. W. Garrison. *Levofloxacin: a therapeutic review*. Clinical therapeutics **20**(6), 1049–1070 (1998).

[73] M. Ghezzi, I. Ferraboschi, A. Fantini, S. Pescina, C. Padula, P. Santi, C. Sissa, and S. Nicoli. *Hyaluronic acid–pva films for the simultaneous delivery of dexamethasone and levofloxacin to ocular tissues*. International Journal of Pharmaceutics **638**, 122911 (2023).

[74] P. Hazra, D. Chakrabarty, A. Chakraborty, and N. Sarkar. *Intramolecular charge transfer and solvation dynamics of nile red in the nanocavity of cyclodextrins*. Chemical physics letters **388**(1-3), 150–157 (2004).

[75] A. Ray, S. Das, and N. Chattopadhyay. *Aggregation of nile red in water: Prevention through encapsulation in β-cyclodextrin*. ACS omega **4**(1), 15–24 (2019).

[76] B. Boldrini, E. Cavalli, A. Painelli, and F. Terenziani. *Polar dyes in solution: A joint experimental and theoretical study of absorption and emission band shapes*. The Journal of Physical Chemistry A

106(26), 6286–6294 (2002).

[77] S.-W. Teng, H.-Y. Tan, J.-L. Peng, H.-H. Lin, K. H. Kim, W. Lo, Y. Sun, W.-C. Lin, S.-J. Lin, S.-H. Jee, *et al. Multiphoton autofluorescence and second-harmonic generation imaging of the ex vivo porcine eye*. Investigative ophthalmology & visual science **47**(3), 1216–1224 (2006).

[78] M. Zyablitskaya, E. L. Munteanu, T. Nagasaki, and D. C. Paik. *Second harmonic generation signals in rabbit sclera as a tool for evaluation of therapeutic tissue cross-linking (txl) for myopia*. Journal of Visualized Experiments: JoVE (131), 56385 (2018).

[79] M. G. Fernandes, L. P. da Silva, and A. P. Marques. *Skin mechanobiology and biomechanics: From homeostasis to wound healing*. Advances in Biomechanics and Tissue Regeneration pp. 343–360 (2019).

[80] L. Zhao, J. Chen, B. Bai, G. Song, J. Zhang, H. Yu, S. Huang, Z. Wang, and G. Lu. *Topical drug delivery strategies for enhancing drug effectiveness by skin barriers, drug delivery systems and individualized dosing*. Frontiers in Pharmacology **14**, 1333986 (2024).

[81] N. Mumtaz, M. Imran, A. Javaid, S. Latif, N. Hussain, and L. Mitu. *Nanomaterials for targeted drug delivery through skin to treat various diseases: Recent trends and future perspective*. Journal of Chemistry **2023**(1), 3861758 (2023).

[82] L. Sercombe, T. Veerati, F. Moheimani, S. Y. Wu, A. K. Sood, and S. Hua. *Advances and challenges of liposome assisted drug delivery*. Frontiers in pharmacology **6**, 286 (2015).

[83] P. Liu, G. Chen, and J. Zhang. *A review of liposomes as a drug delivery system: current status of approved products, regulatory environments, and future perspectives*. Molecules **27**(4), 1372 (2022).

[84] V. G. S. Jyothi, R. Bulusu, B. V. K. Rao, M. Pranothi, S. Banda, P. K. Bolla, and N. Kommineni. *Stability characterization for pharmaceutical liposome product development with focus on regulatory considerations: An update*. International Journal of Phar-

maceutics **624**, 122022 (2022).

[85] M. S. Bin Sayeed, S. M. R. Karim, T. Sharmin, and M. M. Morshed. *Critical analysis on characterization, systemic effect, and therapeutic potential of beta-sitosterol: a plant-derived orphan phytosterol*. Medicines **3**(4), 29 (2016).

[86] S. Chanioti, M. Katsouli, and C. Tzia. *β-sitosterol as a functional bioactive*. In: *A centum of valuable plant bioactives*, pp. 193–212 (Elsevier, 2021).

[87] M. S. Ferreira, J. M. Sousa Lobo, and I. F. Almeida. *Sensitive skin: Active ingredients on the spotlight*. International Journal of Cosmetic Science **44**(1), 56–73 (2022).

[88] I. Pantelic and B. Cuckovic. *Alkyl polyglucosides: An emerging class of sugar surfactants*. In: *Alkyl polyglucosides*, pp. 1–19 (Elsevier, 2014).

[89] N. Ventosa, J. Veciana, S. Sala, and M. Cano. *Method for obtaining micro-and nano-disperse systems* (2010). US Patent 7,754,777.

[90] M. Cano-Sarabia, N. Ventosa, S. Sala, C. Patino, R. Arranz, and J. Veciana. *Preparation of uniform rich cholesterol unilamellar nanovesicles using co2-expanded solvents*. Langmuir **24**(6), 2433–2437 (2008).

[91] I. Cabrera, E. Elizondo, O. Esteban, J. L. Corchero, M. Melgarejo, D. Pulido, A. Cordoba, E. Moreno, U. Unzueta, E. Vazquez, *et al. Multifunctional nanovesicle-bioactive conjugates prepared by a one-step scalable method using co2-expanded solvents*. Nano letters **13**(8), 3766–3774 (2013).

[92] M. Alcaina-Hernando, I. Malvacio, I. Ferraboschi, C. Huck-Iriart, A. Bianchera, S. Sala, J. S. Pedersen, L. Ferrer-Tasies, S. Pescina, C. Sissa, *et al. A new plant-based drug delivery platform based on alkyl polyglucosides and β-sitosterol nanovesicles for topical delivery*. Applied Materials Today **41**, 102467 (2024).

[93] B. Mansoori, S. S. Shotorbani, and B. Baradaran. *Rna interference and its role in cancer therapy*. Advanced pharmaceutical bulletin **4**(4), 313 (2014).

[94] Y. Deng, C. C. Wang, K. W. Choy, Q. Du, J. Chen, Q. Wang, L. Li, T. K. H. Chung, and T. Tang. *Therapeutic potentials of gene silencing by rna interference: principles, challenges, and new strategies*. Gene **538**(2), 217–227 (2014).

[95] Y. Xin, M. Huang, W. W. Guo, Q. Huang, L. z. Zhang, and G. Jiang. *Nano-based delivery of rnai in cancer therapy*. Molecular cancer **16**, 1–9 (2017).

[96] K. A. Whitehead, R. Langer, and D. G. Anderson. *Knocking down barriers: advances in sirna delivery*. Nature reviews Drug discovery **8**(2), 129–138 (2009).

[97] S. M. Dizaj, S. Jafari, and A. Y. Khosroushahi. *A sight on the current nanoparticle-based gene delivery vectors*. Nanoscale research letters **9**, 1–9 (2014).

[98] C. Liu and N. Zhang. *Nanoparticles in gene therapy: principles, prospects, and challenges*. Progress in molecular biology and translational science **104**, 509–562 (2011).

[99] J.-M. Lee, T.-J. Yoon, and Y.-S. Cho. *Recent developments in nanoparticle-based sirna delivery for cancer therapy*. BioMed research international **2013**(1), 782041 (2013).

[100] Q. Xu, C.-H. Wang, and D. Wayne Pack. *Polymeric carriers for gene delivery: chitosan and poly (amidoamine) dendrimers*. Current pharmaceutical design **16**(21), 2350–2368 (2010).

[101] Z. Mao, L. Ma, Y. Jiang, M. Yan, C. Gao, and J. Shen. *N, n, n-trimethylchitosan chloride as a gene vector: Synthesis and application*. Macromolecular Bioscience **7**(6), 855–863 (2007).

[102] C. Lian, K. Yoshida, C. Nogues, and I. D. Samuel. *Organic light-emitting diode based fluorescence sensing system for dna detection*. Advanced Materials Technologies **7**(5), 2100806 (2022).

[103] M. Digiuni, P. Fogagnolo, and L. Rossetti. *A review of the use of latanoprost for glaucoma since its launch*. Expert opinion on pharmacotherapy **13**(5), 723–745 (2012).

[104] Y. Yang and A. Lockwood. *Topical ocular drug delivery systems: Innovations for an unmet need*. Experimental Eye Research **218**,

109006 (2022).

[105] F. A. Maulvi, K. H. Shetty, D. T. Desai, D. O. Shah, and M. D. Willcox. *Recent advances in ophthalmic preparations: Ocular barriers, dosage forms and routes of administration*. International journal of pharmaceutics **608**, 121105 (2021).

[106] J. J. López-Cano, M. A. González-Cela-Casamayor, V. Andrés-Guerrero, R. Herrero-Vanrell, and I. T. Molina-Martínez. *Liposomes as vehicles for topical ophthalmic drug delivery and ocular surface protection*. Expert opinion on drug delivery **18**(7), 819–847 (2021).

[107] M. Guter and M. Breunig. *Hyaluronan as a promising excipient for ocular drug delivery*. European journal of pharmaceutics and biopharmaceutics **113**, 34–49 (2017).

[108] J. Lin, H. Wu, Y. Wang, J. Lin, Q. Chen, and X. Zhu. *Preparation and ocular pharmacokinetics of hyaluronan acid-modified mucoadhesive liposomes*. Drug Delivery **23**(4), 1144–1151 (2016).

[109] A. López-Machado, N. Díaz-Garrido, A. Cano, M. Espina, J. Badia, L. Baldomà, A. C. Calpena, E. B. Souto, M. L. García, and E. Sánchez-López. *Development of lactoferrin-loaded liposomes for the management of dry eye disease and ocular inflammation*. Pharmaceutics **13**(10), 1698 (2021).

[110] A. J. Bron, C. S. de Paiva, S. K. Chauhan, S. Bonini, E. E. Gabison, S. Jain, E. Knop, M. Markoulli, Y. Ogawa, V. Perez, *et al. Tfos dews ii pathophysiology report*. The ocular surface **15**(3), 438–510 (2017).

[111] M. Brugnera, M. V. de-la Torre, M. A. González-Cela-Casamayor, F. M. González-Fernández, I. Ferraboschi, V. Andrés-Guerrero, S. Nicoli, C. Sissa, S. Pescina, R. Herrero-Vanrell, and I. Bravo-Osuna. *Disclosing long-term tolerance, efficacy and penetration properties of hyaluronic acid-coated latanoprost-loaded liposomes as chronic glaucoma therapy*. Journal of controlled release (2025). In preparation.

[112] Y. W. Jun, H. R. Kim, Y. J. Reo, M. Dai, and K. H. Ahn. *Address-*

ing the autofluorescence issue in deep tissue imaging by two-photon microscopy: the significance of far-red emitting dyes. Chemical science **8**(11), 7696–7704 (2017).

[113] W. Qin, P. Zhang, H. Li, J. W. Lam, Y. Cai, R. T. Kwok, J. Qian, W. Zheng, and B. Z. Tang. *Ultrabright red aiegens for two-photon vascular imaging with high resolution and deep penetration*. Chemical Science **9**(10), 2705–2710 (2018).

[114] M. Vicario-de-la Torre, J. M. Benítez-del Castillo, E. Vico, M. Guzmán, B. de Las-Heras, R. Herrero-Vanrell, and I. T. Molina-Martinez. *Design and characterization of an ocular topical liposomal preparation to replenish the lipids of the tear film*. Investigative ophthalmology & visual science **55**(12), 7839–7847 (2014).

[115] M. A. Gonzalez Cela Casamayor, J. J. Lopez Cano, V. Andrés Guerrero, R. Herrero Vanrell, J. M. Benitez del Castillo, and I. T. Molina Martínez. *A novel osmoprotective liposomal formulation from synthetic phospholipids to reduce in vitro hyperosmolar stress in dry eye treatments*. Journal of Liposome Research **33**(2), 117–128 (2023).

[116] N. Razali, W. W. Abdullah, and N. M. Zikir. *Effect of thermo-photocatalytic process using zinc oxide on degradation of macro/micro-plastic in aqueous environment*. J. Sustain. Sci. Manag **15**(6), 1–14 (2020).

[117] N. B. Hartmann, T. Huffer, R. C. Thompson, M. Hassellov, A. Verschoor, A. E. Daugaard, S. Rist, T. Karlsson, N. Brennholt, M. Cole, *et al. Are we speaking the same language? recommendations for a definition and categorization framework for plastic debris* (2019).

[118] A. Wahl, C. Le Juge, M. Davranche, H. El Hadri, B. Grassl, S. Reynaud, and J. Gigault. *Nanoplastic occurrence in a soil amended with plastic debris*. Chemosphere **262**, 127784 (2021).

[119] D. Gola, P. K. Tyagi, A. Arya, N. Chauhan, M. Agarwal, S. Singh, and S. Gola. *The impact of microplastics on marine*

environment: A review. Environmental Nanotechnology, Monitoring & Management **16**, 100552 (2021).

[120] C. Li, R. Busquets, and L. C. Campos. *Assessment of microplastics in freshwater systems: A review*. Science of the Total Environment **707**, 135578 (2020).

[121] A. A. de Souza Machado, W. Kloas, C. Zarfl, S. Hempel, and M. C. Rillig. *Microplastics as an emerging threat to terrestrial ecosystems*. Global change biology **24**(4), 1405–1416 (2018).

[122] J. C. Prata. *Airborne microplastics: consequences to human health?* Environmental pollution **234**, 115–126 (2018).

[123] Y. Deng, Y. Zhang, B. Lemos, and H. Ren. *Tissue accumulation of microplastics in mice and biomarker responses suggest widespread health risks of exposure*. Scientific reports **7**(1), 46687 (2017).

[124] P. Schwabl, S. Köppel, P. Königshofer, T. Bucsics, M. Trauner, T. Reiberger, and B. Liebmann. *Detection of various microplastics in human stool: a prospective case series*. Annals of internal medicine **171**(7), 453–457 (2019).

[125] C. G. Avio, S. Gorbi, M. Milan, M. Benedetti, D. Fattorini, G. d'Errico, M. Pauletto, L. Bargelloni, and F. Regoli. *Pollutants bioavailability and toxicological risk from microplastics to marine mussels*. Environmental pollution **198**, 211–222 (2015).

[126] R. De Stephanis, J. Giménez, E. Carpinelli, C. Gutierrez-Exposito, and A. Cañadas. *As main meal for sperm whales: plastics debris*. Marine pollution bulletin **69**(1-2), 206–214 (2013).

[127] E. Besseling, B. Wang, M. Lurling, and A. A. Koelmans. *Nanoplastic affects growth of s. obliquus and reproduction of d. magna*. Environmental science & technology **48**(20), 12336–12343 (2014).

[128] K. Mattsson, M. T. Ekvall, L.-A. Hansson, S. Linse, A. Malmendal, and T. Cedervall. *Altered behavior, physiology, and metabolism in fish exposed to polystyrene nanoparticles*. Environmental science & technology **49**(1), 553–561 (2015).

[129] C. M. Rochman, T. Kurobe, I. Flores, and S. J. Teh. *Early warning signs of endocrine disruption in adult fish from the ingestion of polyethylene with and without sorbed chemical pollutants from the marine environment*. Science of the total environment **493**, 656–661 (2014).

[130] R. E. Zurub, S. Bainbridge, L. Rahman, S. Halappanavar, D. El-Chaâr, and M. G. Wade. *Particulate contamination of human placenta: plastic and non-plastic*. Environmental Advances **17**, 100555 (2024).

[131] R. E. Zurub, Y. Cariaco, M. G. Wade, and S. A. Bainbridge. *Microplastics exposure: implications for human fertility, pregnancy and child health*. Frontiers in Endocrinology **14**, 1330396 (2024).

[132] C.-W. Yu, T. C. Luk, and V. H.-C. Liao. *Long-term nanoplastics exposure results in multi and trans-generational reproduction decline associated with germline toxicity and epigenetic regulation in caenorhabditis elegans*. Journal of hazardous materials **412**, 125173 (2021).

[133] A. Ragusa, A. Svelato, C. Santacroce, P. Catalano, V. Notarstefano, O. Carnevali, F. Papa, M. C. A. Rongioletti, F. Baiocco, S. Draghi, *et al. Plasticenta: First evidence of microplastics in human placenta*. Environment international **146**, 106274 (2021).

[134] F. Amereh, N. Amjadi, A. Mohseni-Bandpei, S. Isazadeh, Y. Mehrabi, A. Eslami, Z. Naeiji, and M. Rafiee. *Placental plastics in young women from general population correlate with reduced foetal growth in iugr pregnancies*. Environmental pollution **314**, 120174 (2022).

[135] T. Braun, L. Ehrlich, W. Henrich, S. Koeppel, I. Lomako, P. Schwabl, and B. Liebmann. *Detection of microplastic in human placenta and meconium in a clinical setting*. Pharmaceutics **13**(7), 921 (2021).

[136] L. Zhu, J. Zhu, R. Zuo, Q. Xu, Y. Qian, and A. Lihui. *Identification of microplastics in human placenta using laser direct infrared spectroscopy*. Science of the Total Environment **856**, 159060

(2023).

[137] M. PrabhuDas, E. Bonney, K. Caron, S. Dey, A. Erlebacher, A. Fazleabas, S. Fisher, T. Golos, M. Matzuk, J. M. McCune, *et al. Immune mechanisms at the maternal-fetal interface: perspectives and challenges*. Nature immunology **16**(4), 328–334 (2015).

[138] P. Nancy, E. Tagliani, C.-S. Tay, P. Asp, D. E. Levy, and A. Erlebacher. *Chemokine gene silencing in decidual stromal cells limits t cell access to the maternal-fetal interface*. Science **336**(6086), 1317–1321 (2012).

[139] J. Xue, Z. Xu, X. Hu, Y. Lu, Y. Zhao, and H. Zhang. *Microplastics in maternal amniotic fluid and their associations with gestational age*. Science of the Total Environment **920**, 171044 (2024).

[140] E. Bongaerts, L. L. Lecante, H. Bové, M. B. Roeffaers, M. Ameloot, P. A. Fowler, and T. S. Nawrot. *Maternal exposure to ambient black carbon particles and their presence in maternal and fetal circulation and organs: an analysis of two independent population-based observational studies*. The Lancet Planetary Health **6**(10), e804–e811 (2022).

[141] K. Enders, R. Lenz, C. A. Stedmon, and T. G. Nielsen. *Abundance, size and polymer composition of marine microplastics $\geq$ 10 µm in the atlantic ocean and their modelled vertical distribution*. Marine pollution bulletin **100**(1), 70–81 (2015).

[142] M. Di and J. Wang. *Microplastics in surface waters and sediments of the three gorges reservoir, china*. Science of the Total Environment **616**, 1620–1627 (2018).

[143] M. M.-L. Leung, Y.-W. Ho, C.-H. Lee, Y. Wang, M. Hu, K. W. H. Kwok, S.-L. Chua, and J. K.-H. Fang. *Improved raman spectroscopy-based approach to assess microplastics in seafood*. Environmental Pollution **289**, 117648 (2021).

[144] A. Ragusa, V. Notarstefano, A. Svelato, A. Belloni, G. Gioacchini, C. Blondeel, E. Zucchelli, C. De Luca, S. D'Avino, A. Gulotta, *et al. Raman microspectroscopy detection and charac-*

terisation of microplastics in human breastmilk. Polymers **14**(13), 2700 (2022).

[145] S. L. Wright, J. M. Levermore, and F. J. Kelly. *Raman spectral imaging for the detection of inhalable microplastics in ambient particulate matter samples*. Environmental science & technology **53**(15), 8947–8956 (2019).

[146] A. Turner and M. Filella. *The role of titanium dioxide on the behaviour and fate of plastics in the aquatic environment*. Science of the Total Environment **869**, 161727 (2023).

[147] M. Nicola, C. Mastrippolito, and A. Masic. *Iron oxide-based pigments and their use in history*. Iron Oxides: From Nature to Applications pp. 545–566 (2016).

[148] E. C. Sklute, S. Kashyap, M. D. Dyar, J. F. Holden, T. Tague, P. Wang, and S. J. Jaret. *Spectral and morphological characteristics of synthetic nanophase iron (oxyhydr) oxides*. Physics and chemistry of minerals **45**(1), 1–26 (2018).

[149] D. Wu, Y. Feng, R. Wang, J. Jiang, Q. Guan, X. Yang, H. Wei, Y. Xia, and Y. Luo. *Pigment microparticles and microplastics found in human thrombi based on raman spectral evidence*. Journal of advanced research **49**, 141–150 (2023).

[150] A. Dehaut, A.-L. Cassone, L. Frère, L. Hermabessiere, C. Himber, E. Rinnert, G. Rivière, C. Lambert, P. Soudant, A. Huvet, *et al. Microplastics in seafood: Benchmark protocol for their extraction and characterization*. Environmental pollution **215**, 223–233 (2016).

[151] A. Karami, A. Golieskardi, C. K. Choo, N. Romano, Y. B. Ho, and B. Salamatinia. *A high-performance protocol for extraction of microplastics in fish*. Science of the total environment **578**, 485–494 (2017).

[152] G. M. Whitesides. *The origins and the future of microfluidics*. nature **442**(7101), 368–373 (2006).

[153] D. B. Weibel and G. M. Whitesides. *Applications of microfluidics in chemical biology*. Current opinion in chemical biology **10**(6),

584–591 (2006).

[154] D. J. Beebe, G. A. Mensing, and G. M. Walker. *Physics and applications of microfluidics in biology*. Annual review of biomedical engineering **4**(1), 261–286 (2002).

[155] Y. Liu and H. Lu. *Microfluidics in systems biology—hype or truly useful?* Current opinion in biotechnology **39**, 215–220 (2016).

[156] D. Huh, B. D. Matthews, A. Mammoto, M. Montoya-Zavala, H. Y. Hsin, and D. E. Ingber. *Reconstituting organ-level lung functions on a chip*. Science **328**(5986), 1662–1668 (2010).

[157] A. Varone, J. K. Nguyen, L. Leng, R. Barrile, J. Sliz, C. Lucchesi, N. Wen, A. Gravanis, G. A. Hamilton, K. Karalis, *et al. A novel organ-chip system emulates three-dimensional architecture of the human epithelia and the mechanical forces acting on it*. Biomaterials **275**, 120957 (2021).

[158] G. J. Mahler, M. B. Esch, R. P. Glahn, and M. L. Shuler. *Characterization of a gastrointestinal tract microscale cell culture analog used to predict drug toxicity*. Biotechnology and bioengineering **104**(1), 193–205 (2009).

[159] G. D. Vatine, R. Barrile, M. J. Workman, S. Sances, B. K. Barriga, M. Rahnama, S. Barthakur, M. Kasendra, C. Lucchesi, J. Kerns, *et al. Human ipsc-derived blood-brain barrier chips enable disease modeling and personalized medicine applications*. Cell stem cell **24**(6), 995–1005 (2019).

[160] L. C. Crowley, A. P. Scott, B. J. Marfell, J. A. Boughaba, G. Chojnowski, and N. J. Waterhouse. *Measuring cell death by propidium iodide uptake and flow cytometry*. Cold Spring Harbor Protocols **2016**(7), pdb–prot087163 (2016).

[161] L. Muiznieks and I. Ferraboschi. *Perfusion cell culture with recirculationn*. `https://microfluidics-innovation-center.com/application-notes/perfusion-cell-culture/` (2024 (accessed December 31, 2024)).

[162] I. Pavlova, K. R. Hume, S. A. Yazinski, R. M. Peters, R. S. Weiss, and W. W. Webb. *Multiphoton microscopy as a diagnostic*

imaging modality for lung cancer. In: *Multiphoton Microscopy in the Biomedical Sciences X*, volume 7569, pp. 176–182 (SPIE, 2010).

[163] A.-M. Pena, A. Fabre, D. Débarre, J. Marchal-Somme, B. Crestani, J.-L. Martin, E. Beaurepaire, and M.-C. Schanne-Klein. *Three-dimensional investigation and scoring of extracellular matrix remodeling during lung fibrosis using multiphoton microscopy*. Microscopy research and technique **70**(2), 162–170 (2007).

[164] L. F. Ochoa, A. Kholodnykh, P. Villarreal, B. Tian, R. Pal, A. N. Freiberg, A. R. Brasier, M. Motamedi, and G. Vargas. *Imaging of murine whole lung fibrosis by large scale 3d microscopy aided by tissue optical clearing*. Scientific reports **8**(1), 13348 (2018).

[165] J. O. Escobedo, O. Rusin, S. Lim, and R. M. Strongin. *Nir dyes for bioimaging applications*. Current opinion in chemical biology **14**(1), 64–70 (2010).

[166] M. Rumi, S. Barlow, J. Wang, J. W. Perry, and S. R. Marder. *Two-photon absorbing materials and two-photon-induced chemistry*. Photoresponsive Polymers I pp. 1–95 (2008).

[167] G. Wensheng, F. Guo, C. Wei, Q. Liu, G. Zhou, D. Wang, and Z. Shao. *Shg from centrosymmetric supermolecular crystal*. Science in China Series B: Chemistry **45**, 267–274 (2002).

[168] L. A. Remington and D. Goodwin. *Clinical Anatomy and Physiology of the Visual System E-book: Clinical Anatomy and Physiology of the Visual System E-book* (Elsevier Health Sciences, 2021).

[169] I. Sanchez, R. Martin, F. Ussa, and I. Fernandez-Bueno. *The parameters of the porcine eyeball*. Graefe's Archive for Clinical and Experimental Ophthalmology **249**, 475–482 (2011).

[170] A. C. Croce and G. Bottiroli. *Autofluorescence spectroscopy and imaging: a tool for biomedical research and diagnosis*. European journal of histochemistry: EJH **58**(4) (2014).

[171] C.-M. Chuong, B. Nickoloff, P. Elias, L. Goldsmith, E. Macher, P. Maderson, J. Sundberg, H. Tagami, P. Plonka, K. Thestrup-

Pederson, *et al. What is the'true'function of skin?* Experimental dermatology **11**(2), 159–187 (2002).

[172] N. Dragicevic, H. I. Maibach, *et al. Percutaneous penetration enhancers physical methods in penetration enhancement*. Technical report, Springer (2017).

La borsa di dottorato è stata cofinanziata con risorse del Programma Operativo Nazionale Ricerca e Innovazione 2014-2020, risorse FSE REACT-EU Azione IV.4 “Dottorati e contratti di ricerca su tematiche dell’innovazione” e Azione IV.5 “Dottorati su tematiche Green”